

**NOVEL SINGLE-MOLECULE FORCE SPECTROSCOPY  
APPROACHES TO CHARACTERIZE INTERACTIONS OF  
MEMBRANE PROTEINS**

**Inauguraldissertation**

zur

Erlangung der Würde eines Doktors der Philosophie

vorgelegt der

Philosophisch-Naturwissenschaftlichen Fakultät

der Universität Basel

von

Michael Zocher

aus

Ilmenau, Deutschland

Basel, 2012

Genehmigt von der Philosophisch-Naturwissenschaftlichen Fakultät  
auf Antrag von  
Prof. Dr. Andreas Engel und Prof. Dr. Sebastian Hiller

Basel, den 26.06.2012

Prof. Dr. Martin Spiess  
Dekan

## **Abstract**

Atomic force microscopy (AFM) based single-molecule force spectroscopy (SMFS) is a biophysical tool used to investigate folding and unfolding of biological macromolecules, like membrane proteins. Unfolding of single membrane proteins can be recorded by force-distance (FD) curves, which exhibit reproducible sawtooth-like patterns of force peaks. These force peaks reflect the unfolding of stable structural segments. In the case of  $\alpha$ -helical transmembrane proteins, these segments consist of partial or complete  $\alpha$ -helices, or even of several consecutive  $\alpha$ -helices connected by extracellular or intracellular loops. Fitting these force peaks using polymer extension models reveals the exact position of the interaction within the membrane protein. Furthermore, with SMFS based dynamic force spectroscopy (DFS) it is possible to study intrinsic behavior of proteins, such as energetic, kinetic and mechanical properties, or, in other words, their energy landscape. The work presented here contains two SMFS-related projects that were carried out independently from each other. However, both projects are novel SMFS approaches that improve our understanding of  $\alpha$ -helical transmembrane proteins.

In the first project, it was investigated how cholesterol, an essential component of eukaryotic membranes, and ligands modulate the energy landscape of the human  $\beta_2$  adrenergic G protein-coupled receptor ( $\beta_2$ AR). G protein-coupled receptors (GPCRs) are a class of versatile proteins that transduce signals across membranes. Environmental changes induce inter- and intramolecular interactions that change the functional state of GPCRs and activate intracellular messenger molecules. How these interactions are established and how they modulate the functional state of  $\beta_2$ AR was addressed in this project. Cholesterol considerably increased the kinetic, energetic, and mechanical stability of almost every structural segment at sufficient magnitude to alter the structure and function relationship of  $\beta_2$ AR. One exception was the

structural core segment of  $\beta_2$ AR, which establishes multiple ligand-binding sites and which properties were not significantly influenced by cholesterol. This suggests that cholesterol may not necessarily influence ligand binding to  $\beta_2$ AR rather than setting the GPCR into a different state so that the receptor will respond differently to ligand binding. For that purpose, SMFS and DFS approaches were used to investigate how ligand binding modulates the energy landscape of  $\beta_2$ AR. Five different ligands that represented agonists, inverse agonists or neutral antagonists established a complex network of interactions that tuned the kinetic, energetic and mechanical properties of functionally important structural regions of  $\beta_2$ AR. These interactions were specific to the efficacy profile of the investigated ligands, which suggests that the functional modulation of GPCRs follows structurally well-defined interaction patterns.

The second project addressed the problem that SMFS is a rather time-consuming technique, since the membranes embedding the membrane proteins must be imaged and localized before starting the actual SFMS measurement. In order to simplify the investigation of membrane proteins by SMFS the light-driven proton pump bacteriorhodopsin (BR) was reconstituted into lipid nanodiscs. The advantage of using nanodiscs is that membrane proteins can be handled and characterized like water-soluble proteins with similar ease. SMFS characterization of BR in native purple membranes and in nanodiscs revealed no significant alterations of structure, function, unfolding intermediates, and strengths of inter- and intra-molecular interactions. This demonstrates that lipid nanodiscs provide a unique approach for *in vitro* studies of native membrane proteins using SMFS and opens up a new avenue to characterize membrane proteins by a wide variety of SMFS approaches that have been established on water-soluble proteins.

## Zusammenfassung

Rasterkraftmikroskopie (AFM) basierte Einzelmolekül-Kraftspektroskopie (SMFS) ist eine biophysikalische Anwendung, die es ermöglicht, Entfaltung und Faltung von biologischen Makromolekülen, zum Beispiel von Membranproteinen, zu studieren. Die Entfaltung von einzelnen Makromolekülen kann mittels einer Kraft-Abstands-Kurve gemessen werden. Eine typische Kraft-Abstands-Kurve, welche die Entfaltung eines Transmembranproteins widerspiegelt, weist eine sägezahnartige Struktur aus Peaks auf. Jeder dieser Peaks entspricht der Entfaltung eines stabilen strukturellen Segments des entfalteten Proteins. Bei  $\alpha$ -helikalen Transmembranproteinen bestehen diese Segmente aus  $\alpha$ -Helices (oder Teilen davon), oder sogar aus mehreren Transmembransegmenten, welche durch extra- oder intrazelluläre Loops miteinander verbunden sind. Die Peaks können mittels physikalischer Modelle, die das Verhalten steifer Polymere bei Dehnung beschreiben, gefittet werden. Dadurch kann die exakte Position, an welcher innerhalb des Membranproteins eine Interaktion auftritt, bestimmt werden. Des Weiteren ist es möglich, mit dynamischer Kraftspektroskopie (DFS), ein auf SMFS basierendes Verfahren, das intrinsische Verhalten von Proteinen zu untersuchen. Beispielsweise können mittels DFS biophysikalische Parameter, wie energetische, kinetische und mechanische Eigenschaften (Energielandschaft) von Proteinen bestimmt werden. Bei der im Folgenden vorgestellten Arbeit handelt es sich um zwei voneinander unabhängig durchgeführte SMFS-Projekte. Beide Projekte sind neuartige Ansätze, welche unser Verständnis von  $\alpha$ -helikalen Transmembranproteinen verbessern.

Im ersten Projekt wurde der Einfluss von Cholesterin, einem essentiellen Bestandteil eukaryotischer Membranen, auf die Energielandschaft des humanen  $\beta_2$  adrenergen G-Protein-gekoppelten Rezeptors ( $\beta_2$ AR) untersucht. G-Protein-gekoppelte Rezeptoren (GPCRs) sind die größte und vielseitigste Gruppe von Membranrezeptoren.

Extrazelluläre Veränderungen induzieren inter- und intramolekulare Interaktionen, die den funktionellen Zustand von GPCRs modulieren und dadurch eine intrazelluläre Signalkaskade auslösen. In dem Projekt wurde untersucht, auf welche Art und Weise diese Interaktionen etabliert werden und wie sie den funktionellen Zustand des  $\beta_2$ ARs beeinflussen. Cholesterin hatte einen wesentlichen Einfluss auf die Stärke der Interaktionen sowie die Energielandschaft fast aller struktureller Segmente des Rezeptors. Eine Ausnahme war das strukturelle Kernsegment von  $\beta_2$ AR, welches eine Vielzahl von Ligandenbindungsstellen aufweist. Die Eigenschaften dieses Segmentes blieben auch in Gegenwart von Cholesterin unverändert. Da Cholesterin nicht notwendigerweise die Bindung von Liganden beeinflusst, ist zu vermuten, dass das Kernsegment seine Eigenschaften ändert, nachdem ein Ligand gebunden hat. Um diese Frage zu beantworten wurde mittels SMFS und DFS untersucht, wie die Bindung von Liganden an  $\beta_2$ AR dessen Energielandschaft beeinflusst. Fünf Liganden unterschiedlicher therapeutischer Wirksamkeit etablierten ein Netzwerk von Interaktionen, welches die kinetischen, energetischen und mechanischen Parameter funktionell wichtiger struktureller Regionen des Rezeptors modulierte. Diese Interaktionen waren spezifisch entsprechend der Wirksamkeit des jeweiligen Liganden. Offenbar folgt die funktionelle Modulation von GPCRs strukturell definierten Interaktionsmustern.

Bei SMFS von Membranprotein handelt es sich um relativ zeitintensive Messungen, da die Membranen, in die das zu untersuchende Protein eingebettet ist, zunächst abgebildet und lokalisiert werden müssen. Dieses Problem wurde im zweiten Projekt näher betrachtet. Um SMFS mit Membranproteinen zu vereinfachen, wurde die lichtgetriebene Protonenpumpe Bakteriorhodopsin in Nanodiscs rekonstituiert. Nanodiscs sind synthetische Modellmembranen, mittels derer Membranproteine ähnlich wie wasserlösliche Proteine behandelt werden können. Die Charakterisierung von nativem BR in der Purpurmembran sowie in Nanodiscs ergab keine signifikanten Unterschiede bezüglich Struktur, Funktion, Entfaltungsintermediaten sowie Stärke von inter-

iv

und intramolekularen Interaktionen. Diese Resultate bestätigen, dass Nanodiscs neue Möglichkeiten für SMFS-Studien an Membranproteinen *in vitro* bieten.



---

## Table of contents

<b>1</b>	<b>Cell membranes and membrane proteins .....</b>	<b>1</b>
1.1	Cells and their membranes .....	1
1.2	Membrane proteins.....	3
1.2.1	Folding of membrane proteins .....	5
1.2.1.1	Sec-dependent insertion.....	5
1.2.1.2	Insertion models .....	6
1.2.2	Membrane protein research – a challenge .....	7
1.2.3	Approaches to study membrane proteins .....	8
<b>2</b>	<b>The atomic force microscope .....</b>	<b>11</b>
2.1	History .....	11
2.2	Atomic force microscopy in biophysics .....	12
2.3	Instrumental setup .....	13
2.4	Cantilevers.....	14
2.5	Calibration.....	15
2.5.1	Calibration of the photo-detection system.....	15
2.5.2	Calibration of the cantilever spring constant.....	17
2.6	Sample and support preparation .....	18
2.7	Contact mode imaging .....	19
2.8	AFM-based force measurements.....	19
2.8.1	Single-molecule force spectroscopy (SMFS).....	19
2.8.2	Polymer extension models .....	20
2.8.3	Dynamic force spectroscopy (DFS).....	21
<b>3</b>	<b>Molecular interactions of the human G protein-coupled <math>\beta_2</math> adrenergic receptor .....</b>	<b>25</b>
3.1	Introduction .....	27
3.1.1	Multifaceted functionality of GPCRs .....	27
3.1.2	Cholesterol and GPCRs .....	29
3.1.3	Ligands and their efficacy profiles .....	31
3.2	Experimental procedures.....	32
3.2.1	Preparation of $\beta_2$ AR proteoliposomes .....	32
3.2.2	SMFS and DFS .....	33
3.2.3	Data selection.....	35

3.2.4	Data analysis.....	35
3.2.5	Assignment of stable structural segments .....	35
3.2.6	Calculation of $x_u$ and $k_0$ .....	36
3.2.7	Calculation of transition barrier height and rigidity.....	36
<b>3.3</b>	<b>Cholesterol dependent interactions of <math>\beta_2</math>AR .....</b>	<b>37</b>
3.3.1	Results .....	37
3.3.1.1	SFMS of human $\beta_2$ AR in the presence and absence of cholesterol .....	37
3.3.1.2	Unfolding $\beta_2$ AR from N- and C-terminal ends .....	40
3.3.1.3	Mapping interactions that stabilize structural segments of $\beta_2$ AR.....	43
3.3.1.4	Cholesterol changes the energy landscape of $\beta_2$ AR .....	45
3.3.1.5	Cholesterol increases kinetic and energetic stability of $\beta_2$ AR.....	49
3.3.1.6	Cholesterol increases conformational variability and decreases mechanical rigidity of transmembrane $\alpha$ -helices H1 and H2.....	50
3.3.2	Discussion.....	51
3.3.2.1	Cholesterol strengthens interactions of almost every structural segment of $\beta_2$ AR.....	51
3.3.2.2	Cholesterol increases free energy barrier and kinetic stability of every structural segment except for the structural core segment.....	52
3.3.2.3	[H1.1].....	53
3.3.2.4	[H1.2-C1] .....	54
3.3.2.5	[H2.1].....	55
3.3.2.6	[H2.2-E1] .....	55
3.3.2.7	[H3-C2-H4-E2-H5.1].....	55
3.3.2.8	[H5.2-C3-H6.1].....	56
3.3.2.9	[H6.2-E3-H7-H8].....	57
3.3.2.10	[CT].....	57
<b>3.4</b>	<b>Ligand-specific changes of the <math>\beta_2</math>AR .....</b>	<b>58</b>
3.4.1	Results .....	58
3.4.1.1	Determining energetic, kinetic and mechanical properties of structural segments of $\beta_2$ AR in the presence of ligands .....	58
3.4.1.2	Ligands change energy landscape of $\beta_2$ AR.....	58
3.4.1.3	Structural segments changing conformational variability upon ligand binding.....	64
3.4.1.4	Structural segments changing lifetime upon ligand binding.....	64
3.4.1.5	Structural segments changing free energy upon ligand binding.....	65
3.4.1.6	Structural segments changing mechanical properties upon ligand binding.....	65
3.4.2	Discussion.....	66

---

3.4.2.1	Ligand binding to $\beta_2$ AR lacks pronounced localized interactions.....	66
3.4.2.2	Conformational variability and kinetic stability of unliganded $\beta_2$ AR..	66
3.4.2.3	Energetic stability and mechanical elasticity of unliganded $\beta_2$ AR.....	67
3.4.2.4	High conformational variability and mechanical elasticity of structural core correlates to basal $\beta_2$ AR activity .....	68
3.4.2.5	Properties of $\beta_2$ AR modified by the neutral antagonist alprenolol.....	69
3.4.2.6	An overall scheme: most ligands modulate the structural core segment of $\beta_2$ AR.....	70
3.4.2.7	The inverse agonist carazolol introduces major modifications to $\beta_2$ AR	73
3.4.2.8	Carazolol modifies structural regions proposed to be involved in oligomerization .....	74
3.4.2.9	Carazolol employs direct and indirect interactions to modify structural regions .....	75
<b>3.5</b>	<b>Conclusions.....</b>	<b>75</b>
<b>4</b>	<b>Single-molecule force spectroscopy from lipid nanodiscs .....</b>	<b>79</b>
<b>4.1</b>	<b>Introduction .....</b>	<b>81</b>
<b>4.2</b>	<b>Experimental procedures.....</b>	<b>83</b>
4.2.1	Expression and purification of MSP1 .....	83
4.2.2	Preparation of BR .....	84
4.2.3	Reconstitution of BR into nanodiscs .....	85
4.2.4	UV/vis spectra .....	86
4.2.5	Circular dichroism .....	86
4.2.6	SMFS .....	86
4.2.7	Selection and analysis of F-D curves .....	87
4.2.8	Assignment of stable structural segments .....	87
<b>4.3</b>	<b>Results and discussion.....</b>	<b>88</b>
4.3.1	Mechanically unfolding single BR molecules from purple membrane and from nanodiscs .....	88
4.3.2	BR in purple membrane and in nanodiscs choose identical unfolding intermediates .....	92
4.3.3	BR <sub>PM</sub> and BR <sub>ND</sub> populate unfolding intermediates similarly .....	98
4.3.4	Limited binding probability of the C-terminal end.....	99
<b>4.4</b>	<b>Summary .....</b>	<b>100</b>
<b>5</b>	<b>Outlook .....</b>	<b>103</b>
<b>6</b>	<b>Appendix .....</b>	<b>105</b>
<b>6.1</b>	<b>Abbreviations.....</b>	<b>105</b>

*Table of contents*

---

<b>6.2 Symbols.....</b>	<b>106</b>
<b>6.3 Acknowledgements.....</b>	<b>107</b>
<b>7 Bibliography .....</b>	<b>109</b>
<b>Curriculum Vitae.....</b>	<b>I</b>

# **1 Cell membranes and membrane proteins**

## **1.1 Cells and their membranes**

It is estimated that there are about 100 million living species on earth today (1). Most of them are single cells. Others, for example humans, are enormous multicellular complexes in which specialized groups of cells perform specific functions and are linked by intricate communication systems (1). Nevertheless, all cells on earth share common features: hereditary information stored by DNA, DNA replication systems, transcription of DNA into RNA, and translation of RNA into proteins (1). Thus, every cell on the planet can be regarded as a biochemical factory dealing with the same basic molecular building blocks: DNA, RNA and proteins. Nevertheless, at least one other universal component of cells is missing: each cell is confined by a container – the plasma membrane. It acts as a selective barrier, enabling the cell to concentrate nutrients gathered from the environment, retaining the products it synthesizes for its own use and excreting its waste products (1). Without the plasma membrane, cells would lose their integrity as coordinated chemical systems (1). Complex multicellular organisms, such as eukaryotes, have specialized membranes that define different organelles, for example endoplasmic reticulum, Golgi apparatus, mitochondria, chloroplasts and other membrane-enclosed organelles, which maintain the characteristic differences between the contents of each organelle and the cytosol (2).

The membrane consists of a set of amphipathic molecules called lipids, which have a hydrophobic (water-insoluble) and a hydrophilic (water-soluble) part. Membrane lipids constitute about 50% of the mass of most animal cell membranes. Lipid molecules aggregate spontaneously when placed in water. They arrange their hydrophobic portions to be as much in contact with one another as possible to shield them from water molecules whereas their hydrophilic portions are kept exposed (1).

Phospholipid molecules comprise most of the plasma membrane (1). Phospholipids have a polar headgroup and two hydrophobic hydrocarbon tails, usually fatty acids of different lengths (1). They spontaneously aggregate in aqueous environment forming a bilayer that creates small closed vesicles. This lipid bilayer has been decisively established as the universal basis for cell-membrane structure (1).

The plasma membrane of many mammalian cells contains phosphatidylcholine (PC), phosphatidylethanolamine (PE), phosphatidylserine (PS) and sphingomyelin (SM). The composition of lipids depends on cell type, organelle, and organism (1, 3). Additionally, the lipid bilayer of many cell membranes often contains cholesterol<sup>1</sup> and glycolipids (1, 3). The different types of lipids are not equally distributed within the two monolayers (leaflets) of the membrane (4). PS and PE are enriched in the cytoplasmic leaflet of the membrane, whereas PC and SM are primarily located in the outer monolayer (1, 5). PS is negatively charged, which results in a significant difference in charge between the two halves of the bilayer. This effect is referred to as the “positive-inside” rule (6-9).

The resulting asymmetry is functionally important. Many proteins specifically bind or recognize certain lipid headgroups (10, 11). Animals use the phospholipid asymmetry of their plasma membranes to discriminate between living and dead cells (1). Furthermore, the distribution of lipids influences protein folding, assembly (12) and activity (13, 14).

The “fluid mosaic model”, which has been proposed by Singer and Nicolson in 1972, describes membranes as an oriented, dynamic, two dimensional, and viscous solution of proteins and lipids (15). However, it turned out that membranes are more mosaic than fluid (16). Membrane proteins undergo restrained or directed motion within membranes (17).

---

<sup>1</sup> Cholesterol reduces the permeability of membranes to small water-soluble molecules (1). It can be predominantly found in eukaryotic plasma membranes, since they contain large amounts of cholesterol.

They are often organized in large functionally relevant supramolecular complexes, such as the respiratory chain complexes I, III and IV (18) and photosystems I and II (19). In addition, membranes contain microdomains, or lipid rafts, which are enriched in sphingolipids, cholesterol and membrane proteins (1).

## **1.2 Membrane proteins**

For cells to function properly, membranes must not be completely impermeable. A cell must be able to import raw materials and export waste across its membranes. To transfer specific molecules from one side to the other, cells have specialized proteins embedded in their membrane. These transport proteins mainly determine which molecules can enter or exit the cell. Furthermore, all cells have membrane proteins that act as sensors of external stimuli, allowing the cell to change its behavior in response to environmental signals. Instead of molecules, these protein sensors, or receptors, transfer information across the membrane (1).

Why are membrane proteins such an interesting and important field of research? In fact, 20-30% of all open reading frames in the genome of eubacterial, archaean, and eukaryotic organisms encode integral membrane proteins (20), indicating the importance of this class of proteins. Since membrane proteins are located at the boundaries of cells and other membrane-enclosed organelles, they are involved in all processes that require signal transduction across the membrane. They transport solubles, like toxic compounds and nutrients. Moreover, they play important roles in energy conversion and cell adhesion (1). Since they are involved in so many processes, they are important targets for drugs. Actually, about 70% of all drug targets are membrane proteins (21, 22). Mutations in membrane proteins can be the cause of a multitude of diseases, for example cystic fibrosis and retinitis pigmentosa (23, 24). To develop new drugs and understand the molecular processes behind these diseases, it is of major importance to gain insight into structural and functional mechanisms of membrane proteins. However, compared to soluble proteins, the amount of membrane protein structures in the

Protein Data Bank (PDB)<sup>2</sup> (25) is underrepresented. Because of the slow progress of membrane protein structure determination (26), structures and functional mechanisms of membrane proteins are poorly understood.

Two protein secondary structure motifs capable of passing the membrane have been observed:  $\alpha$ -helical bundles and antiparallel  $\beta$ -strands (**Figure 1.1**). The great majority of membrane-spanning segments traverse the bilayer forming a  $\alpha$ -helical bundle.  $\alpha$ -helical membrane proteins contribute to active transport of solubles, signaling, and communication with other cells. In contrast,  $\beta$ -barrel membrane proteins arrange their transmembrane strands as a  $\beta$ -sheet in the form of a barrel. These proteins can be found in the outer membrane of Gram-positive bacteria. In eukaryotes,  $\beta$ -barrel proteins are abundant in the outer membrane of mitochondria and chloroplasts<sup>3</sup>. However, the majority of multipass transmembrane proteins in the bacterial plasma membrane and in eukaryotic cells are composed of transmembrane  $\alpha$ -helices (1).

---

<sup>2</sup> On June 4, 2012, the search for membrane and cell surface proteins and peptides in the PDB resulted in 615 hits. The PDB contained 75885 protein structures at that day.

<sup>3</sup> Structure, assembly and folding of  $\beta$ -barrel membrane proteins are reviewed in (27-31).

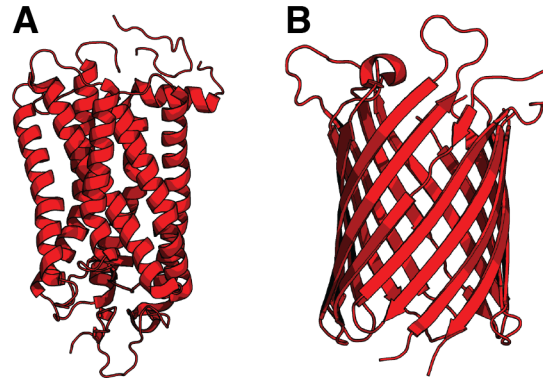


**Figure 1.1: The two major structural motifs found in membrane proteins.** (A) The heterotrimeric guanine nucleotide-binding protein (G protein)-coupled receptor rhodopsin from bovine rod outer segment (ROS). The transmembrane region contains seven  $\alpha$ -helical bundles, which are connected by extramembrane loops. PDB ID: 1F88 (32). (B) The OmpG protein from *Escherichia coli* is a  $\beta$ -barrel protein composed of 14 antiparallel  $\beta$ -strands. PDB ID: 2FIC (33). Both proteins are shown in side-view.

## 1.2.1 Folding of membrane proteins

### 1.2.1.1 Sec-dependent insertion

One important step during the lifetime of a membrane protein is its insertion into the lipid bilayer, a process that follows protein synthesis. Exhaustive functional studies on bacterial and eukaryotic homologues of the archaeobacterial protein-translocating SecYEG channel have significantly advanced our understanding of the molecular mechanisms that guide folding and insertion of membrane proteins (34-38).

The process of membrane protein folding and insertion is facilitated and controlled by the so-called translocon protein machinery (36, 37). It consists of a hydrophilic cavity with a diameter of a few tens of Ångströms, and a ribosome-binding site, which is displayed towards the cytoplasm. The N-terminal portion of a nascent polypeptide chain of a membrane protein contains a signal sequence in the N-terminal part that targets the ribosome-peptide complex to the translocon. After binding of the ribosome to the translocon, the nascent polypeptide chain is directly expelled from the ribosomal exit tunnel into the pore of the translocon. The translocon can accommodate peptides with a length of  $\approx 20$  aa, which

is sufficient to form an  $\alpha$ -helical transmembrane segment. The peptide exits the translocon through a lateral gate. The gate might open and close periodically (39) in order to allow the segment to sense and partition into the lipid bilayer (40). As indicated by the size of the pore, transmembrane segments laterally exit the translocon one by one or pairwise (41, 42). While hydrophobic sequences are inserted into the membrane, hydrophilic sequences pass through the aqueous pore or emerge between the translocon and the ribosome.

### **1.2.1.2 Insertion models**

Popot and Engelman introduced models, which describe the folding and insertion of membrane proteins into a membrane (43, 44). In the two-stage model, the membrane protein inserts into the lipid bilayer in a process driven by a translocon. Secondary structure elements like the  $\alpha$ -helical bundle are formed in this step. In contrast to soluble proteins, whose three-dimensional fold is dictated by their amino acid sequences (45), the folding of a membrane protein requires the interplay between ribosome and the translocon machinery. In the second step, the actual membrane protein folding process takes place, including the formation of the correct tertiary or quaternary structure. Furthermore, the transmembrane elements need to rearrange and reorient to adopt the correct fold. The formation of additional structural elements (*e.g.* re-entrant loops), binding of cofactors or oligomerization can be combined in a third step.

The dimerization of  $\alpha$ -helical bundles is promoted by specific amino acid sequence motifs within the peptide (*e.g.* GxxxG) (46-48). This process optimizes the packing of helices through van-der-Waals interactions (46). In addition, the formation of interhelical hydrogen bonds can be observed even in early stages of the translocon-mediated protein insertion (49).

Although the two-stage folding model for membrane proteins appears simple, it provides an explanation of many experimental data. For instance, it has been shown that peptide fragments of membrane

proteins can be independently refolded or synthesized and assemble into functional proteins (50).

Despite its simplicity, the two-stage model does not provide answers to certain questions, for example how and when transmembrane  $\alpha$ -helices are formed. Also, it does not explain the principles behind this process. The four-step model provides a more detailed insight based on experimental data such as folding and insertion of synthetic peptides and small proteins into lipid bilayers (51). It includes the following steps: (i) partitioning of the unfolded polypeptide chain in the interface region of the membrane, (ii) folding of the  $\alpha$ -helical segment, (iii) insertion of the  $\alpha$ -helical segment, and finally (iv) association of  $\alpha$ -helical transmembrane segments (**Figure 1.2**). The membrane interface provides a local free energy minimum for binding and the subsequent folding of hydrophobic peptides (52-54). The minimization of the free energy is the driving factor behind this process.

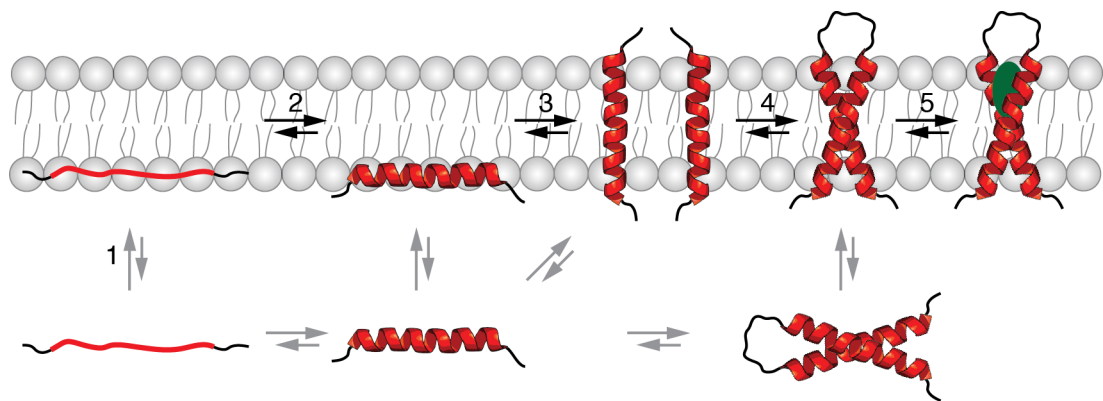


**Figure 1.2: The four-step model of membrane protein folding.** (1) Partitioning of the unfolded polypeptide chain. (2) Folding of  $\alpha$ -helical segments. (3) Insertion of  $\alpha$ -helical segments. (4) Association of  $\alpha$ -helical segments (5) Optional: assisted folding by a chaperone (green).

### 1.2.2 Membrane protein research – a challenge

As mentioned in section 1.1, there are still considerable difficulties in membrane protein research. The repertoire of reliable methods to produce, purify, solubilize and reconstitute or crystallize a membrane protein is limited, compared to the techniques available for water-soluble

proteins. To make things worse, the handling of a membrane protein is much trickier than working with a water-soluble protein.

The concentration of membrane proteins in the native membrane is usually very low<sup>4</sup>. Therefore, approaches to overexpress membrane proteins are required (56-58). Overexpressed proteins can accumulate in the membrane, which may induce stress response mechanisms or can have other cytotoxic effects (58). Moreover, it is difficult to express eukaryotic membrane proteins in bacteria, since they do not fulfill certain requirements, such as specific glycosylation (58, 59) or lipid composition of the membrane (13, 60). In addition, translation rates differ between prokaryotes and eukaryotes, which eventually leads to aggregation and misfolding of the membrane protein of interest (56). The complexity of the cellular membrane further complicates purification of functional membrane proteins.

Membrane proteins can be solubilized by detergents, which stabilize the protein in aqueous solutions (61, 62). Since the (long-term) stability of membrane proteins depends on the nature of the solubilizing agents (57, 62) the choice of detergent is possibly the most important decision to make when purifying a membrane protein. Alternatively, membrane proteins can be solubilized using polymers with a hydrophilic backbone and hydrophobic side chains, so-called amphipols (63).

### **1.2.3 Approaches to study membrane proteins**

As discussed in the previous section, structure determination of membrane protein research remains an intricate challenge. Due to the enormous number of crystallization conditions that have to be screened and the low stability of solubilized membrane proteins, the growth of well-diffracting three-dimensional (3D) crystals for X-ray crystallography is very time-consuming.

---

<sup>4</sup> Some proteins are available in large quantities from their native membrane, for example bacteriorhodopsin (55). Therefore they can be purified from their natural sources.

Novel approaches, like the lipid cubic phase (64), fusion with large hydrophilic domains (65), and the use of antibody fragments (66) to improve crystallization of membrane proteins did not significantly accelerate the pace of structure determination. Nevertheless, this problem can be overcome by the use of electron microscopy (EM) (67). EM requires the arrangement of proteins in a two-dimensional (2D) planar ordered structure (68). An increase in resolution to near-atomic level (69) can be achieved by freezing the sample, a technique called cryo-EM (70). Besides, single-particle EM techniques to approach large proteins yield in medium resolution (8-30 Å), allowing observation of functionally related conformational changes (71). Furthermore, nuclear magnetic resonance (NMR) approaches, such as solution NMR (72), solid-state NMR (73) and magic-angle spinning NMR (74) provide increasing possibilities to study structure and dynamics of membrane protein complexes.

Besides these relatively new techniques, “classical” methods are still indispensable in membrane protein research. Important approaches are circular dichroism (CD) spectroscopy (75, 76), time-resolved Fourier transform infrared (FTIR) spectroscopy (77, 78), several different types of fluorescence spectroscopy (75, 79), calorimetric studies (80, 81) and electrophysiological techniques (82-84).

In addition to the experimental methods to study membrane proteins, computational tools have emerged in the past years. They gain importance since they strengthen or validate experimental data for these different methods. Additionally, the transmembrane topology based on sequence analysis can be predicted. The potential of molecular dynamics (MD) simulations is illustrated through modeling of structure and function of G protein-coupled receptors (GPCRs) (85, 86) and unfolding of bacteriorhodopsin (BR) (87, 88).

There is one more method for studying membrane proteins that has not been mentioned so far: the atomic force microscope (AFM), a powerful tool to address single membrane proteins. The AFM will be described in the following chapter.



## **2 The atomic force microscope**

### **2.1 History**

Stockholm, Wednesday, December 10, 1986. The Nobel Prize in Physics has just been awarded to two scientists, Gerd Binnig and Heinrich Rohrer, for their outstanding invention: the scanning tunneling microscope (STM). The STM, which uses a sharp tip to probe a surface, revolutionized microscopy. The tip “may be a fine needle, which is moved across the surface of the structure to be investigated. [...] This is just the beginning of an extremely promising and fascinating development. The old dream from antiquity of a visible image of the atomic structure of matter is beginning to look like a realistic possibility, thanks to progress in modern microscopy”<sup>5</sup>.

The STM showed the atomic structure at the crystalline surface of silicon and demonstrated the possibility to manipulate single atoms (89). However, the STM is limited to conducting surfaces, because it relies on tunnel currents between tip and surface. In 1986, Binnig and Rohrer received the Nobel Prize in Physics for their discovery. In the same year, Binnig together with Quate and Gerber introduced the atomic force microscope (AFM) (90) to image both conducting and non-conducting surfaces. Although true atomic resolution is only possible under ultrahigh vacuum and with atomically flat surfaces (91), the AFM impresses by its high spatial resolution. Both STM and AFM are members of the scanning probe microscopy (SPM) family.

Today AFMs are commercially available. They have evolved through several generations since the early 1990s. Many different types of AFMs have been developed that can be used not only for measuring the topologies of surfaces, but also for measuring the properties of various materials at or close to surfaces. With a resolution down to either atomic

---

<sup>5</sup> Excerpt from the Award Ceremony Speech. Nobelprize.org 4 Jun 2012 [http://nobelprize.org/nobel\\_prizes/physics/laureates/1986/presentation-speech.html](http://nobelprize.org/nobel_prizes/physics/laureates/1986/presentation-speech.html)

or molecular level, this can be done in a broad temperature range in vacuum, gas, or in liquids.

## **2.2 Atomic force microscopy in biophysics**

Over the past decades, the AFM has emerged into a versatile tool to study structural and mechanical properties of biological samples such as proteins and biological membranes (92). One advantage is the fact that these studies can be carried out under close to native conditions. For instance, Andreas Engel and Daniel J. Müller developed tools for high-resolution imaging of membrane proteins (93). With these methods it became possible to acquire images with a lateral resolution of  $\approx 5$  Å and a vertical resolution of  $\approx 1$  Å. Using AFM imaging of reconstituted membrane proteins and native membranes biophysicists gained insight into high-resolution information about the topography (94-103), conformational changes (101, 103-108), oligomeric states (109-122), or dynamic process of membrane proteins (123, 124). Furthermore, AFM based single-molecule force spectroscopy (SMFS, see section 2.8.1) has emerged into a tool to investigate unfolding and folding of membrane proteins (92, 125). Prior to an SMFS experiment, membrane proteins reconstituted into lipid bilayers are adsorbed on a flat surface and attached to the AFM cantilever with one of their termini (see section 2.6). In the actual SMFS measurement, the cantilever is retracted and the protein is stretched. During this process, the membrane protein is unfolded in a sequential manner. With the help of SMFS, interactions that stabilize membrane proteins can be determined (92). Furthermore, these interactions are located within the membrane protein structures using polymer extension models (see section 2.8.2).

It has already been shown that SMFS can address the effect of environmental changes on the membrane protein, for example temperature (126), ligands (127-131), ions (132, 133), inhibitors (134), point mutations (135), oligomeric states (136), pH (137) or the functional state of the protein (127, 128). A change in environmental factors affects molecular interactions that stabilize membrane proteins. This results in

changes in the unfolding spectra (125). An extension of SMFS uses unfolding at different velocities. This method is called dynamic force spectroscopy (DFS) and reveals parameters that are specific for the energy landscape of single membrane proteins (see section 2.8.3).

In addition to mechanical unfolding of membrane proteins, it is also possible to study their refolding into lipid bilayers (138, 139). In these unfolding experiments, the membrane protein is partially unfolded, leaving one mechanical anchor in the membrane. In the next step, the cantilever approaches the surface again, which relaxes the unfolded polypeptide chain and allows reinsertion of the peptide or parts of it into the lipid bilayer. The folding kinetics of a single membrane protein can be evaluated by changing the time before the cantilever is retracted again to completely unfold the protein.

### **2.3 Instrumental setup**

At first sight, the AFM seems to be a complicated instrument. Nevertheless, it works on a very simple principle and it is probably one of the easiest microscopy techniques to learn and understand. The instrumental setup of an AFM is simple (**Figure 2.1**). It consists of only three key components: i) a cantilever with a sharp tip or stylus at its end, ii) a piezoelectric transducer or actuator, which moves the sample mounted on its top in three dimensions with sub-nanometer precision<sup>6</sup>, and iii) an optic detection system that consists of a laser diode and a position sensitive photodiode (PSPD) with four quadrants for accurate detection of vertical and lateral displacement of the laser beam. Finally, a computer is required to control the AFM.

---

<sup>6</sup> AFMs from Bruker (formerly Veeco, DI) change the position of the sample. Other AFM instruments (*e.g.* JPK) move the cantilever for x-y-scanning and vertical adjustment in z-direction.

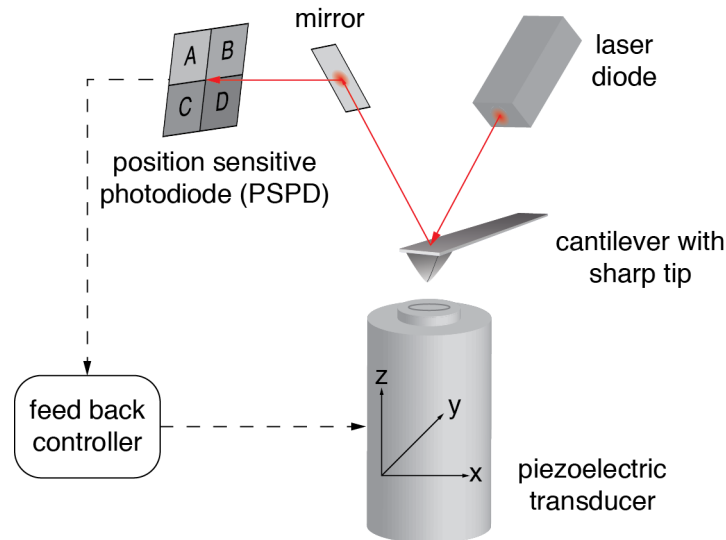


**Figure 2.1: Schematic illustration of a typical AFM setup.** A laser beam is focused on the backside of the cantilever. A mirror directs the reflected beam onto the photodiode (PSPD). Deflection of the cantilever changes the position of the laser spot on the PSPD, resulting in a signal, which is transferred to the controller. The controller processes the signal and sends a feedback signal to the piezoelectric transducer. Thus, the height of the surface is adjusted according to the feedback signal.

Before setting up an AFM experiment, the cantilever needs to be mounted on a fluid cell or glass block (not shown in **Figure 2.1**). Next, the laser beam is focused on the backside of the cantilever, from where it is reflected onto a mirror. The mirror directs the laser beam to the PSPD. Deflection of the cantilever changes the position of the laser spot on the PSPD. This change is transferred to the controller, which records the incoming information, processes it, and converts it into a feedback signal. Then the signal is sent to the piezoelectric actuator, which adjusts the height, or z-position of the sample, in order to change the deflection of the cantilever. Thus, the contact force between the AFM tip and the sample surface is changed as well.

## 2.4 Cantilevers

The cantilever with a sharp tip at its end is the most important part of an AFM, since it interacts with the sample. Modern AFM cantilevers and tips are commonly made from silicon, silicon-nitride ( $\text{Si}_3\text{N}_4$ ) or diamond. Usually cantilevers are rectangular or triangular shaped with a length of 50-200  $\mu\text{m}$  and a thickness of 0.5-2  $\mu\text{m}$ . They are

often coated with a thin layer of gold or aluminum for efficient reflection of the laser beam. Depending on the application, one can choose among cantilevers with different physical properties. Cantilevers used for high-resolution contact mode imaging have a spring constant of  $\approx 0.05\text{-}0.2$  N/m. Highly sensitive low-noise SMFS experiments require cantilevers with a spring constant of  $\approx 0.03$  N/m. However, spring constants of cantilevers used for non-contact mode applications are significantly higher by a factor of  $\approx 10$ .

It can be assumed that the cantilever acts like a Hookean spring<sup>7</sup> with the spring constant  $k$ . Therefore, the bending of the cantilever,  $dx$ , can be converted into force:

$$F = k \times dx \tag{Equation 2.1}$$

The force value usually lies in the range of piconewton (pN) to nanonewton (nN).

The spring constant of a cantilever is principally affected by its geometrical properties, such as length, width and thickness. Additionally, the material of a cantilever (Young's modulus) further affects the spring constant. **Equation 2.2** gives the theoretical spring constant of a rectangular cantilever.

$$k = \frac{Et^3w}{4l^3} \tag{Equation 2.2}$$

$E$  is the Young's modulus,  $t$  is the thickness,  $w$  is the width and  $l$  is the length of the cantilever (140). Typically, for biological AFM applications, rectangular or triangular cantilevers are used.

## 2.5 Calibration

### 2.5.1 Calibration of the photo-detection system

Calibrating the photo-detection system of the AFM followed by determination of the cantilever spring constant (see following section) is

---

<sup>7</sup> Assuming that cantilevers act like Hookean springs, this assumption is only valid for small deflections (several tens of nanometers). Cantilevers do not behave as linear springs at higher deflections anymore.

obligatory for precise force measurements. During all calibration procedures, the cantilever is immersed in liquid, and a solid supporting surface is required. The x,y-position of the cantilever relative to the sample is kept constant while the piezo-actuator is repeatedly extended and retracted in the vertical (z-) direction by a certain distance. The beam deflection in the contact area is recorded during these approach-and-retract cycles. This allows the correlation between the beam displacement on the PSPD in Volt (V) and the piezo-actuator in nm.

**Figure 2.2** on the next page illustrates how the deflection signal changes when the cantilever stylus gets into contact with the surface during an approach-and-retract cycle:

1. The cantilever is away from the surface. Fluctuations in the deflection signal are caused by thermal noise.
2. Next, the piezo-actuator is extended until the cantilever tip gets into contact with the surface.
3. The cantilever bends upwards until the end of the piezo extension, leading to a linear increase in the signal on the PSPD.
4. The piezo is retracted. The decrease in the bending of the cantilever is displayed by the linear decrease in the deflection signal. The deflection sensitivity (rate of signal strength correlated to extension in V/nm) can now be determined by fitting a line to this contact regime.
5. Usually, the cantilever sticks to the surface and bends downwards during piezo retraction, which results in a negative deflection signal, also called adhesion peak.
6. Further retraction of the piezo releases the cantilever from its interaction with the surface. Thus, it loses contact and relaxes into its original non-bent position.

Thus, after calibration of the photo-detection system, a measured voltage signal of the PSPD can be easily converted into a metric cantilever deflection.

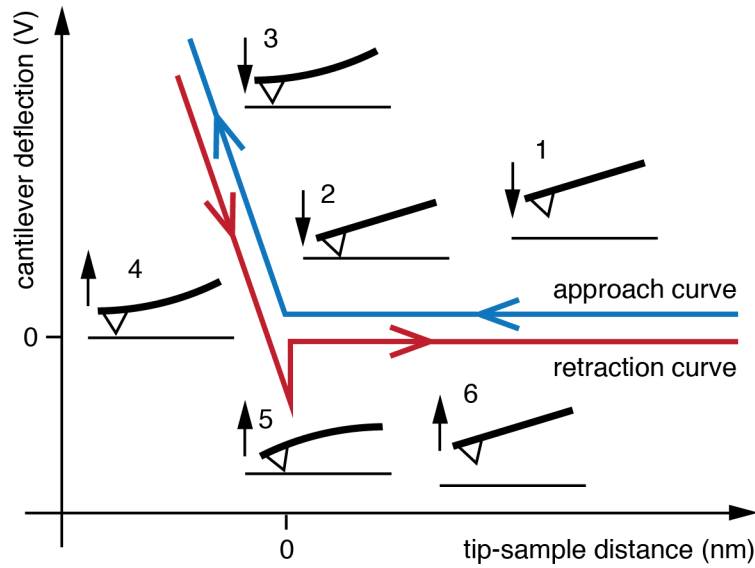


**Figure 2.2: Deflection of the cantilever during an approach-and-retract cycle.** For calibrating the deflection sensitivity of the PSPD detection system, the piezo-scanner is extended until the cantilever reaches the surface and deflects (1-3). Then, the scanner is retracted at constant speed and the cantilever relaxes (4-6). Thus, the piezo-extension can be directly correlated to the linear increase in the deflection of the cantilever (3 and 4).

### 2.5.2 Calibration of the cantilever spring constant

There are several possibilities to calculate the spring constant of an AFM cantilever (141). The most common method used for the calibration of AFM cantilevers is the so-called “thermal tuning” that was introduced by Hutter and Bechhoefer (142). The cantilever needs to be kept in solution, at a fixed position at least  $50\ \mu\text{m}$  away from the surface. Brownian motions induce minor free oscillations of the cantilever. After Fourier transformation of the free oscillation frequencies of the cantilever recorded over several seconds, a probability-oscillation frequency plot is generated. The resulting curve can be fitted with a power law, which allows determination of the actual spring constant of the respective cantilever. Measured spring constants can easily deviate by 50% compared to nominal spring constants provided by the manufacturer. This underlines the necessity of the calibration procedure.

## **2.6 Sample and support preparation**

In order to investigate a sample by AFM, it has to be adsorbed on a surface. This process is usually facilitated by physisorption (143) and strongly depends on the surface charges of both the supporting surface and the sample. The concentration of the sample as well as the adsorption time determine the adsorption efficiency, which can be optimized by minimizing repulsive electrostatic forces between sample and surface (143). Thus, the successful adsorption of a sample requires the careful adjustment of the electrolyte concentration and pH conditions. Furthermore, an appropriate surface is required on which the sample can be adsorbed. Adding cations balances the negative surface charge and leads to increased van-der-Waals interactions between sample and surface.

A commonly used surface for AFM studies on membrane proteins is negatively charged muscovite (mica). Mica was used as a supporting surface throughout the work presented in chapter 3 and chapter 4. Further supporting surfaces used for AFM experiments are highly ordered pyrolytic graphite (HOPG) (106), ultraflat gold (144, 145) or glass (146, 147). However, due to their hydrophobicity those materials might lead to destruction of the investigated membrane protein. For that reason, mica surfaces are the first choice for AFM studies on membrane proteins.

Usually a small piece of mica is glued onto a metal disc or onto a glass slide to ensure lateral fixation of the sample on the piezo-scanner (93). To adsorb a sample, it needs to be diluted in an appropriate buffer and subsequently placed on a clean surface. After an adequate adsorption time the surface needs to be washed several times. The AFM cantilever needs to be mounted on top of the sample. Normally, thermal equilibration requires several minutes before the experiment can be started.

## **2.7 Contact mode imaging**

In order to determine the topography of a surface, the AFM tip needs to be scanned over the area of interest in a raster-like manner. The bending of the cantilever provides information on the vertical dimension of the surface. In contact-mode imaging, the bending of the cantilever and, thus, the interaction force between tip and surface are kept constant by adjusting a user-defined value (set point). For that purpose, the height of the sample is constantly adjusted by the piezo movement. This imaging mode is also referred to as constant force mode. Usually, the scanning force is kept low ( $\approx 100$  pN) in order to minimize alterations or distortion of topographical features of the sample. Contact mode imaging facilitated high-resolution images of several membrane proteins, like bacteriorhodopsin (BR) (148), connexin channels (103), the c-rings of ATP synthase (119) and the  $\beta$ -barrel protein OmpG (107).

## **2.8 AFM-based force measurements**

Introduced to image the topography of inorganic surfaces in vacuum at nanometer precision (90), the AFM has emerged into a multifunctional toolbox in nanobiotechnology (149). One of a multitude of the currently used AFM techniques is an approach called single-molecule force spectroscopy (SMFS), which will be described in the next section.

### **2.8.1 Single-molecule force spectroscopy (SMFS)**

Single-molecule force spectroscopy (SMFS) is an AFM technique, which uses force to unfold single proteins. SMFS has been introduced by Gaub (150) and Lee (151) to probe the strength of receptor-ligand bonds. All SMFS experiments that have been conducted so far demonstrated that the forces probed by SMFS reflect interactions within or between molecules. Unraveling the mechanisms of protein folding and unfolding, receptor-ligand interactions, and ligand-binding interactions that switch the functional state of a protein are only a small number of biologically and medically pertinent questions that can be answered by SMFS (149).

The first protein investigated by SMFS (and probably the best-studied one) is the immunoglobulin titin (152). In the muscle sarcomeres of humans, the titin filament acts as an adjustable molecular spring. About 90% of the titin filaments are immunoglobulin (IG) domains that provide mechanical elasticity to the filament (153). Reversible unfolding of an oligomeric titin construct was achieved by simply applying a mechanical pulling force to both ends of the peptide. Recording the applied force over the distance the peptide has been stretched revealed a characteristic sawtooth-like pattern of force peaks. Every single force peak of this pattern reflected unfolding of a single IG domain of the peptide, whereas the sequence of force peaks described the unfolding pathways of all IG domains within the oligomeric titin construct.

The light-driven proton pump bacteriorhodopsin (BR) from *Halobacterium salinarum*<sup>s</sup> was the first membrane protein studied by SMFS (156). BR is an ideal model for SMFS on membrane proteins, since its atomic structure is known (64, 157). Furthermore, it is easy to purify and naturally abundant. Thus, an enormous amount of function-related biochemical data on BR is available (158). In SMFS experiments, single BR molecules withstand forces of up to 200 pN before their structural segments unfold cooperatively (159) (see chapter 4). Mechanical unfolding of BR occurs along a few highly reproducible pathways, which are temperature-dependent (126, 159).

### **2.8.2 Polymer extension models**

In order to describe the stretching of flexible polymer chains the freely jointed chain model was developed (160). From this model, the worm-like chain (WLC) model emerged (161). The WLC model describes the extension of semi-flexible polymer chains (161, 162). The force  $F$  required to stretch the polymer chain is given by

---

<sup>s</sup> *Halobacterium salinarum* is a halophilic marine Gram-negative obligate aerobic archaeon (154, 155).

$$F(x) = \frac{k_B T}{l_p} \left[ 0.25 \left( 1 - \frac{x}{L_c} \right)^{-2} - 0.25 + \frac{x}{L_c} \right] \quad \text{Equation 2.3}$$

where  $k_B$  is the Boltzmann constant<sup>9</sup> and  $T$  is the absolute temperature.  $l_p$  is the persistence length of the polymer and describes its rigidity. Values for  $l_p$  are specific for each polymer and must be experimentally determined (163). A persistence length of 4 Å has been successfully applied to describe the extension at forces higher than 50 pN (152, 156). F-D curves recorded upon unfolding of single polypeptides can be fitted using the WLC model (164). The contour length  $L_c$  (in aa) obtained from fitting a force peak using the WLC model describes the length of the polypeptide that had been unfolded and stretched. The WLC model was used throughout all projects in the work presented here.

### 2.8.3 Dynamic force spectroscopy (DFS)

The mechanical stability of an interaction cannot be adequately characterized by its strength. In addition to the strength, the lifetime of an interaction has to be taken into consideration.

Dynamic force spectroscopy (DFS) is an extension of SMFS. DFS probes molecular bonds at different loading rates (applied force over time), allowing the approximation of the transition state and kinetic rate of the energy barrier of the bond (165).

Usually, the bound state of an interaction is characterized by the state of the lowest energy. Thus, in order to disrupt an interaction, it has to be transferred from this local energy minimum into the unbound state of unknown energy. To do so, the unfolding energy barrier must be overcome by a sufficient amount of energy in the direction of the reaction coordinate. The investigation of the folding and unfolding of soluble proteins revealed that these processes could be described by a two-state model (166, 167). In this model, folded structures exist either in a low-energy, low-entropic conformation, which corresponds to the native folded state. The high-energy, high-entropic state corresponds to the unfolded

---

<sup>9</sup>  $k_B = 1.38 \cdot 10^{-23}$  J/K

state of the protein. Both states are separated by an energy barrier (**Figure 2.3A**). The unfolding process can be modeled as a thermally driven overdamped first-order kinetic process in an aqueous environment described by the unfolding rate  $k_0$ , which is given by

$$k_0 = \tau_D^{-1} \exp\left(-\frac{\Delta G_0^\ddagger}{k_B T}\right) \quad \text{Equation 2.4}$$

where  $\tau_D$  is the diffuse relaxation time, which lies in the range of  $10^{-7}$ - $10^{-9}$  s (168, 169) and  $\Delta G_0^\ddagger$  is the activation free energy. **Equation 2.3** gives the expression for the spontaneous unfolding rate in the absence of applied force.

Since most proteins are kept in their native conformation by non-covalent interactions with limited lifetime, these bonds can break even in the absence of any applied force. According to **Equation 2.4**, the unfolding rate  $k_0$  increases when the activation free energy  $\Delta G_0^\ddagger$  decreases. Application of an externally applied unfolding force  $F$  leads to a decrease in  $\Delta G_0^\ddagger$ :

$$\Delta G^\ddagger(F) = \Delta G_0^\ddagger - F x_\beta \quad \text{Equation 2.5}$$

where  $x_\beta$  is the length along the reaction coordinate.  $x_\beta$  is defined by

$$x_\beta = x_u \cos(\theta) \quad \text{Equation 2.6}$$

Thus, application of an external unfolding force adds a mechanical unfolding potential ( $-F \cos(\theta) x_u$ ), which results in a tilt in the energy landscape (**Figure 2.3B**).  $x_u$  is the distance between folded and the transition state along the reaction coordinate, whereas  $\theta$  is the angle of the externally applied force relative to the reaction coordinate. For single-molecule force experiments it can be assumed that  $\theta$  is small, so that  $x_\beta \approx x_u$ . Therefore, the unfolding rate under an externally applied force  $F$  is given by

$$k(F) = \tau_D^{-1} \exp\left(-\frac{\Delta G_0^\ddagger - F x_u}{k_B T}\right) \quad \text{Equation 2.7}$$

The transition rate across the energy barrier and the force required to break an interaction both depend on the rate and duration of the

applied force (165, 170, 171). The most probable unfolding force  $F^*$  depends on the most probable loading rate  $r_f^*$ , which is the slope of a force peak multiplied by the speed of unfolding (165, 171):

$$F^* = \frac{k_B T}{x_u} \ln \left( \frac{x_u r_f^*}{k_B T k_0} \right) \quad \text{Equation 2.8}$$

In general, AFM-based SMFS does not allow performing experiments under equilibrium conditions. Nevertheless, biophysicists are interested in parameters that describe the untilted energy landscape at equilibrium, such as  $x_u$ ,  $k_0$  and  $\Delta G_0^\ddagger$ . To extract these parameters, one needs to measure the most probable unfolding force  $F^*$  of a rupture event at different loading rates using DFS. The data obtained from these DFS unfolding experiments can be fitted using **Equation 2.8**. The ground-to-transition state distance  $x_u$  can be obtained from the slope of the DFS fit ( $F^*$  vs  $\ln(r_f^*)$ ). The height of the activation energy barrier  $\Delta G_0^\ddagger$  can be calculated using an the Arrhenius equation:

$$\Delta G_0^\ddagger = -k_B T \ln(\tau_D k_0) \quad \text{Equation 2.9}$$

The energy landscape illustrated in **Figure 2.3** is an oversimplification, since the structures of soluble and membrane proteins are stabilized by weak non-covalent interactions, for example ionic bonds, hydrogen bonds and van-der-Waals interactions. These interactions break when the protein is transferred from the native state into the completely stretched and unfolded state. Thus, a large number of energy barriers have to be overcome during the folding or unfolding of a protein, which results in a rough energy landscape as indicated in **Figure 2.3** (172-176). Therefore, DFS experiments locate and quantify only the most prominent energy barriers, while minor energy barriers might not be detected.

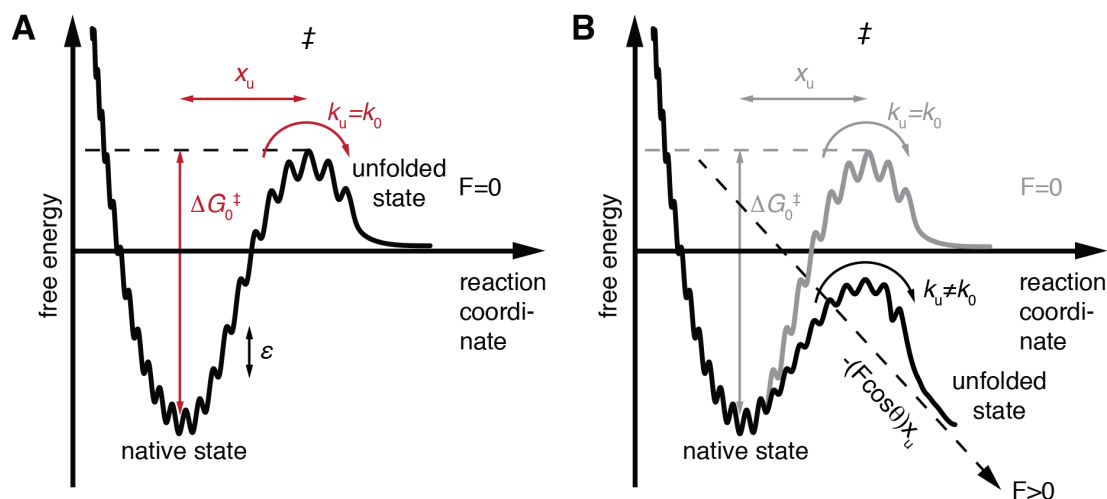


**Figure 2.3: Free energy unfolding barrier describing energetic ( $\Delta G_0^\ddagger$ ) and kinetic ( $k_0$  and  $x_u$ ) parameters of stable structural segments.** (A) According to the Bell-Evans model (165, 177), folded structures can be characterized using a simple two-state model. The native, folded structure resides in an energy valley and is separated by an energy barrier from the unfolded state. As approximated previously the surface roughness of the energy landscape of transmembrane  $\alpha$ -helices,  $\varepsilon$ , is  $\approx 4-6 k_B T$  (178). This roughness creates local energy minima that can stabilize functionally related conformational states of a structural segment. Thus, for a given surface roughness, a wide energy valley can host more conformational states (*i.e.*, hosts a higher conformational variability) of a structural segment compared to a narrow energy valley. The transition state ( $\ddagger$ ) has to be overcome to induce unfolding of the stable structural segment.  $x_u$  represents the distance between the folded state and the transition state,  $k_u$  is the transition rate for crossing the energy barrier under zero force, and  $\Delta G_0^\ddagger$  gives the activation energy for unfolding the segment. (B) Applying an external force  $F$  changes the thermal likelihood of reaching the top of the energy barrier. The energy profile along the reaction coordinate (pulling direction) is tilted by the mechanical energy  $-F \cos(\theta)x_u$ , as indicated by the dashed line. The applied force does not change the ground-to-transition state distance  $x_u$ .  $\theta$  describes the angle of the externally applied force relative to the reaction coordinate. As a result of this tilt, the energy barrier that separates the folded from the unfolded state decreases and the probability of the folded structural segment to unfold increases.

### **3 Molecular interactions of the human G protein-coupled $\beta_2$ adrenergic receptor**

Parts of this work have been submitted to *PNAS* and *Structure* for consideration.

#### *Publications*

M. Zocher *et al.* (2012), *Structure*

M. Zocher *et al.* (2012), submitted

#### *Author contributions*

**Michael Zocher**: Experimental planning and setup, SMFS experiments, SFMS data analysis, figure preparation & manuscript writing

Juan J. Fung & Cheng Zhang: Preparation of  $\beta_2$ AR proteoliposomes

Søren G. F. Rasmussen: Bimane fluorescence stain of  $\beta_2$ AR

Brian K. Kobilka & Daniel J. Müller: Project initiation and supervision



### **3.1 Introduction**

Over the past four years remarkable advances in the structural biology of G protein-coupled receptors (GPCRs) have been made. One of the highlights includes solving the crystal structure of the human  $\beta_2$  adrenergic G protein-coupled receptor ( $\beta_2$ AR) (65, 66), an outstanding success of great interest, in particular from the perspective of membrane-protein biophysics.

#### **3.1.1 Multifaceted functionality of GPCRs**

What is it that makes this family of membrane proteins so interesting? First of all, GPCRs are the largest family of membrane proteins mediating most cellular responses to hormones and neurotransmitters. Furthermore, GPCRs are responsible for olfaction, taste and vision. All GPCRs contain seven membrane-spanning  $\alpha$ -helical segments, which are separated by alternating intracellular and extracellular loops. In vertebrates, GPCRs can be divided into five families. Depending on their sequence and structural similarity, they are divided into rhodopsin-like (family A), secretin (family B), glutamate (family C), adhesion and frizzled/taste2 (179). The rhodopsin family is by far the largest and most diverse of these families. Members of family A are characterized by conserved sequence motifs implying shared activation mechanisms and structural features. Nevertheless, individual GPCRs have unique combinations of signal-transduction activities that involve multiple G protein subtypes. In addition, they initiate complex regulatory processes (180). Due to their broad influence over human physiology and behavior, GPCRs are promising targets for new and more effective drugs.

The  $\beta_2$ AR is one of the best-characterized GPCRs.  $\beta_2$ AR belongs to the class A GPCRs and is expressed in pulmonary and cardiac myocyte tissue (181, 182). Together with its close relative  $\beta_1$ AR,  $\beta_2$ AR senses adrenalin in bronchial vasculature and noradrenalin in cardiac muscle. The implication in a broad spectrum of diseases like asthma or heart failure makes  $\beta_2$ AR an important therapeutic target (183-187). Numerous

ligands that bind to  $\beta_2$ AR are used as drugs in cardiac disease and asthma treatment (183). Several crystal structures of  $\beta_2$ AR have been determined over the last years (65, 66, 188-191), providing unique insights into structure-function relationships of GPCRs.

In general, the classical role of a GPCR is to couple the binding of agonists to activation of specific heterotrimeric G proteins, which leads to the modulation of downstream effector proteins. In the case of  $\beta_2$ AR, binding of adrenalin and noradrenalin to cells in the target tissues of sympathetic neurotransmission leads to activation of  $G_{\alpha s}$ , the stimulatory subunit of the heterotrimeric G protein.  $G_{\alpha s}$  stimulates adenylylate cyclase, cyclic (cAMP) accumulates, the cAMP-dependent protein kinase A (PKA) is activated, and proteins involved in muscle-cell contraction are phosphorylated (192). Nevertheless, in recent years it has been shown that many GPCRs exhibit a much more complex signaling behavior. For instance,  $\beta_2$ AR has a significant constitutive activity, which can be blocked by inverse agonists (193, 194). Besides  $G_{\alpha s}$ ,  $\beta_2$ AR couples to the inhibitory subunit  $G_{\alpha i}$  in cardiac myocytes (195).  $\beta_2$ AR can also signal in a G protein-independent manner: binding of arrestin to  $\beta_2$ AR triggers MAP kinase pathways (196, 197). Additionally, desensitization of  $\beta_2$ AR involves multiple pathways that include phosphorylation of the receptor, arrestin-mediated internalization into endosomes, recycling of the receptor and lysosomal degradation (198, 199) (**Figure 3.1**). Finally, these activities are further complicated by oligomerization of GPCRs (200) and localization to specific membrane compartments (201), which results in differences in the composition of the lipid bilayer. Drugs can preferentially activate or inhibit these different signaling pathways. This shows that the functional behavior of GPCRs is highly complex and multifaceted.

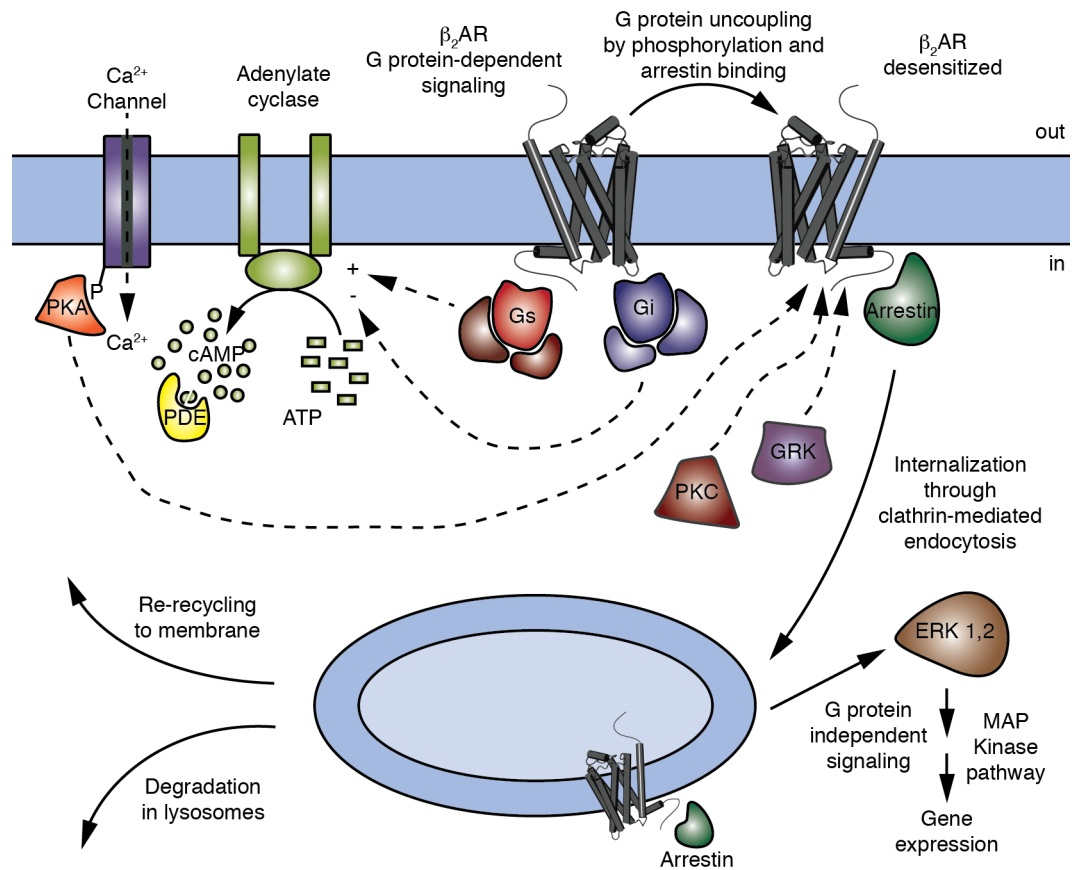


**Figure 3.1: Signal transduction pathways induced by  $\beta_2$ AR.** A multitude of signaling pathways are regulated by  $\beta_2$ AR. The receptor can activate two G proteins (Gs and Gi). Both G proteins differentially regulate adenylate cyclase. Adenylate cyclase generates cyclic AMP (cAMP), a second messenger, which activates protein kinase A (PKA). PKA regulates the activity of several cellular proteins, for example the L-type  $\text{Ca}^{2+}$  channel and also  $\beta_2$ AR itself. Specific phosphodiesterase proteins (PDEs) downregulate cAMP levels. Activation of  $\beta_2$ AR further leads to phosphorylation of  $\beta_2$ AR by a G protein-coupled receptor kinase (GRK) followed by coupling of arrestin, a signaling and regulatory protein. Arrestin promotes the activation of extracellular signal-regulated kinases (ERK). Moreover, it prevents the activation of G proteins and stimulates internalization of the receptor *via* clathrin-mediated endocytosis. Protein kinase C (PKC) is another protein that can phosphorylate the receptor. Adapted from (180).

### 3.1.2 Cholesterol and GPCRs

Cellular membranes functionally modulate a large number of membrane proteins (16, 202-206). Such functional modulation is facilitated by chemical and physical interactions between membrane proteins and phospholipids, sphingolipids, cholesterol and other molecular

components of the cell membrane. Similar to many other membrane proteins, GPCRs are regulated by their hetero- and homooligomeric assembly and the membrane composition. Because the heterogeneous composition of cellular membranes changes dynamically, the functional state of GPCRs depends on the location in the cell membrane and on the state of the cell (207, 208). The steroid cholesterol modulates chemical and physical properties of cellular membranes and plays a role in the dynamic formation of sphingolipid-enriched assemblies of lipids and membrane proteins. These metastable assemblies, or lipid rafts, can functionally regulate membrane proteins by different mechanisms (207). Indirect regulation of membrane proteins, including GPCRs, can be observed through the ability of cholesterol to modulate biophysical properties of a lipid bilayer (14) whereas the direct regulation of membrane proteins can occur through specific interactions (209-212). Although it is not completely understood how cells control the distribution of cholesterol and by which mechanisms cholesterol functionally regulates GPCRs, insights into these processes are of cell biological and pharmacological importance (213, 214).

Similar to other GPCRs cholesterol modulates the physiological function of  $\beta_2$ AR (213, 215). Furthermore, cholesterol and the more water-soluble cholesterol analog cholesteryl hemisuccinate (CHS) enhance the thermal stability of  $\beta_2$ AR (213, 216). Additionally, cholesterol facilitates interactions between GPCRs and appears helpful to crystallize  $\beta_2$ AR (65). A recently published X-ray crystallography model of human  $\beta_2$ AR showed cholesterol to fit into a shallow surface groove formed by transmembrane  $\alpha$ -helices H1, H2, H3 and H4 (217). This structural model unraveled possible interactions between cholesterol and  $\beta_2$ AR. However, to understand to which extent the interactions established by cholesterol change kinetic, energetic, and mechanical properties of structural regions in the receptor requires additional insight.

### 3.1.3 Ligands and their efficacy profiles

What are the biophysical mechanisms behind the complex functional behavior of GPCRs? The biochemical and biophysical properties of GPCRs can be modulated in a ligand-specific manner (218). Ligands are classified by their efficacy. The efficacy of a ligand reflects its effect on the structure and biophysical properties of a receptor. Depending on the biological response, ligands can be grouped into different efficacy classes (**Figure 3.2**). Full agonists are able to maximally stimulate the receptor, whereas partial agonists are unable to elicit full activity, even at saturating concentrations. Neutral antagonists can prevent other ligands from binding to the receptor, but they have no effect on signaling activity. Inverse agonists decrease the level of agonist-independent basal activity.

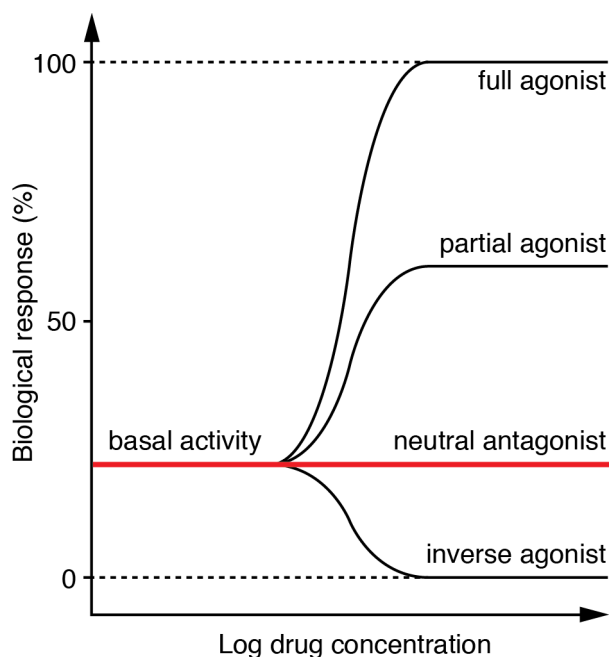


**Figure 3.2: Classification of ligand efficacy for GPCRs.** Many GPCRs exhibit basal or constitutive activity, which is independent from agonists (red line). Inverse agonists inhibit basal activity, whereas neutral antagonists have no effect. Agonists (and partial agonists) initiate biological responses above the basal activity. Note that efficacy is not directly related to affinity.

The wide spectrum of ligand efficacies for GPCRs implies that efficient energy transfer between the binding pocket and G protein binding site depends on multiple interactions between receptor and ligand. Apparently, the energy transfer requires more than simply occupying the ligand-binding site. Biophysical studies on fluorescently labeled  $\beta_2$ AR showed that full and partial agonists with different subsets of functional groups stabilize distinct conformational states of the receptor (219-221). These findings led to a complex picture of GPCR

activation: a distinct conformation stabilized by the structure of a ligand determines the efficacy towards a specific pathway. Many GPCRs are capable of activating multiple signaling pathways (see section 3.1.1), and specific ligands can have a different relative efficacy to different pathways (222). Even opposite activities for different signaling pathways are observed: for  $\beta_2$ AR, agonists that induce the arrestin/MAP kinase pathway can also act as inverse agonists for the classical G $\alpha$ s/cAMP/PKA pathway (196, 223). Thus, GPCRs are no longer thought to act like simple two-state switches. By now, they are regarded as molecular rheostats, having the ability to sample a continuum of conformations with relatively closely spaced energies (224). There is evidence from biochemical and biophysical data showing that GPCRs are flexible and dynamic molecules and that functionally distinct ligands can stabilize specific conformations of the receptor (224).

In the following sections, it was investigated how these conformations, or interactions, change their dynamic energy profile. For that purpose, the dynamic energy landscape of  $\beta_2$ AR was determined using DFS. Finally, it was investigated how physiologically relevant variables, such as cholesterol and ligands, modulate the energy landscape of  $\beta_2$ AR.

## **3.2 Experimental procedures**

### **3.2.1 Preparation of $\beta_2$ AR proteoliposomes**

$\beta_2$ AR-containing proteoliposomes were kindly provided by Brian Kobilka (Stanford University). *Spodoptera frugiperda* (Sf9) insect cells were grown at 27°C in suspension cultures in ESF-921 medium (Expression Systems, USA) supplemented with 0.5 mg/ml gentamicin. The Bac-to-Bac® Baculovirus Expression System (Invitrogen, USA) was used for generating baculovirus for the  $\beta_2$ AR. Throughout this project, a modified construct of human  $\beta_2$ AR with a truncated C-terminal end (48 amino acids (aa)) and a N-terminal FLAG epitope followed by a TEV protease cleavage site was used.  $\beta_2$ AR expression was accomplished by

infecting Sf9 cells at a density of  $\approx 3 \times 10^6$  cells/ml for  $\approx 48$  h. Cells expressing receptors, as assessed by immunofluorescence, were harvested by centrifugation (15 min at 5000g). Cell pellets were stored at  $-80$  °C. From these pellets  $\beta_2$ AR was purified using a three-step purification procedure as described (225). For preparation of lipids, 1,2-dioleoyl-sn-glycero-3-phosphocholine (DOPC) (Avanti Polar Lipids, USA) and the cholesterol analog cholesteryl hemisuccinate (CHS) (Steraloids, USA) were mixed and dissolved in chloroform to form a stock solution of lipids at concentrations of 20 mg/ml and 10 mg/ml. DOPC and CHS were added to a glass vial, with DOPC at a 10-fold excess, and the chloroform was evaporated under a fine stream of argon. To prepare DOPC lipids without cholesterol, CHS was excluded from all preparation steps. The lipids were then dried under vacuum for 1 h. After this, the lipids were resuspended in 100 mM NaCl, 1% (w/v) octylglucoside, 20 mM HEPES, pH 7.5, vortexed and sonicated for 1 h in an ice water bath. The lipid mixture was stored at  $-80$ °C.

$\beta_2$ AR was reconstituted as described previously (225). Briefly, 300  $\mu$ l samples were prepared containing lipid and the  $\beta_2$ AR at a lipid-to-receptor ratio of 1,000:1 (mol:mol). The lipid/receptor mixture was mixed with reconstitution buffer (100 mM NaCl, 20 mM HEPES, pH 7.5) at a final volume of 300  $\mu$ l and placed on ice for 2 h. Vesicles were formed removing detergent on a Sephadex G-50 (fine) column (25 x 0.8 cm) using reconstitution buffer. To bind ligands,  $\beta_2$ AR in DOPC/CHS liposomes was pre-incubated for 1 h at room temperature ( $\approx 22$ °C) with saturating amounts (10  $\mu$ M for BI-167107 (BI, Boehringer-Ingelheim), THRX-144877 (THRX, Theravance) and carazolol, 100  $\mu$ M for alprenolol and 100  $\mu$ M for adrenalin). During subsequent reconstitution steps, the same concentration of ligand was included in the reconstitution buffer.

### **3.2.2 SMFS and DFS**

SMFS was conducted using two different AFMs that provided similar results (ForceRobot 300, JPK Instruments, Germany and Nanoscope IIIa PicoForce AFM, Bruker, Germany). SMFS data of  $\beta_2$ AR

were recorded at pulling velocities of 100, 300, 600, 900, 1200, 2500 and 5000 nm/s. SMFS at pulling velocity of 5000 nm/sec was recorded using an additional 16-bit data acquisition hardware (Nanoscope IIIa: NI PCI-6221; ForceRobot 300: NI PCI-6251, National Instruments, Germany). Cantilevers used (60  $\mu$ m long silicon nitride A-BioLever, BL-RC150 VB, Olympus Ltd., Japan) had nominal resonance frequencies of  $\approx$ 8 kHz in water. Cantilever spring constants ( $\approx$ 30 pN/nm) were determined in buffer solution using the equipartition theorem (226, 227) prior to experiments. Due to uncertainties in calibrating the cantilever spring constant ( $\approx$ 10%),  $\beta_2$ AR was unfolded using at least five different cantilevers for each velocity. Proteoliposomes containing  $\beta_2$ AR were adsorbed over night at 4°C onto freshly cleaved mica in SMFS buffer (300 mM NaCl, 25 mM MgCl<sub>2</sub>, 25 mM Tris, pH 7.0). Mica is an atomically flat, chemically inert and hydrophilic surface, which so far did not significantly influence the structure-function relationship of membrane proteins and their interactions probed by SMFS (93, 123, 138, 156). To remove weakly attached membrane patches, the sample was rinsed several times with SMFS buffer. SMFS buffer solutions were prepared using nanopure water ( $\geq$ 18 MOhm/cm; PURE-LAB Ultra, ELGA LabWater) and pro-analysis grade ( $\geq$ 98.5%) chemicals from Sigma-Aldrich or Merck. All SMFS experiments were performed under identical SMFS buffer conditions at 24°C. To characterize ligand binding, SMFS buffer was supplemented with adequate amounts of the ligand. To attach a single  $\beta_2$ AR *via* unspecific interactions, the AFM stylus was pushed onto proteoliposomes, applying a constant force of 700 pN for 0.5 s. The unspecific attachment between AFM stylus and terminal end of the  $\beta_2$ AR polypeptide chain is strong enough to withstand pulling forces of  $\approx$ 2 nN (93, 228). Separation of stylus and membrane stretched the polypeptide and exerted a force at the protein. At sufficiently high pulling force  $\beta_2$ AR unfolded stepwise. Unfolding events were monitored recording the cantilever deflection and the distance separating cantilever stylus and membrane. Interaction forces were calculated from the cantilever deflection using Hook's law.

### **3.2.3 Data selection**

Mechanical unfolding of  $\beta_2$ AR was recorded by F-D curves. Each force peak of a F-D curve denoted the rupture of an unfolding barrier established by a structural segment of  $\beta_2$ AR. The distance at which a force peak was detected assigned the contour length of the unfolded and stretched polypeptide that tethered the AFM stylus and the anchoring structural segment. The very last force peak of a F-D curve represented the unfolding of the last structural segment remaining anchored by the lipid bilayer (159). Overcoming the stability of this last segment lead to complete unfolding of the receptor, followed by extraction from the membrane. In the GPCR bovine rhodopsin, the last structural segment (or unfolding barrier) corresponds to  $\alpha$ -helix H8, which lies parallel to the membrane bilayer followed by a palmitoylation site (229). It was assumed that this was also the case for  $\beta_2$ AR since it shares very similar structural features with rhodopsin. A fully stretched  $\beta_2$ AR polypeptide that remains anchored by  $\alpha$ -helix H8 would show a contour length of  $\approx 260$  to 290 aa. Therefore, F-D curves showing a maximum length of 70-90 nm ( $\approx 260$  to 290 aa) were selected for data analysis.

### **3.2.4 Data analysis**

Every force peak of a F-D curve was fitted using the WLC model (161) (see section 2.8.2). A persistence length  $P$  of 0.4 nm and a backbone length of 0.36 nm were assumed for every aa. The contour length  $L_c$  (in aa) obtained from fitting a force peak using the WLC model describes the length of the polypeptide that had been unfolded and stretched. Contour lengths and rupture forces were statistically analyzed for every reproducibly occurring force peak using built-in and custom procedures of IgorPro 6 (WaveMetrics, USA). To generate density maps, F-D curves were superimposed and aligned to the characteristic force peak detected at the contour length of 121 aa.

### **3.2.5 Assignment of stable structural segments**

The contour length determined by the WLC fits corresponds to the length of the unfolded and stretched  $\beta_2$ AR polypeptide that tethers AFM

stylus and a structural unfolding intermediate. Thus, every force peak could be used to assign the end of the previous and the beginning of the following structural segment that stabilized  $\beta_2$ AR against unfolding (125). Some stable structural segments had to be assumed to begin at the cytoplasmic  $\beta_2$ AR surface at the opposite side of the pulling AFM stylus. To locate the beginning of such a stable structural segment, the so-called ‘membrane compensation procedure’ was applied (125, 159). Thereto, the thickness of the membrane ( $\approx 4$  nm) was added to the contour length of the corresponding force peak (125, 159). Accordingly,  $\approx 11$  aa ( $11 \text{ aa} \cdot 0.36 \text{ nm/aa}$ ) were added to the contour length of a force peak. If the beginning of a stable structural segment was located within the membrane, less aa were added to the contour length.

### **3.2.6 Calculation of $x_u$ and $k_0$**

The Bell-Evans theory (177) describes the most probable unfolding force  $F^*$  as a function of the most probable loading rate  $r_f^*$  to reveal insight into the unfolding energy barrier that stabilizes a structural segment against unfolding (171) (see section 2.8.3). Using a non-linear least squares algorithm, the parameters  $x_u$  and  $k_0$  were obtained by fitting **Equation 2.8** to a DFS plot. The loading rate was calculated using  $r_f = k_{spacer} v$ , where  $k_{spacer}$  is the spring constant of the stretched polypeptide and  $v$  is the pulling velocity.  $k_{spacer}$  corresponds to the slope of a force peak before rupture. Experimental force and loading rate histograms were fitted using Gaussian distributions.

### **3.2.7 Calculation of transition barrier height and rigidity**

The free energy barrier  $\Delta G_0^\ddagger$  separating the unfolded from the folded state was calculated using **Equation 2.9**. In the calculations,  $\tau_D = 10^{-8}$  s was used. Varying  $\tau_D$  in the range mentioned in section 2.8.3 would change  $\Delta G_0^\ddagger$  by  $<15\%$ . Furthermore, the influence of errors of  $\tau_D$  would be the same for all conditions and  $\Delta G_0^\ddagger$  values, even if  $\tau_D$  was wrong by orders of magnitude. Errors in  $\Delta G_0^\ddagger$  were calculated by propagation of errors of  $k_0$ . Without having information on the energy potential shape, a simple

parabolic potential was assumed. The mechanical spring constant  $\kappa$  of a structural segment was calculated using  $\Delta G_0^\ddagger$  and  $x_u$  (230) with the following equation:

$$\kappa = \frac{2\Delta G_0^\ddagger}{x_u^2} \quad \text{Equation 3.1}$$

To estimate errors in  $\kappa$ , errors in  $\Delta G_0^\ddagger$  and  $x_u$  were propagated.

### 3.3 Cholesterol dependent interactions of $\beta_2$ AR

#### 3.3.1 Results

##### 3.3.1.1 SFMS of human $\beta_2$ AR in the presence and absence of cholesterol

To characterize the influence of cholesterol on the interactions stabilizing human  $\beta_2$ AR, the receptor was reconstituted into liposomes containing phospholipids (DOPC) or phospholipids and cholesteryl hemisuccinate (DOPC/CHS) (see section 3.2.1). For SMFS,  $\beta_2$ AR the proteoliposomes were densely adsorbed onto freshly cleaved mica (**Figure 3.3**). The AFM stylus was pushed onto the proteoliposomes with a force of  $\approx 700$  pN for 0.5 s (**Figure 3.4A**). Subsequently, the cantilever was retracted, and its deflection recorded as a force-distance (F-D) curve. In  $\approx 0.5\%$  of these approach-and-retract cycles, a single  $\beta_2$ AR attached to the AFM stylus and the F-D curve recorded during retracting the cantilever showed a sawtooth-like pattern with several force peaks. These sawtooth-like patterns were similar for  $\beta_2$ AR reconstituted in DOPC (**Figure 3.4B**, top) and DOPC/CHS liposomes (**Figure 3.4C**, top). Each force peak of a F-D curve reflected the unfolding of a structural segment of  $\beta_2$ AR. The magnitude of the force peak revealed the strength of the interaction that stabilized a structural segment against unfolding. These interactions were composed of inter- and intramolecular interactions. For analysis only F-D curves with an overall length of  $\approx 70$ -90 nm were selected, since they describe the complete unfolding of the receptor from its terminus (see section 3.2.3). To highlight common features among the F-D curves, they were superimposed and displayed as density plots (**Figure 3.4B,C**,

bottom). The superimpositions of F-D curves recorded of  $\beta_2$ AR reconstituted in DOPC (**Figure 3.4B**) and DOPC/CHS (**Figure 3.4C**) showed a characteristic pattern of eight force peaks. The presence of cholesterol did not change the position of the force peaks. However, the magnitude of the force peaks increased in presence of cholesterol (**Figure 3.5**). This difference implies that cholesterol increases the strength of interactions stabilizing  $\beta_2$ AR.

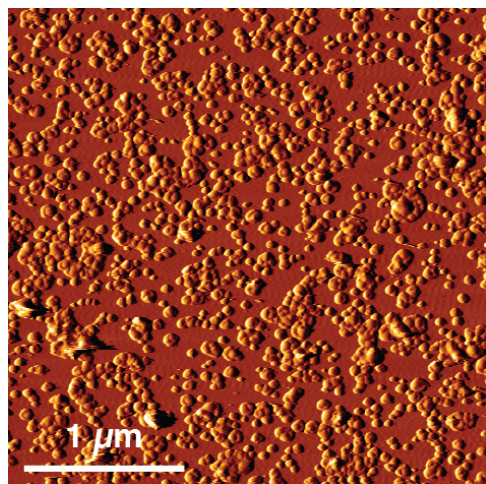


**Figure 3.3: AFM deflection image of  $\beta_2$ AR proteoliposomes.** Proteoliposomes were adsorbed over night at 4°C onto freshly cleaved mica in buffer solution (300 mM NaCl, 25 mM MgCl<sub>2</sub>, 25 mM Tris, pH 7.0). To remove weakly attached membrane patches, the sample was rinsed several times with the same buffer solution. The contact mode AFM deflection image was recorded in buffer solution applying an imaging force of  $\approx$ 50-100 pN.

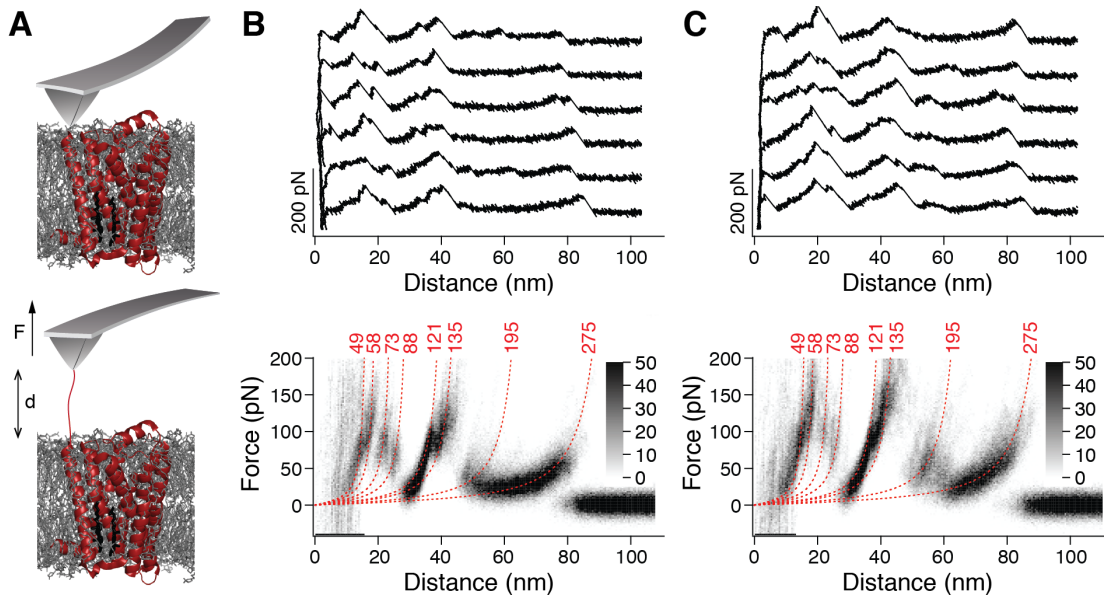


**Figure 3.4: SMFS of  $\beta_2AR$  reconstituted into liposomes composed of either phospholipids (DOPC) or phospholipids and cholesterol (DOPC/CHS).** (A) Pressing the AFM stylus onto the proteoliposomes promotes the unspecific attachment of a single  $\beta_2AR$  polypeptide to the stylus. Withdrawal of the AFM cantilever stretches the polypeptide and induces the sequential unfolding of  $\beta_2AR$ . F: force, d: distance. (B, C) Selection of force-distance (F-D) curves recorded upon N-terminal unfolding of  $\beta_2AR$  reconstituted into DOPC (B, top) and DOPC/CHS liposomes (C, top). Density plots of superimposed F-D curves (bottom of (B) and (C)) highlight their common features. Number of superimposed F-D curves  $n=100$  (B) and  $n=100$  (C). Red numbers on top of each WLC curve (red dashed lines) indicate the average contour lengths (in amino acids) revealed from fitting each force peak of each superimposed F-D curve. Gray scale bars allow evaluating how frequently individual force peaks were populated.

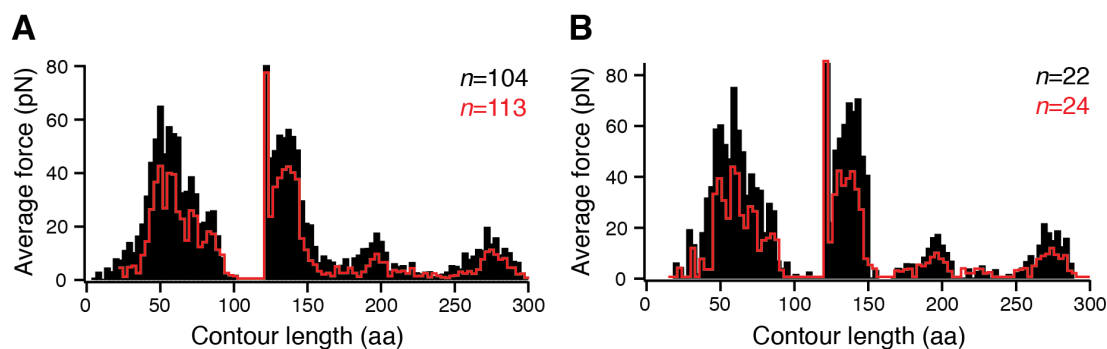


**Figure 3.5: Average force required to unfold structural segments of  $\beta_2$ AR reconstituted into liposomes composed of phospholipids (DOPC) or of phospholipids and cholesterol (DOPC/CHS).** (A) On average the force required to unfold  $\beta_2$ AR reconstituted into DOPC/CHS liposomes (black) was higher than the average force required to unfold  $\beta_2$ AR reconstituted into DOPC liposomes (red). This difference implies an increased mechanical stability of the GPCR in the presence of cholesterol. To determine average unfolding forces the sum of unfolding forces detected for every peak of every force-distance spectrum used in superimpositions shown in **Figure 3.4B** and **Figure 3.4C** was calculated. This sum of forces was then divided by the number of all analyzed F-D curves. (B) To exclude that differences in average forces are not a result of cantilever calibration errors,  $\beta_2$ AR in DOPC (red) and DOPC/CHS (black) liposomes was unfolded under identical experimental conditions using the same cantilever. Bin sizes of histograms are 3 aa. The pulling velocity was 300 nm/s (A) and 528 nm/s (B). The numbers ( $n$ ) of analyzed F-D curves are indicated.

### 3.3.1.2 Unfolding $\beta_2$ AR from N- and C-terminal ends

In principle  $\beta_2$ AR could attach non-specifically with either the N- or the C-terminal end to the AFM stylus. Accordingly, two different unfolding F-D spectra were recorded (**Figure 3.6**). To assign these classes to N- or C-terminal unfolding, the N-terminal FLAG tag was enzymatically removed and the shortened  $\beta_2$ AR was unfolded (**Figure 3.7**). A shift of  $\approx 14$  aa was observed in one class of F-D curves, suggesting that this particular class corresponds to N-terminal unfolding. Approximately 75% of the F-D curves ( $n \approx 1000$ ) corresponded to unfolding of  $\beta_2$ AR by mechanically pulling the N-terminal end (**Figure 3.6A**). The remaining F-D curves represented unfolding the receptor from the C-terminal end (**Figure 3.6B**). The superimpositions of F-D curves showed a characteristic pattern of eight force peaks when unfolding  $\beta_2$ AR from

the N-terminal end (**Figure 3.6A**, bottom). When unfolding  $\beta_2$ AR from the C-terminal end, only four reproducible force peaks were detected (**Figure 3.6B**, bottom). The C-terminal region of the receptor, which is unfolded at pulling distances  $<30$  nm, did not reveal reproducible unfolding events (force peaks) (**Figure 3.6B**). In summary, F-D curves recording the unfolding of  $\beta_2$ AR from the N-terminal end occurred at higher probability and, most importantly, detected more unfolding events and interactions of the GPCR. For these reasons, only F-D curves that were recorded upon unfolding of  $\beta_2$ AR from the N-terminus were analyzed.

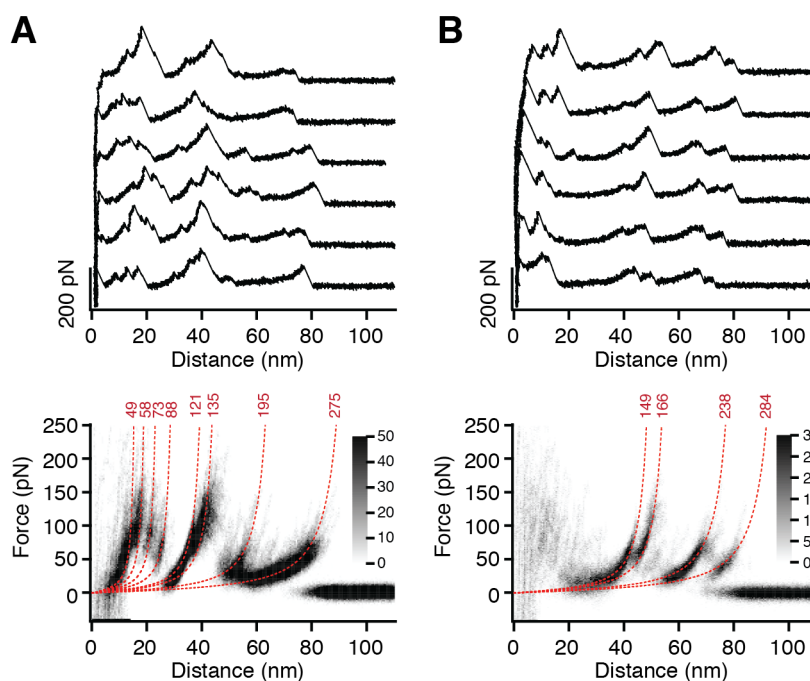


**Figure 3.6: N- and C-terminal unfolding of  $\beta_2$ AR reconstituted into DOPC/CHS liposomes.** Selection of force-distance (F-D) curves recorded upon N-terminal (**A**, top) and C-terminal (**B**, top) unfolding of  $\beta_2$ AR. Superimpositions of F-D curves (density plots at bottom of **(A)** and **(B)**) highlight their common features. Red dashed lines represent WLC fits of the force peaks and the numbers on top of the curves indicate the average contour lengths (in amino acids) revealed from the WLC fits. Gray scale bars allow evaluating how frequently individual force peaks were populated. SMFS data recorded in SMFS buffer (300 mM NaCl, 25 mM Tris, 25 mM  $\text{MgCl}_2$ , pH 7.0). Number of superimposed F-D curves  $n=103$  (**A**, bottom) and  $n=56$  (**B**, bottom).

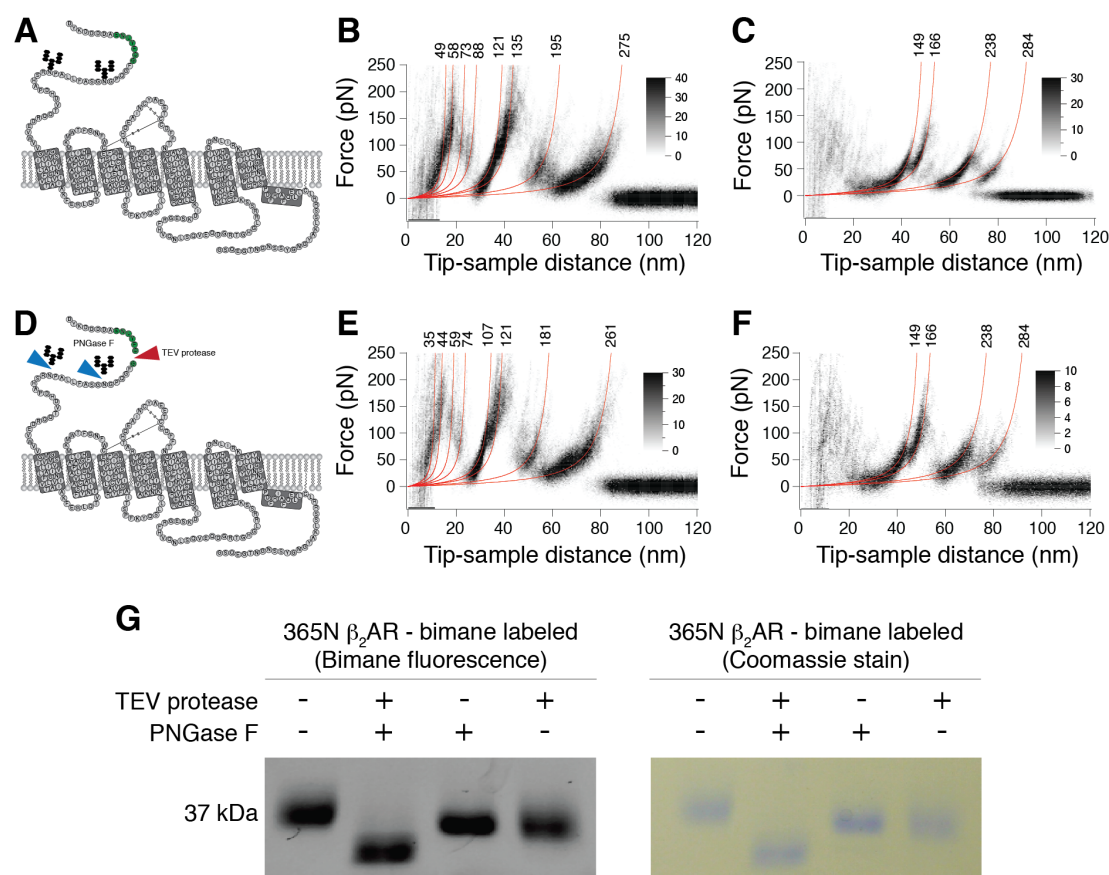


**Figure 3.7: Unfolding  $\beta_2$ AR after removal of the FLAG-Tag.** (A) Secondary structure model of 365N  $\beta_2$ AR with N-terminal FLAG tag followed by a TEV protease cleavage site (colored in green). Superimposition of F-D curves recorded pulling N-terminal (B) and C-terminal (C) ends before TEV protease treatment. SMFS of the untreated receptor shows the normal full-length spectrum. Force peaks were fitted using the WLC model to reveal the contour length of the unfolded and stretched polypeptide (given at the end of each WLC fit in aa). (D) Treatment of  $\beta_2$ AR with TEV protease (red triangle) and PNGase F (blue triangles) removed 14 amino acids (aa) from the N-terminus and the glycosylations, respectively. (E) Superimposition of F-D curves recorded pulling the truncated N-terminal end of  $\beta_2$ AR after TEV protease treatment. On average the force peaks showed a shift of 14 aa. (F) Superimposition of F-D curves recorded pulling the C-terminal end of TEV protease treated  $\beta_2$ AR. The superimposition shows the spectrum of the untreated receptor. Data (B-F) recorded in buffer solution (300 mM NaCl, 25 mM MgCl<sub>2</sub>, 25 mM Tris, pH 7.0). (G) Bimane fluorescence and Coomassie stain of untreated, TEV protease and PNGase F treated bimane labeled  $\beta_2$ AR. The molecular weight was shifted on the gel after treatment with TEV, PNGaseF and both enzymes.

### 3.3.1.3 Mapping interactions that stabilize structural segments of $\beta_2$ AR

After having identified that the superimposed F-D spectra (**Figure 3.4B,C**, bottom) correspond to the unfolding of  $\beta_2$ AR from the N-terminal end (see previous section) the interactions were mapped to the  $\beta_2$ AR structure. When exerting sufficient force to the N-terminal end,  $\beta_2$ AR unfolds in a sequence of steps. Every force peak of the F-D curve reflects an unfolding step (**Figure 3.4B,C**, top). An unfolding step, in which a structural segment unfolds, describes the transfer of one unfolding intermediate to the next (125). To assign the unfolding steps and structural segments, every force peak of a F-D curve was fitted using the worm-like chain (WLC) model (see section 2.8.2). Each WLC fit revealed the contour length of the unfolded polypeptide that connected AFM stylus and the unfolding intermediate of the receptor. The contour lengths of all force peaks allowed determining all unfolding steps of  $\beta_2$ AR (**Figure 3.4B,C**, **Table 3.1**). In the first unfolding step the N-terminus and the N-terminal transmembrane  $\alpha$ -helix of  $\beta_2$ AR unfolded. Next, the unfolded polypeptide linking AFM stylus and the stable structural segments that remained folded and anchored in the membrane was elongated and stretched. As soon as the stretching force exceeded the stability of the next structural segment this segment unfolded as well. This sequential unfolding of one structural segment after the other continued until the entire  $\beta_2$ AR had been unfolded. In summary, eight unfolding steps were detected, each step reflecting the unfolding of a structural segment. Mapped onto the secondary and tertiary structure these stable structural segments show where inter- and intramolecular interactions stabilized  $\beta_2$ AR (**Figure 3.8**). Because the common unfolding peaks detected for  $\beta_2$ AR in the presence and in the absence of cholesterol showed no differences in their position (**Figure 3.4**), it could be concluded that cholesterol did not stabilize different structural segments (**Figure 3.8**). However, apparently the strength of the interactions stabilizing  $\beta_2$ AR depended on the presence of cholesterol (**Figure 3.5**). In the following the nature of these interactions was investigated.

**Table 3.1: Mean contour lengths of force peaks in F-D curves recorded during N-terminal unfolding of  $\beta_2AR$  and stable structural segments assigned to the force peaks.** Contour lengths represent mean peak positions. Errors represent standard deviations (SD). Number of analyzed F-D curves  $n=100$  (DOPC) and  $n=100$  (DOPC/CHS).

Stable structural segment	Contour length $\pm$ SD (aa)	
	DOPC	DOPC/CHS
[H1.1]	$49 \pm 4$	$49 \pm 4$
[H1.2-C1]	$58 \pm 4$	$58 \pm 3$
[H2.1]	$73 \pm 3$	$73 \pm 3$
[H2.2-E1]	$88 \pm 4$	$88 \pm 4$
[H3-C2-H4-E2-H5.1]	$121 \pm 0$	$121 \pm 0$
[H5.2-C3-H6.1]	$135 \pm 9$	$135 \pm 7$
[H6.2-E3-H7-H8]	$195 \pm 8$	$195 \pm 7$
[CT]	$275 \pm 13$	$275 \pm 11$

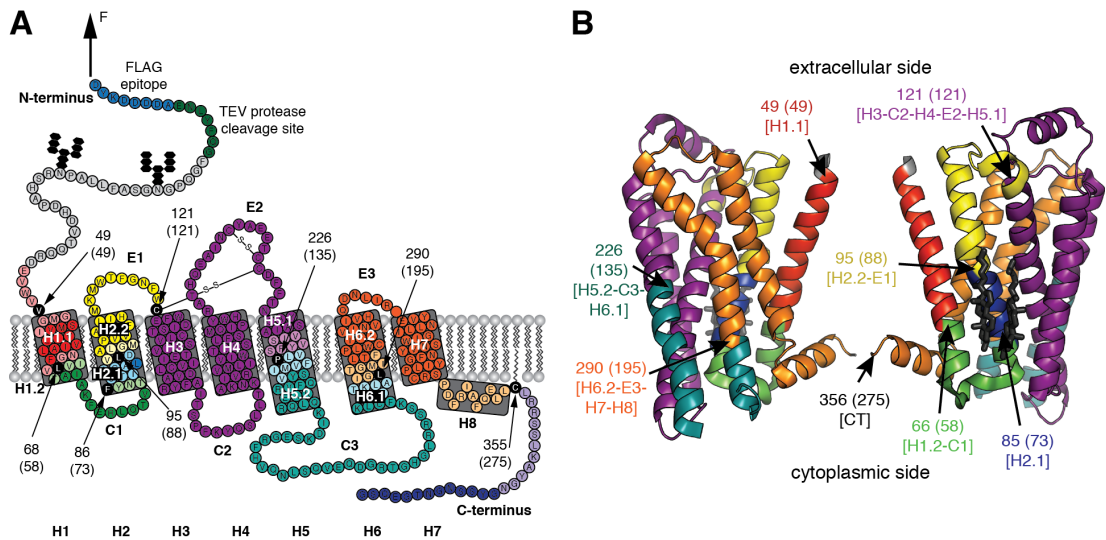


**Figure 3.8: Structural segments stabilizing human  $\beta_2$ AR.** Secondary (**A**) and tertiary (**B**) structure model of  $\beta_2$ AR. Each color represents a structural segment that is stabilized by inter- and intramolecular interactions. (**A**) Black amino acids (aa) highlight the end of the previous and the beginning of the next stable structural segment. This structural position corresponds to the mean contour length (given in brackets) revealed from WLC curves fitting every force peak of every F-D curve. aa colored at less intensity give the standard deviation of locating the average force peak (**Table 3.1**). Membrane compensation' (see section 3.2.5) was applied for the boundaries of structural segments that had to be assumed to lie within the membrane or at the membrane surface opposite to the pulling AFM stylus. All seven transmembrane  $\alpha$ -helices of  $\beta_2$ AR are labeled with bold numerals (H1-H7). Cytoplasmic and extracellular loops are indicated C1, C2, C3 and E1, E2, E3, respectively. H8 denotes the short C-terminal  $\alpha$ -helix 8 at the cytoplasmic side. The secondary structure model (**A**) of C-terminally truncated  $\beta_2$ AR carrying a N-terminal FLAG epitope (blue) followed by a TEV protease cleavage site (green) was taken from (66). The tertiary structure model (**B**) was taken from PDB ID 3D4S.

### 3.3.1.4 Cholesterol changes the energy landscape of $\beta_2$ AR

The most probable force required to unfold a structural segment of a protein depends on the loading rate (pulling force applied *versus* time) (165). Thus, the unfolding force is only a relative measure of the stability of a structural segment exposed to mechanical stress. However, the kinetic, energetic, and mechanical properties of a folded structure that resides in an energy valley at equilibrium can be described by a free energy unfolding landscape (**Figure 2.3**). To approximate these parameters (165, 231) F-D curves were recorded at seven different pulling

velocities (100, 300, 600, 900, 1200, 2500 and 5000 nm/s). To investigate the effect of cholesterol on the energy landscape of  $\beta_2$ AR, DFS was carried out in the absence and in the presence of cholesterol. Then the most probable unfolding force  $F^*$  of every structural segment was determined at different loading rates  $r_f^*$ . After this, the most probable unfolding force was plotted *versus* the most probable loading rate for every structural segment in a so-called DFS plot (**Figure 3.9**). As theoretically predicted (171, 177) and experimentally verified using membrane proteins (129, 130, 135, 232-234), increasing the loading rate increased the unfolding forces. A linear relationship between the most probable unfolding force and the logarithm of the loading rate was observed for every interaction. This linearity suggests that, for every structural segment, a single energy barrier separated the folded from the unfolded state (**Figure 2.3**) (171). The DFS data were fitted using **Equation 2.8** (**Figure 3.9**) to reveal the ground-to-transition-state distance  $x_u$  and transition rate  $k_0$ , and **Equation 2.9** and **Equation 3.1** were used to estimate the unfolding free energy  $\Delta G_0^\ddagger$  and the mechanical spring constant  $\kappa$  for every structural segment of  $\beta_2$ AR (see section 2.8.3). The statistical significance of these differences was estimated using a non-linear sum-of-squares  $F$ -test (**Table 3.2**) (235, 236). Several segments showed statistical significant differences in the presence of cholesterol (**Table 3.3**) suggesting that the energy barriers stabilizing the individual structural regions of  $\beta_2$ AR changed. In the following these cholesterol-induced changes will be described.

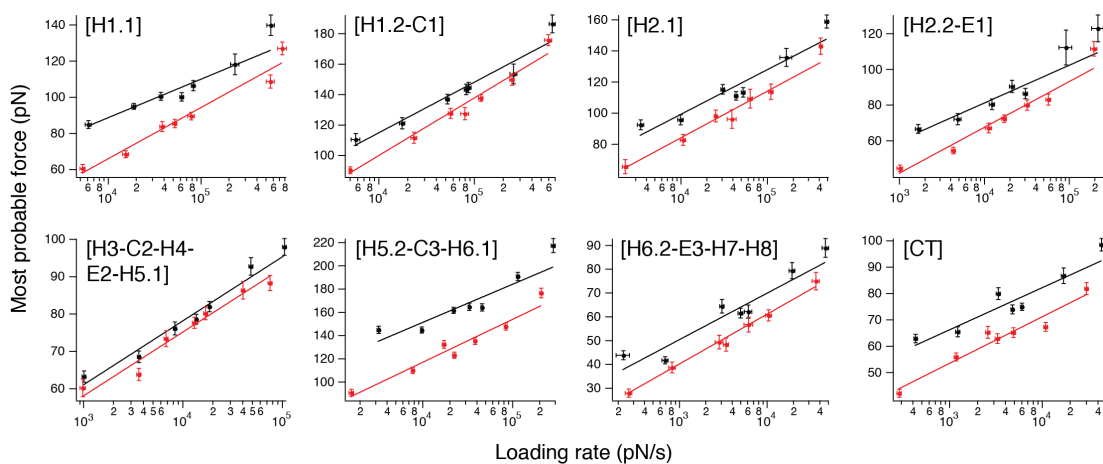


**Figure 3.9: Loading rate dependent interactions stabilizing structural segments of  $\beta_2$ AR depend on cholesterol.** DFS plots of each structural segment of  $\beta_2$ AR reconstituted into DOPC (red) and DOPC/CHS liposomes (black). Shown is the most probable unfolding force against the most probable loading rate. Solid lines show DFS fits from which  $x_u$  and  $k_0$  were obtained (**Table 3.3**). Error bars indicate the standard error of the most probable force and the loading rate.

**Table 3.2: Sum of squares  $F$ -test comparing DFS data recorded from  $\beta_2AR$  reconstituted into DOPC and DOPC/CHS liposomes.** For every stable structural segment the DFS data points (**Figure 3.9**) were fitted individually and simultaneously using **Equation 2.8**. The difference between the individually and simultaneously fitted values was assessed by sum-of-square (SSQ)  $F$ -tests. Degrees of freedom (dof) are given in parentheses. The  $F$ -ratio given by  $F=((SSQ1-SSQ2)/(dof1-dof2))/(SSQ2/dof2)$  quantifies the relationship between the relative increase in the sum of squares and the relative increase in the degrees of freedom. SSQ1 and SSQ2 refer to the sum of the two compared fits; dof1 and dof2 denote the degrees of freedom of the two compared fits.  $p$ -values estimate the significance of differences of the same stable structural segment detected in  $\beta_2AR$  in DOPC/CHS and DOPC.

<b>Lipid</b>	<b>Stable structural segment</b>	<b>Separate SSQ1 (dof1) SSQ2 (dof2)</b>	<b>Common SSQ (dof)</b>	<b><math>F</math>-ratio</b>	<b><math>p</math>-value</b>
DOPC/CHS DOPC	[H1]	154.1 (5) 128.9 (5)	1477.8 (12)	21.110	$1.202 \cdot 10^{-4}$
DOPC/CHS DOPC	[H1.2-C1]	214.0 (5) 130.6 (5)	860.8 (12)	7.490	$6.464 \cdot 10^{-3}$
DOPC/CHS DOPC	[H2.1]	253.7 (5) 117.0 (5)	1083.1 (12)	9.609	$2.718 \cdot 10^{-3}$
DOPC/CHS DOPC	[H2.2-E1]	164.5 (5) 134.0 (5)	1016.7 (12)	12.028	$1.179 \cdot 10^{-3}$
DOPC/CHS DOPC	[H3-C2-H4-E2-H5.1]	24.0 (5) 55.2 (5)	89.6 (12)	0.657	0.597
DOPC/CHS DOPC	[H5.2-C3-H6.1]	497.7 (5) 237.6 (5)	4581.7 (12)	26.153	$4.756 \cdot 10^{-5}$
DOPC/CHS DOPC	[H6.2-E3-H7-H8]	138.9 (5) 13.2 (5)	596.4 (12)	14.606	$5.512 \cdot 10^{-4}$
DOPC/CHS DOPC	[CT]	90.6 (5) 49.4 (5)	659.3 (12)	18.546	$2.076 \cdot 10^{-4}$

**Table 3.3: Parameters characterizing the free energy barrier ( $x_u$ ,  $k_0$  and  $\Delta G_0^\ddagger$ ) and spring constant ( $\kappa$ ) of structural segments stabilizing  $\beta_2AR$  reconstituted into DOPC and DOPC/CHS liposomes.** Errors represent standard deviations (SD). Differences were considered significant when  $p$ -values approached  $p < 0.001$  from  $F$ -tests (**Table 3.2**) and their changes did not overlap with their standard deviation. Significant changes are highlighted bold.

Stable structural segment	$x_u \pm SD$ (nm)		$k_0 \pm SD$ ( $s^{-1}$ )	
	DOPC	DOPC/CHS	DOPC	DOPC/CHS
[H1.1]	0.33 $\pm$ 0.02	<b>0.44 <math>\pm</math> 0.04</b>	3.935 $\pm$ 1.210	<b>0.077 <math>\pm</math> 0.073</b>
[H1.2-C1]	0.26 $\pm$ 0.02	0.29 $\pm$ 0.02	1.418 $\pm$ 0.429	<b>0.248 <math>\pm</math> 0.178</b>
[H2.1]	0.32 $\pm$ 0.02	0.33 $\pm$ 0.02	1.250 $\pm$ 0.496	<b>0.290 <math>\pm</math> 0.174</b>
[H2.2-E1]	0.37 $\pm$ 0.02	<b>0.45 <math>\pm</math> 0.05</b>	2.174 $\pm$ 0.592	<b>0.166 <math>\pm</math> 0.140</b>
[H3-C2-H4-E2-H5.1]	0.55 $\pm$ 0.04	0.55 $\pm$ 0.03	0.055 $\pm$ 0.041	0.038 $\pm$ 0.022
[H5.2-C3-H6.1]	0.26 $\pm$ 0.01	0.29 $\pm$ 0.02	0.443 $\pm$ 0.162	<b>0.018 <math>\pm</math> 0.014</b>
[H6.2-E3-H7-H8]	0.45 $\pm$ 0.03	0.49 $\pm$ 0.03	1.376 $\pm$ 0.384	<b>0.320 <math>\pm</math> 0.118</b>
[CT]	0.54 $\pm$ 0.03	0.59 $\pm$ 0.05	0.126 $\pm$ 0.054	<b>0.011 <math>\pm</math> 0.008</b>

Stable structural segment	$\Delta G_0^\ddagger \pm SD$ ( $k_B T$ )		$\kappa \pm SD$ (N/m)	
	DOPC	DOPC/CHS	DOPC	DOPC/CHS
[H1.1]	17.1 $\pm$ 0.3	<b>21.0 <math>\pm</math> 0.9</b>	1.26 $\pm$ 0.11	<b>0.88 <math>\pm</math> 0.13</b>
[H1.2-C1]	18.1 $\pm$ 0.3	<b>19.8 <math>\pm</math> 0.7</b>	2.39 $\pm$ 0.17	2.02 $\pm$ 0.26
[H2.1]	18.2 $\pm$ 0.4	<b>19.7 <math>\pm</math> 0.6</b>	1.51 $\pm$ 0.17	1.49 $\pm$ 0.18
[H2.2-E1]	17.6 $\pm$ 0.3	<b>20.2 <math>\pm</math> 0.8</b>	1.07 $\pm$ 0.10	0.84 $\pm$ 0.15
[H3-C2-H4-E2-H5.1]	21.3 $\pm$ 0.7	21.7 $\pm$ 0.6	0.58 $\pm$ 0.07	0.59 $\pm$ 0.06
[H5.2-C3-H6.1]	19.2 $\pm$ 0.4	<b>22.4 <math>\pm</math> 0.8</b>	2.43 $\pm$ 0.21	2.23 $\pm$ 0.25
[H6.2-E3-H7-H8]	18.1 $\pm$ 0.3	<b>19.6 <math>\pm</math> 0.4</b>	0.73 $\pm$ 0.08	0.69 $\pm$ 0.08
[CT]	20.5 $\pm$ 0.4	<b>23.0 <math>\pm</math> 0.7</b>	0.59 $\pm$ 0.06	0.54 $\pm$ 0.06

### 3.3.1.5 Cholesterol increases kinetic and energetic stability of $\beta_2AR$

Most prominent among the changes induced by cholesterol is that almost every structural segment of  $\beta_2AR$  increased kinetic and energetic stability (**Table 3.3**). The free energy barriers that stabilize each structural segment against unfolding increased height in the presence of cholesterol. Particular the energy barriers stabilizing the structural segments [H1.1], [H1.2-C1], [H2.1], [H2.2-E1], [H5.2-C3-H6.1], [H6.2-E3-

H7-H8] and [CT] were significantly higher in the presence of cholesterol. For individual structural segments the free energy increase caused by cholesterol ranged between  $1.5 k_B T$  ([H2.1] and [H6.2-E3-H7-H8]) and  $3.9 k_B T$  ([H1.1]). The exception was the largest structural segment [H3-C2-H4-E2-H5.1], whose small increase of the energy barrier ( $0.4 k_B T$ ) was not significant. Synchronous to the free energy barrier heights, the structural segments significantly increased kinetic stability (reciprocal of the transition rate  $k_0$ ) in the presence of cholesterol (**Table 3.3**). Some structural segments increased their kinetic stability considerably. For example in the presence of cholesterol structural segment [H1.1] increased kinetic stability by a factor of 50, [H1.2-C1] by a factor of 6, [H2.1] and [H6.2-E3-H7-H8] by a factor of 4, [H5.2-C3-H6.1] by a factor of 25, and [CT] by a factor of 11. However, the transition rate of the structural core segment [H3-C2-H4-E2-H5.1] remained unchanged in the presence of cholesterol.

### **3.3.1.6 Cholesterol increases conformational variability and decreases mechanical rigidity of transmembrane $\alpha$ -helices H1 and H2**

The conformational variability of a structure can be approximated by the ground-to-transition state distance  $x_u$  (237, 238). With increasing ground-to-transition state distance the energy valley stabilizing a structural segment becomes wider. Consequently, the segment can adopt more conformational substates and, therefore, enhances conformational variability. On the contrary, if an energy valley stabilizing a structural segment narrows the conformational variability of the structural segment decreases (**Figure 2.3**). The only structural segments that significantly increased transition state distance  $x_u$  by  $\approx 20$ -30% and, thus, increased conformational variability were [H1.1] and [H2.2-E1] (**Table 3.3**). Although the other structural segments of  $\beta_2$ AR showed similar trends in presence of cholesterol these differences were insignificant.

The spring constant  $\kappa$  quantifies the mechanical rigidity of a structural segment (135, 230). Although all structural segments (except

[H3-C2-H4-E2-H5.1]) slightly decreased their mechanical rigidity (spring constant) in the presence of cholesterol (**Table 3.3**), this decrease was only statistically significant for structural segment [H1.1], which decreased the spring constant by  $\approx 30\%$  to 0.88 N/m.

### **3.3.2 Discussion**

#### **3.3.2.1 Cholesterol strengthens interactions of almost every structural segment of $\beta_2$ AR**

Using SMFS, interactions that stabilize the human  $\beta_2$ AR reconstituted into DOPC liposomes were characterized. F-D spectra recorded during mechanical unfolding of  $\beta_2$ AR showed a reproducible pattern of force peaks (**Figure 3.4B,C**). This pattern suggests that a characteristic interaction network stabilized structural segments within  $\beta_2$ AR. The presence of cholesterol did not alter the position of the force peaks. Thus, it can be concluded that the interactions established in the presence of cholesterol stabilized the same structural segments of  $\beta_2$ AR as detected in the absence of cholesterol. However, cholesterol increased the magnitude of individual force peaks (**Figure 3.5**) and, thus, increased the interaction strengths stabilizing the structural segments within  $\beta_2$ AR (**Figure 3.9**). As this trend was observed for all structural segments (except for [H3-C2-H4-E2-H5.1]) and for all pulling velocities it can be concluded that cholesterol increased the mechanical stability of  $\beta_2$ AR. This increased mechanical stability may result from direct interactions between cholesterol and  $\beta_2$ AR. However, since cholesterol also affects the properties of the lipid membrane (14, 239, 240) and because cholesterol establishes direct interactions with some but not with all structural segments of  $\beta_2$ AR (217), it can be assumed that it also affected the stability of  $\beta_2$ AR indirectly.

### **3.3.2.2 Cholesterol increases free energy barrier and kinetic stability of every structural segment except for the structural core segment**

The strengths of the interactions stabilizing the structural segments of  $\beta_2$ AR depended on the loading rate (**Figure 3.9**). This dependency was used to characterize the energy valley and barrier stabilizing every structural segment (**Table 3.3**). Except for the structural core segment [H3-C2-H4-E2-H5.1], cholesterol significantly affected the energy landscape of every structural segment of  $\beta_2$ AR. Generally, the free energy barriers stabilizing these structural segments increased height in the presence of cholesterol. Consequently, the structural segments reduced transition rate and increased kinetic stability. Thus, cholesterol increased the kinetic and energetic stability of  $\beta_2$ AR. However, the energy landscape of individual structural segments stabilizing  $\beta_2$ AR and thus their properties changed quite individually. These changes, which are structurally mapped in **Figure 3.10**, will be discussed in the following.

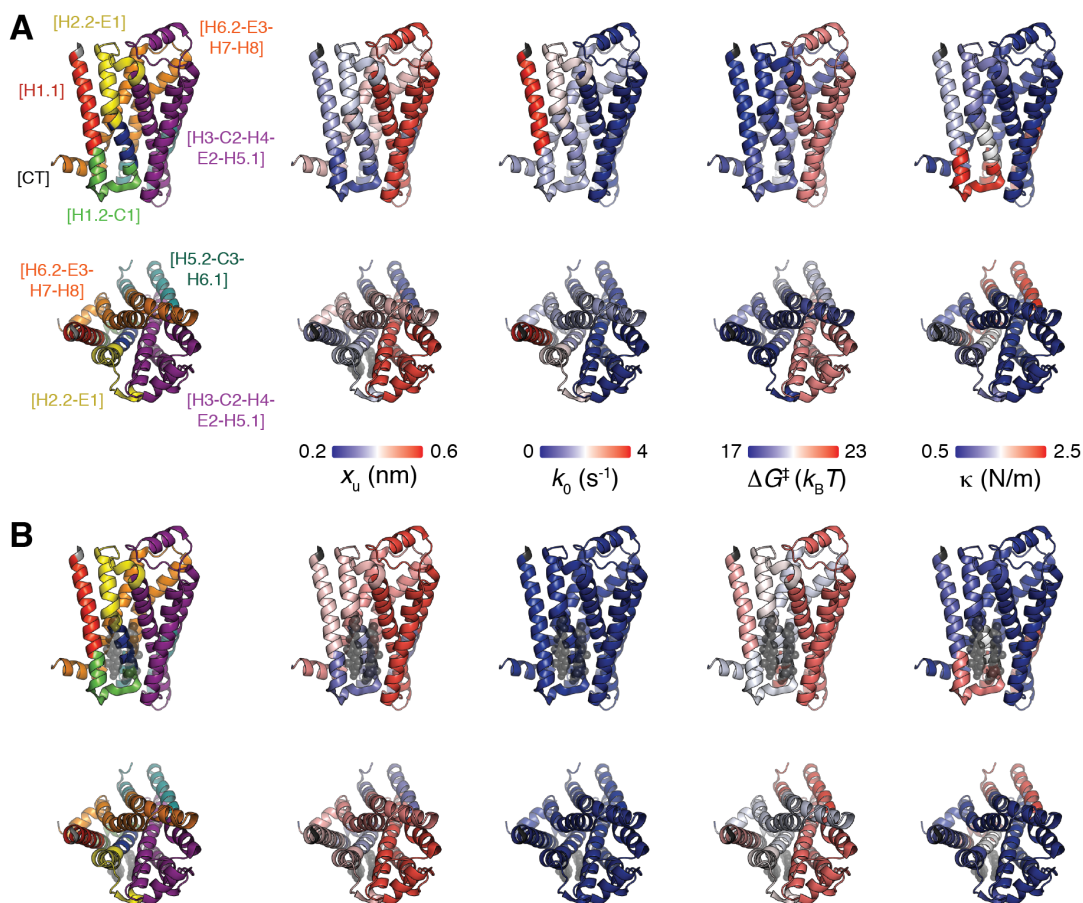


**Figure 3.10: Mapping the kinetic, energetic, and mechanical properties of  $\beta_2$ AR in the absence (A) and presence (B) of cholesterol.** Structural segments stabilizing  $\beta_2$ AR (PDB ID code 3D4S) are mapped on the left. Transition state distance  $x_u$ , transition rate  $k_0$ , free energy barrier height  $\Delta G_0^\ddagger$ , and spring constant  $\kappa$  of structural segments in the absence of cholesterol (A) and in the presence of cholesterol (B). The color of the  $\beta_2$ AR backbone roughly indicates the value for each parameter as indicated by the scale bars. Top panel of (A) and (B) shows  $\beta_2$ AR from side view, lower panel of (A) and (B) shows  $\beta_2$ AR from extracellular view. Values were taken from **Table 3.3**.

### 3.3.2.3 [H1.1]

The presence of cholesterol affected kinetic, energetic, and mechanical parameters of structural segment [H1.1]. Cholesterol increased the transition state distance  $x_u$  by 33% to 0.44 nm, which enhanced the conformational variability of the extracellular region of transmembrane  $\alpha$ -helix H1. Furthermore, cholesterol significantly decreased the transition rate  $k_0$  and thus, increased the kinetic stability of [H1.1] 50-fold. Moreover, cholesterol increased the free energy barrier,

$\Delta G_0^\ddagger$ , stabilizing [H1.1] by  $\approx 4 k_B T$  ( $\approx 23\%$ ). Finally, [H1.1] was the only structural segment of  $\beta_2$ AR, which significantly lowered the spring constant  $\kappa$  in presence of cholesterol from 1.26 N/m to 0.88 N/m ( $\approx 30\%$ ). This implies that cholesterol increases mechanical flexibility of this structural region. The X-ray structure suggests that H1 establishes a direct interaction with cholesterol (217). The DFS data shows that cholesterol kinetically and energetically stabilizes the extracellular part of  $\alpha$ -helix H1 and enhances its mechanical flexibility. It is thought that GPCRs including  $\beta_2$ AR can assemble into dimers in the plasma membrane (200, 241). Although the functional importance of this dimerization and the exact location of the dimer interface in GPCRs are not fully understood (242) it may be speculated that cholesterol promotes  $\beta_2$ AR dimerization, since ordered cholesterol molecules were found in the interface between H1 and H8 of two symmetry-related  $\beta_2$ AR molecules (65). It has been proposed for several other class A GPCRs that  $\alpha$ -helix H1 is involved in receptor oligomerization (243, 244). Therefore, it may be speculated that increased kinetic and energetic stability, and mechanical flexibility of [H1.1] may favor oligomerization of  $\beta_2$ AR.

#### **3.3.2.4 [H1.2-C1]**

In the presence of cholesterol the energy landscape stabilizing structural segment [H1.2-C1] showed minor but statistically significant changes. [H1.2-C1] decreased transition rate and, thus, increased kinetic stability 6-fold. The free energy of [H1.2-C1] increased by  $1.7 k_B T$  ( $\approx 9\%$ ), indicating that this structural segment stabilizes in the presence of cholesterol. Structural models show cholesterol binding to the C-terminal part of transmembrane  $\alpha$ -helix H1 (217), which could directly change the properties of structural segments [H1.1] and [H1.2-C1] as detected by DFS. Further changes may be caused by direct interactions between cholesterol and residue Y70 at the interface between structural segments [H1.2-C1] and [H2.1]. The minor changes detected for [H1.2-C1] correlates with the finding that Y70 appears to be the least important residue for cholesterol binding and establishes only van-der-Waals-

interactions with ring A of cholesterol (217). In absence of further information, it may be speculated that electrostatic interactions between hydrophilic residues of intracellular loop C1 (e.g. K60, R63) and the cholesterol hydroxyl group could also contribute to the cholesterol-induced changes of [H1.2-C1].

### 3.3.2.5 [H2.1]

Cholesterol reduced the transition rate  $k_0$  of [H2.1] 6-fold and increased the height of the free energy barrier  $\Delta G_0^\ddagger$  by  $1.5 k_B T$  ( $\approx 8\%$ ). The ground-to-transition state distance  $x_u$  and the spring constant  $\kappa$  of [H2.1] remained unchanged. Thus, in the presence of cholesterol, the lifetime and the energetic stability of [H2.1] enhanced significantly. These changes may result from direct interactions between  $\beta_2AR$  and cholesterol, which interacts with [H2.1] *via* residues T73, S74 and C77 (217). Hanson *et al.* (217) showed that cholesterol increases the packing value for transmembrane  $\alpha$ -helix H2, which correlates with an increased thermal stability of  $\beta_2AR$ . The DFS data shows that the increased packing value induced by cholesterol increases the kinetic and energetic stability of  $\alpha$ -helix H2.

### 3.3.2.6 [H2.2-E1]

Cholesterol slightly increased the ground-to-transition state distance by 0.08 nm and, thus, the conformational variability of [H2.2-E1]. Furthermore, cholesterol increased the kinetic stability of this structural segment 13-fold, and increased the height of the free energy barrier by  $2.6 k_B T$  ( $\approx 15\%$ ). Cholesterol increases the packing value of  $\alpha$ -helix H2 and interacts with [H2.2-E1] through an interaction with V81 (217). The changes in [H2.2-E1] might also be indirectly induced by electrostatic interactions between the cholesterol hydroxyl group and positively charged residues (e.g. K97) of extracellular loop E1.

### 3.3.2.7 [H3-C2-H4-E2-H5.1]

Although transmembrane  $\alpha$ -helices H3 and H4 are supposed to establish direct interactions with cholesterol (217), the energy landscape

of the core segment remained unchanged by the presence of cholesterol. This finding was surprising because it was recently detected that [H3-C2-H4-E2-H5.1] changes energy landscape in the presence of agonists and inverse agonists (245). However, the core segment [H3-C2-H4-E2-H5.1] exposed a relatively high conformational variability (high  $x_u$ ) and high mechanical elasticity (low  $\kappa$ ) compared to the other structural segments of  $\beta_2$ AR in the presence of cholesterol. Thermal stability assays showed that cholesterol increased the packing value, and thus, the thermal stability of transmembrane  $\alpha$ -helix H4 (217), which is part of the core segment. Furthermore, the crystal structures of cholesterol bound  $\beta_2$ AR were determined from solubilized and liganded receptors (217). In contrast to these measurements, we characterized unliganded  $\beta_2$ AR reconstituted into liposomes. It may be speculated that the different experimental conditions cause this apparent discrepancy. However, the short  $\alpha$ -helical region of loop E2 contains two disulfide bonds that link transmembrane  $\alpha$ -helices H3, H4 and H5 (65) and stabilize the core segment of  $\beta_2$ AR. In addition, the structural core segment contains multiple ligand binding sites (188, 189). It has been also shown that cholesterol is required for efficient ligand binding of  $\beta_2$ AR (246). Thus, the finding that the core segment of  $\beta_2$ AR retains its relatively high conformational variability and mechanical flexibility in the presence of cholesterol may be of functional importance for ligand binding.

### **3.3.2.8 [H5.2-C3-H6.1]**

Cholesterol significantly increased the kinetic stability of [H5.2-C3-H6.1] 25-fold and increased the height of the energy barrier,  $\Delta G_0^\ddagger$ , by 3.2  $k_B T$  ( $\approx 17\%$ ). The distance between ground and transition state as well as the spring constant of [H5.2-C3-H6.1] remained unchanged. These changes are surprising, since cholesterol does not directly interact with structural segment [H5.2-C3-H6.1]. Thus, it can be assumed that cholesterol induced these changes by modulating the biophysical properties of the lipid membrane (14, 239, 240) or/and by indirect interactions in  $\beta_2$ AR. As assessed by proteolysis and split receptor

studies, co-transfection of a plasmid encoding the N-terminus to  $\alpha$ -helix H5 and a plasmid encoding  $\alpha$ -helix H6 to the C-terminus generates a functional ‘split’ receptor (247). The interface between both fragments locates at segment [H5.2-C3-H6.1]. Furthermore, the N- and C-terminal regions of cytoplasmic loop C3 are involved in G protein activation and are crucial for the formation of interactions between GPCR and G protein (248). These GPCR and G protein interactions require cholesterol (249). Thus, it may be speculated that the kinetic and energetic stability of [H5.2-C3-H6.1] increased by cholesterol may play a role in regulating the interactions between  $\beta_2$ AR and G proteins.

### **3.3.2.9 [H6.2-E3-H7-H8]**

In the presence of cholesterol, structural segment [H6.2-E3-H7-H8] significantly increased the kinetic stability  $k_0$  4-fold and increased the free energy barrier,  $\Delta G_0^\ddagger$ , by  $1.5 k_B T$  ( $\approx 8\%$ ). The oligomerization of class A GPCRs involves the interface between  $\alpha$ -helices H1 and H8 (243, 244). Similar to segments [H1.1] and [H1.2-C1] it may be speculated that cholesterol affects oligomerization of  $\beta_2$ AR by modulating the kinetic and the energetic stability of [H6.2-E3-H7-H8]. Furthermore,  $\alpha$ -helix H8, which lies parallel to the membrane, might be affected by the composition of the membrane, for example through electrostatic interactions with polar lipid headgroups or the hydroxyl group of cholesterol (217).

### **3.3.2.10 [CT]**

Cholesterol induced significant changes in [CT], which increased kinetic stability 10-fold and free energy by  $2.5 k_B T$  ( $\approx 12\%$ ). The C-terminal end of  $\beta_2$ AR is not known to contribute to cholesterol binding to the receptor (217). Thus, it might be speculated that the changing properties of segment [CT] could be indirectly caused by cholesterol modulating the biophysical properties of the lipid bilayer. However, [CT] contains charged amino acid residues, which might establish electrostatic interactions with the interfacial region of the membrane, to which the cholesterol hydroxyl group contributes. [CT] is functionally important since it interacts with G protein-coupled receptor kinases, arrestin and

further signaling molecules (250). For instance, the C-terminal binding domain is required to direct the trafficking of  $\beta_2$ AR to cholesterol-rich caveolae (251). Therefore, it can be assumed that the properties of [CT] changed by cholesterol in turn influence the way signaling molecules interact with  $\beta_2$ AR.

### **3.4 Ligand-specific changes of the $\beta_2$ AR**

#### **3.4.1 Results**

##### **3.4.1.1 Determining energetic, kinetic and mechanical properties of structural segments of $\beta_2$ AR in the presence of ligands**

To investigate to which extent the binding of different ligands affects the energy landscape of  $\beta_2$ AR (reconstituted into DOPC/CHS proteoliposomes), DFS was carried out in the unbound state and in the presence of the synthetic agonists BI-167107 (BI, Boehringer-Ingelheim) and THRX-144877 (THRX, Theravance), the natural agonist adrenalin, the inverse agonist carazolol and the neutral antagonist alprenolol. For all pulling velocities superimpositions of the F-D curves did not change drastically upon ligand binding to  $\beta_2$ AR. Next, the most probable unfolding force  $F^*$  of every force peak characterizing a stable structural segment of  $\beta_2$ AR was determined and plotted for the different loading rates  $r_f^*$  (**Figure 3.11**).

##### **3.4.1.2 Ligands change energy landscape of $\beta_2$ AR**

Fitting the DFS plots using **Equation 2.8** (**Figure 3.11**) revealed the transition state  $x_u$ , transition rate  $k_0$ , free energy  $\Delta G_0^\ddagger$ , and mechanical spring constant  $\kappa$  characterizing every structural segment (**Figure 3.8**). Differences between these parameters imply that the kinetic stability and mechanical nature of molecular interactions changed in the presence of ligands (**Table 3.4**). To determine the statistical significance of these differences, DFS plots from ligand-free and ligand-bound  $\beta_2$ AR were fitted simultaneously, resulting in a common estimate for  $x_u$  and  $k_0$ . The sum of squares of both separate and simultaneous fits was assessed by an  $F$ -test (**Table 3.5**) (235, 236). Several segments

showed statistically significant differences after ligand binding (**Table 3.4**). In the following the significant differences detected in the experiments will be described.

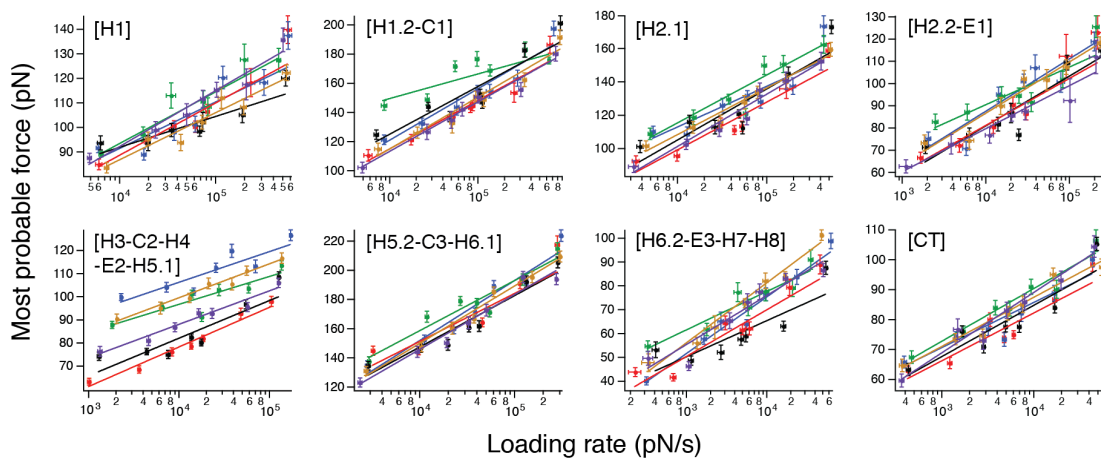


**Figure 3.11: DFS plots reveal loading rate dependent interactions stabilizing  $\beta_2AR$ .** For each stable structural segment of  $\beta_2AR$  the most probable unfolding force was plotted against the loading rate. DFS fits using **Equation 2.8** (see section 2.8.3) are shown for unliganded (red), alprenolol bound (black), carazolol bound (green), BI bound (blue), THRX bound (orange) and adrenalin bound (violet) states. Values for  $x_u$  and  $k_0$  obtained from fitting the DFS plots are given in **Table 3.4**. Error bars represent the standard error of most probable force and loading rate.

**Table 3.4: Parameters characterizing energy barriers ( $x_u$ ,  $k_0$ , and  $\Delta G_0^\ddagger$ ) and mechanical spring constants ( $k$ ) of structural segments stabilizing  $\beta_2$ AR.** Parameters are shown for unliganded  $\beta_2$ AR and in the presence of two high-affinity agonists (BI and THRX), a strong partial agonist (adrenalin), an inverse agonist (carazolol) and a neutral antagonist (alprenolol). Errors represent standard deviations (SD). Statistically significant changes to the unliganded state were assessed by *F*-tests (Table 3.5) and highlighted bold.

Stable structural segment	$x_u \pm \text{SD} (nm)$					
	Unliganded $\beta_2$ AR	Agonist (BI)	Agonist (THRX)	Agonist (adrenalin)	Inverse agonist (Carazolol)	Neutral antagonist (alprenolol)
[H1.1]	0.44 ± 0.04	0.50 ± 0.05	0.49 ± 0.07	0.47 ± 0.05	0.45 ± 0.04	<b>0.75 ± 0.12</b>
[H1.2-C1]	0.29 ± 0.02	0.27 ± 0.02	0.30 ± 0.04	0.26 ± 0.03	<b>0.56 ± 0.07</b>	0.29 ± 0.02
[H2.1]	0.33 ± 0.02	0.39 ± 0.04	0.39 ± 0.05	0.33 ± 0.04	0.33 ± 0.02	0.31 ± 0.02
[H2.2-E1]	0.45 ± 0.05	0.40 ± 0.04	0.40 ± 0.06	0.54 ± 0.08	0.56 ± 0.08	0.42 ± 0.03
[H3-C2-H4-E2-H5.1]	0.55 ± 0.03	<b>0.71 ± 0.07</b>	<b>0.73 ± 0.13</b>	<b>0.65 ± 0.09</b>	<b>0.79 ± 0.08</b>	0.58 ± 0.04
[H5.2-C3-H6.1]	0.29 ± 0.02	0.23 ± 0.01	0.25 ± 0.02	0.26 ± 0.02	0.28 ± 0.02	0.27 ± 0.02
[H6.2-E3-H7-H8]	0.49 ± 0.03	0.40 ± 0.02	0.39 ± 0.05	0.40 ± 0.04	<b>0.59 ± 0.06</b>	0.58 ± 0.05
[CT]	0.59 ± 0.05	0.63 ± 0.06	0.64 ± 0.10	0.49 ± 0.06	0.54 ± 0.05	0.55 ± 0.04

Stable structural segment	$k_0 \pm \text{SD} (10^{-3} s^{-1})$					
	Unliganded $\beta_2$ AR	Agonist (BI)	Agonist (THRX)	Agonist (adrenalin)	Inverse agonist (Carazolol)	Neutral antagonist (alprenolol)
[H1.1]	77.3 ± 72.5	18.7 ± 22.0	43.8 ± 64.7	26.6 ± 30.5	41.5 ± 33.9	<b>0.09 ± 0.26</b>
[H1.2-C1]	248 ± 178	253 ± 161	121 ± 147	473 ± 372	<b>0.002 ± 0.005</b>	111 ± 76.2
[H2.1]	290 ± 174	23.1 ± 27.1	30.5 ± 42.1	234 ± 210	<b>80.8 ± 54.8</b>	290 ± 179
[H2.2-E1]	166 ± 140	196 ± 144	211 ± 236	38.2 ± 55.2	6.61 ± 11.5	261 ± 155
[H3-C2-H4-E2-H5.1]	38.8 ± 22.4	<b>0.02 ± 0.03</b>	<b>0.04 ± 0.01</b>	<b>1.51 ± 2.75</b>	<b>0.02 ± 0.03</b>	13.4 ± 10.4
[H5.2-C3-H6.1]	18.0 ± 13.5	118 ± 53.3	58.3 ± 41.1	59.5 ± 41.4	16.7 ± 11.5	44.5 ± 24.8
[H6.2-E3-H7-H8]	320 ± 118	663 ± 184	480 ± 300	636 ± 329	<b>21.9 ± 20.7</b>	151 ± 106
[CT]	10.7 ± 7.98	3.28 ± 3.21	2.55 ± 4.06	33.0 ± 31.2	9.99 ± 8.90	15.4 ± 10.8

Stable structural segment	$\Delta G_0^{\pm} \pm SD (k_B T)$					
	Unliganded $\beta_2$ AR	Agonist (BI)	Agonist (THRX)	Agonist (adrenalin)	Inverse agonist (Carazolol)	Neutral antagonist (Alprenolol)
[H1.1]	21.0 $\pm$ 0.9	22.4 $\pm$ 1.2	21.5 $\pm$ 1.5	22.0 $\pm$ 1.1	21.6 $\pm$ 0.8	<b>27.7 <math>\pm</math> 2.7</b>
[H1.2-C1]	19.8 $\pm$ 0.7	19.8 $\pm$ 0.6	20.5 $\pm$ 1.2	19.2 $\pm$ 0.8	<b>31.5 <math>\pm</math> 2.5</b>	20.6 $\pm$ 0.7
[H2.1]	19.7 $\pm$ 0.6	22.2 $\pm$ 1.2	21.9 $\pm$ 1.4	19.9 $\pm$ 0.9	<b>20.9 <math>\pm</math> 0.7</b>	19.7 $\pm$ 0.6
[H2.2-E1]	20.2 $\pm$ 0.8	20.1 $\pm$ 0.7	20.0 $\pm$ 1.1	21.7 $\pm$ 1.4	23.4 $\pm$ 1.7	19.8 $\pm$ 0.6
[H3-C2-H4-E2-H5.1]	21.7 $\pm$ 0.6	<b>29.4 <math>\pm</math> 1.7</b>	<b>28.6 <math>\pm</math> 2.9</b>	<b>24.9 <math>\pm</math> 1.8</b>	<b>29.3 <math>\pm</math> 1.7</b>	22.7 $\pm$ 0.8
[H5.2-C3-H6.1]	22.4 $\pm$ 0.8	20.6 $\pm$ 0.5	21.3 $\pm$ 0.7	21.2 $\pm$ 0.7	22.5 $\pm$ 0.7	21.5 $\pm$ 0.6
[H6.2-E3-H7-H8]	19.6 $\pm$ 0.4	18.8 $\pm$ 0.3	19.2 $\pm$ 0.6	18.9 $\pm$ 0.5	<b>22.2 <math>\pm</math> 0.9</b>	20.3 $\pm$ 0.7
[CT]	23.0 $\pm$ 0.7	24.1 $\pm$ 1.0	24.4 $\pm$ 1.6	21.8 $\pm$ 0.9	23.0 $\pm$ 0.9	22.6 $\pm$ 0.7

Stable structural segment	$\kappa \pm SD (N/m)$					
	Unliganded $\beta_2$ AR	Agonist (BI)	Agonist (THRX)	Agonist (adrenalin)	Inverse agonist (Carazolol)	Neutral antagonist (Alprenolol)
[H1.1]	0.88 $\pm$ 0.13	0.74 $\pm$ 0.12	0.76 $\pm$ 0.17	0.83 $\pm$ 0.14	0.88 $\pm$ 0.12	<b>0.40 <math>\pm</math> 0.09</b>
[H1.2-C1]	2.02 $\pm$ 0.26	2.28 $\pm$ 0.26	1.84 $\pm$ 0.39	2.30 $\pm$ 0.40	<b>0.83 <math>\pm</math> 0.13</b>	2.04 $\pm$ 0.22
[H2.1]	1.49 $\pm$ 0.18	1.22 $\pm$ 0.20	1.19 $\pm$ 0.25	1.50 $\pm$ 0.27	<b>1.60 <math>\pm</math> 0.16</b>	1.71 $\pm$ 0.20
[H2.2-E1]	0.84 $\pm$ 0.15	1.03 $\pm$ 0.15	1.04 $\pm$ 0.25	0.61 $\pm$ 0.15	0.62 $\pm$ 0.14	0.92 $\pm$ 0.10
[H3-C2-H4-E2-H5.1]	0.59 $\pm$ 0.06	<b>0.48 <math>\pm</math> 0.06</b>	<b>0.44 <math>\pm</math> 0.11</b>	<b>0.49 <math>\pm</math> 0.11</b>	<b>0.39 <math>\pm</math> 0.05</b>	0.56 $\pm$ 0.06
[H5.2-C3-H6.1]	2.23 $\pm$ 0.25	3.21 $\pm$ 0.26	2.71 $\pm$ 0.34	2.53 $\pm$ 0.33	2.45 $\pm$ 0.24	2.47 $\pm$ 0.22
[H6.2-E3-H7-H8]	0.69 $\pm$ 0.08	0.98 $\pm$ 0.09	1.03 $\pm$ 0.20	0.99 $\pm$ 0.19	<b>0.53 <math>\pm</math> 0.09</b>	0.50 $\pm$ 0.08
[CT]	0.54 $\pm$ 0.06	0.51 $\pm$ 0.07	0.49 $\pm$ 0.11	0.75 $\pm$ 0.14	0.66 $\pm$ 0.09	0.61 $\pm$ 0.07

**Table 3.5 (next page): Statistical analysis of DFS data.** Sum of squares  $F$ -test for DFS data of unliganded  $\beta_2AR$  compared to  $\beta_2AR$  bound to BI, THRX, adrenalin, carazolol and alprenolol. Degrees of freedom (dof) are given in parentheses. SMFS data were fitted individually and simultaneously (unliganded and liganded). The difference in the fits that were analyzed separately or simultaneously was assessed by  $F$ -tests. The  $F$ -ratio given by  $F = ((SSQ1 - SSQ2) / (dof1 - dof2)) / (SSQ2 / dof2)$  quantifies the relationship between the relative increase in the sum of squares and the relative increase in the degrees of freedom. SSQ1 and SSQ2 refer to the sum of the two compared fits; dof1 and dof2 denote the degrees of freedom of the two compared fits.  $p$ -values estimate the significance to the unliganded state.

Structural segment	Ligand	Sum of squares (dof)		F-ratio	p-value
		Separate	Common		
[H1]	<b>Unliganded</b>	<b>154.1 (5)</b>	-	-	-
	BI	277.8 (5)	441 (12)	0.105	0.955
	THRX	68.9 (5)	261.1 (12)	0.854	0.496
	Adrenalin	62.1 (5)	263.6 (12)	1.096	0.395
	Carazolol	131 (5)	378.1 (12)	1.631	0.244
	Alprenolol	86.7 (5)	522.5 (12)	5.849	0.014
[H1.2-C1]	<b>Unliganded</b>	<b>214 (5)</b>	-	-	-
	BI	250 (5)	623.5 (12)	1.719	0.226
	THRX	196.8 (5)	423.6 (12)	0.156	0.924
	Adrenalin	90 (5)	312.9 (12)	0.146	0.930
	Carazolol	314.2 (5)	2426.5 (12)	17.970	2.368•10 <sup>-4</sup>
	Alprenolol	523.4 (5)	1064.5 (12)	2.218	0.149
[H2.1]	<b>Unliganded</b>	<b>253.7 (5)</b>	-	-	-
	BI	524.9 (5)	1144.7 (12)	2.351	0.134
	THRX	57.5 (5)	411.2 (12)	1.607	0.249
	Adrenalin	119.5 (5)	394.1 (12)	0.280	0.839
	Carazolol	308.3 (5)	1232.5 (12)	5.965	0.013
	Alprenolol	624.3 (5)	1065.9 (12)	1.070	0.405
[H2.2-E1]	<b>Unliganded</b>	<b>164.5 (5)</b>	-	-	-
	BI	289.4 (5)	503.4 (12)	0.938	0.458
	THRX	101 (5)	322.9 (12)	1.081	0.401
	Adrenalin	111.8 (5)	376 (12)	1.805	0.210
	Carazolol	249.1 (5)	609.1 (12)	2.363	0.133
	Alprenolol	267.6 (5)	497.1 (12)	0.752	0.546
[H3-C2-H4-E2-H5.1]	<b>Unliganded</b>	<b>24 (5)</b>	-	-	-
	BI	116.6 (5)	2582.3 (12)	86.831	1.84•10 <sup>-7</sup>
	THRX	68.3 (5)	1443.7 (12)	73.207	4.163•10 <sup>-7</sup>
	Adrenalin	44.8 (5)	760.9 (12)	19.964	1.523•10 <sup>-4</sup>
	Carazolol	96.9 (5)	1128.6 (12)	41.675	5.842•10 <sup>-6</sup>
	Alprenolol	177.8 (5)	262.6 (12)	1.506	0.272
[H5.2-C3-H6.1]	<b>Unliganded</b>	<b>497.7 (5)</b>	-	-	-
	BI	278.4 (5)	832.3 (12)	0.362	0.782
	THRX	86.3 (5)	588.6 (12)	0.039	0.989
	Adrenalin	148.2 (5)	339.7 (12)	0.890	0.479
	Carazolol	295.7 (5)	927.6 (12)	0.846	0.500
	Alprenolol	263.9 (5)	861.9 (12)	0.658	0.596
[H6.2-E3-H7-H8]	<b>Unliganded</b>	<b>138.9 (5)</b>	-	-	-
	BI	58.9 (5)	260.4 (12)	1.582	0.255
	THRX	89.5 (5)	289.5 (12)	1.338	0.317
	Adrenalin	146.2 (5)	289.5 (12)	0.958	0.450
	Carazolol	87.6 (5)	451.9 (12)	4.976	0.023
	Alprenolol	266.4 (5)	499 (12)	1.156	0.374
[CT]	<b>Unliganded</b>	<b>90.6 (5)</b>	-	-	-
	BI	84.3 (5)	200.3 (12)	0.726	0.559
	THRX	66.14 (5)	183.2 (12)	0.844	0.500
	Adrenalin	72.4 (5)	218.8 (12)	1.712	0.227
	Carazolol	97.82 (5)	288.9 (12)	2.665	0.105
	Alprenolol	165.7 (5)	262.6 (12)	0.123	0.944

### **3.4.1.3 Structural segments changing conformational variability upon ligand binding**

The distance between ground state and transition state  $x_u$  approximates the conformational variability of a structure (**Figure 2.3**, see section 2.8.3) (237, 238). If a narrow energy valley stabilizing a structural segment becomes wider after binding of a ligand, the ligand increases the number of conformational states (i.e., conformational variability) the structural segment can adopt. Such an effect was observed upon ligand binding to  $\beta_2$ AR (**Table 3.4**). Binding of agonists (BI, THRX, or adrenalin) significantly increased the conformational variability of the core segment [H3-C2-H4-E2-H5.1] ( $p < 0.001$ ), carazolol significantly increased the conformational variability of structural segments [H1.2-C1] ( $p < 0.001$ ), [H3-C2-H4-E2-H5.1] ( $p < 0.001$ ), and [H6.2-E3-H7-H8] ( $p < 0.05$ ), whereas alprenolol significantly increased the conformational variability of [H1.1] ( $p < 0.05$ ) (**Table 3.4**). These results show that ligand binding increases the conformational variability (or states) of certain structural regions of  $\beta_2$ AR whereas all other structural regions were not affected significantly. It appeared, that some structural regions were modulated by different ligands whereas other regions were modulated by only one ligand. However, to which extent the conformational variability of a structural region changed was specific to the ligand.

### **3.4.1.4 Structural segments changing lifetime upon ligand binding**

The transition rate  $k_0$  measures the lifetime (reciprocal of transition rate) of a structural segment. The DFS experiments (**Table 3.4**) detected that binding of BI, THRX, or adrenalin significantly increased the lifetime of the structural segment [H3-C2-H4-E2-H5.1] ( $p < 0.001$ ), that carazolol binding significantly increased the lifetime of the structural segments [H1.2-C1] ( $p < 0.001$ ), [H2.1] ( $p < 0.05$ ), [H3-C2-H4-E2-H5.1] ( $p < 0.001$ ) and [H6.2-E3-H7-H8] ( $p < 0.05$ ), and that alprenolol binding significantly increased the lifetime of the structural

segment [H1.1] ( $p < 0.05$ ) (**Table 3.4**). These results demonstrate that ligand binding changes the kinetic properties of structural regions within  $\beta_2$ AR. However, to which extent the kinetic properties of a structural region changed was again specific to the ligand.

#### 3.4.1.5 Structural segments changing free energy upon ligand binding

The free energy  $\Delta G_0^\ddagger$  characterizes the height of the energy barrier stabilizing a folded structure (**Figure 2.3**, see section 2.8.3). DFS measurements showed that ligand binding increased the free energy of several structural segments (**Table 3.4**). Binding of BI, THRX and adrenalin significantly increased  $\Delta G_0^\ddagger$  of structural segment [H3-C2-H4-E2-H5.1] ( $p < 0.001$ ), carazolol significantly increased  $\Delta G_0^\ddagger$  of structural segments [H1.2-C1] ( $p < 0.001$ ), [H2.1] ( $p < 0.05$ ), [H3-C2-H4-E2-H5.1] ( $p < 0.001$ ) and [H6.2-E3-H7-H8] ( $p < 0.05$ ), and alprenolol significantly increased  $\Delta G_0^\ddagger$  of structural segment [H1.1] ( $p < 0.05$ ).

#### 3.4.1.6 Structural segments changing mechanical properties upon ligand binding

Similar to the other parameters characterizing the energy barriers the spring constants  $\kappa$  that quantify the mechanical rigidity of structural segments (135, 230), changed upon ligand binding (**Table 3.4**). Binding of the agonists BI, THRX, and adrenalin significantly increased the mechanical elasticity of the core structural segment [H3-C2-H4-E2-H5.1] ( $p < 0.001$ ), and alprenolol significantly decreased the mechanical elasticity of structural segment [H1.1] ( $p < 0.05$ ). Carazolol significantly increased the mechanical elasticity of structural segments [H1.2-C1] ( $p < 0.001$ ), [H3-C2-H4-E2-H5.1] ( $p < 0.001$ ), and [H6.2-E3-H7-H8] ( $p < 0.05$ ), and decreased that of structural segment [H2.1] ( $p < 0.05$ ). These results showed that the binding of a ligand changed the mechanical properties of certain structural regions.

### 3.4.2 Discussion

#### 3.4.2.1 Ligand binding to $\beta_2$ AR lacks pronounced localized interactions

As for all membrane proteins investigated so far by SMFS (114, 129, 130, 133, 135, 156, 233, 234) the F-D spectra recorded during mechanical unfolding of native-like  $\beta_2$ AR reconstituted into proteoliposomes showed a reproducible pattern of force peaks (**Figure 3.4C** and **Figure 3.6**). The reproducibility of the force peak pattern suggests that  $\beta_2$ AR establishes a characteristic interaction network (125). Ligand binding to the receptor did not establish additional force peaks or significantly modify the strength of existing force peaks. In contrast, SMFS detected a significantly increased force peak after ligand binding to functionally activated  $\text{Na}^+/\text{H}^+$  antiporters NhaA from *Escherichia coli* and MjHhaP1 from *Methanococcus jannaschii* (127, 128). The increasing interaction force was correlated to specific interactions established between the ligand  $\text{Na}^+$  and the deprotonated aspartic acid residues at the  $\text{Na}^+$ -binding site. In  $\beta_2$ AR multiple amino acid residues from several transmembrane  $\alpha$ -helices contribute to ligand binding (188, 189). Thus, it is expected that ligand binding modulates the functional state of  $\beta_2$ AR by changing the interaction network in the GPCR (224, 252). However, because no drastic changes of the force peak pattern were detected such as observed for other membrane proteins after ligand binding (127, 128), it can be concluded that ligand binding established rather small changes to the interactions that structurally stabilize  $\beta_2$ AR in the unliganded conformation.

#### 3.4.2.2 Conformational variability and kinetic stability of unliganded $\beta_2$ AR

DFS studies showed that structural segments of bacteriorhodopsin, bovine and mouse rhodopsin, the antiporter NhaA and the transporter BetP are stabilized by single energy barriers (**Figure 2.3**, see section 2.8.3) (129, 133, 232, 234, 253). The same observation was made for the structural segments of  $\beta_2$ AR. The transition state distance  $x_u$  separating

the folded from the unfolded state of every structural segment of  $\beta_2$ AR ranged from 0.3 to 0.6 nm (**Table 3.4**). Thus the structural segments of  $\beta_2$ AR must be stretched by  $\approx 0.3$  to 0.6 nm to induce unfolding. These rather short distances suggest that short ranged inter- and intramolecular bonds, such as hydrogen bonds, van-der-Waals interactions, or electrostatic interactions had to be ruptured to induce unfolding of the receptor. On average, the transition state distance of structural segments determined of  $\beta_2$ AR was similar to the average values of  $\approx 0.4$  nm determined for structural segments stabilizing bacteriorhodopsin, bovine rhodopsin and NhaA ( $x_u$  ranging from 0.2 to 0.8 nm) (129, 232, 234, 253). The structural segments of unliganded  $\beta_2$ AR revealed transition rates  $k_0$  between 0.011 and 0.320 s<sup>-1</sup> (**Table 3.4**), indicating lifetimes ranging between  $\approx 3$  and  $\approx 90$  s. These transition rates were in the range of those measured for other membrane proteins ranging from 0.001 to 0.9 s<sup>-1</sup> (129, 232, 234, 253). However, the  $k_0$  values of the structural segments of  $\beta_2$ AR differed by a factor of 30 with structural segments [H1.1], [H3-C2-H4-E2-H5.1] and [CT] representing the kinetically stable regions, and [H1.2-C1], [H2.1] and [H6.2-E3-H7-H8] the kinetically less stable ones. Biophysical and functional studies support a multistate model of  $\beta_2$ AR in the absence of ligands (254). These multiple conformational and functional states observed for unliganded  $\beta_2$ AR may be directly related to the conformational variability and kinetic heterogeneity of the receptor's structural segments observed by DFS.

#### 3.4.2.3 Energetic stability and mechanical elasticity of unliganded $\beta_2$ AR

The free energy barrier  $\Delta G_0^\ddagger$  stabilizing the structural segments of unliganded  $\beta_2$ AR ranged from  $\approx 20$  to 23  $k_B T$ . These free energy differences were below that determined for structural segments of bovine rhodopsin in the inactive dark-state ( $\Delta G_0^\ddagger$  between 20 and 28  $k_B T$ ) and below those determined for the structurally similar but functionally different bacteriorhodopsin ( $\Delta G_0^\ddagger$  between 21 and 29  $k_B T$ ) (234, 253). Thus

the structural segments of unliganded  $\beta_2$ AR were energetically less stable compared to those of bovine rhodopsin and bacteriorhodopsin.

Spring constants characterizing the mechanical elasticity of structural segments in the unliganded state varied by a factor of four (**Table 3.4**). The intracellular end of  $\alpha$ -helix H1 together with the first intracellular loop [H1.2-C1] ( $\kappa=2.02$  N/m) and the structural segment [H5.2-H6.1-C3] ( $\kappa=2.23$  N/m) formed the most rigid structures of the receptor. In contrast, the core segment [H3-C2-H4-E2-H5.1] ( $\kappa=0.59$  N/m) and the C-terminal domain [CT] ( $\kappa=0.54$  N/m) formed the most elastic segments. In general, the structural segments stabilizing  $\beta_2$ AR were more elastic compared to the structural segments of bacteriorhodopsin, where the values for  $\kappa$  ranged from 0.9 to 4.2 N/m (253). Compared to the elasticity of the structural segments of bovine rhodopsin ( $\kappa$  between 0.16 and 2.54 N/m) (234), the values observed for  $\beta_2$ AR were more similar, indicating that both class A GPCRs share consistent mechanical properties. However, the spring constants of the structural core segments [H3-C2-H4-E2-H5.1] of both GPCRs differed from each other. In the case of unliganded  $\beta_2$ AR,  $\kappa$  was about four times lower than  $\kappa$  of bovine rhodopsin in the dark-state.

#### **3.4.2.4 High conformational variability and mechanical elasticity of structural core correlates to basal $\beta_2$ AR activity**

Parameters characterizing the energy barrier stabilizing unliganded  $\beta_2$ AR describe the receptor in its basal and low energy state (224). It has been suggested that the basal activity of  $\beta_2$ AR in the absence of ligands may be attributed to an inherent structural flexibility and tendency to adopt several conformational states (224). In the measurements, the largest segment in the receptor core [H3-C2-H4-E2-H5.1] exposed a relatively high conformational variability (high  $x_u$ ) and high mechanical elasticity (low  $\kappa$ ) compared to the other structural segments of  $\beta_2$ AR and compared to the core segment of the GPCR bovine rhodopsin in the dark-state. This dark-state of rhodopsin is stabilized by the covalently bound chromophore that acts as inverse agonist and traps

the GPCRs in the inactive state (255, 256). Since the core segment of  $\beta_2$ AR contains multiple ligand-binding sites (188, 189), the increased conformational variability and mechanical elasticity allows the core to sample more conformational states required to interact with a variety of different ligands. Thus, the DFS experiments suggest that the high conformational variability and mechanical elasticity of the core segment (**Table 3.4**) contribute to the basal activity of  $\beta_2$ AR and favor ligand binding.

#### 3.4.2.5 Properties of $\beta_2$ AR modified by the neutral antagonist alprenolol

Neutral antagonists bind in the orthosteric pocket of a GPCR but have little or no effect on basal activity. In contrast to all other ligands tested, the neutral antagonist alprenolol only modulated the N-terminal region of transmembrane  $\alpha$ -helix H1 ([H1.1]) and widened the energy valley  $x_u$  from 0.44 nm (unliganded) to 0.75 nm. Thus, alprenolol enhanced the conformational variability of the extracellular half of  $\alpha$ -helix H1. Furthermore, binding of alprenolol significantly reduced the transition rate  $k_0$  and increased the lifetime of structural segment [H1.1]. The free energy  $\Delta G_0^\ddagger$  stabilizing structural segment [H1.1] increased by  $\approx 7 k_B T$ , whereas the spring constant  $\kappa$  decreased to 0.40 N/m (0.88 N/m in the unliganded state). These changes show that alprenolol kinetically and energetically stabilizes the extracellular part of  $\alpha$ -helix H1 and enhances its mechanical elasticity. Available crystal structures do not explain these observations. It has been suggested that  $\alpha$ -helix H1 is involved in receptor silencing by oligomerization (243, 244). Therefore, it may be speculated that the alprenolol induced kinetic and energetic stabilization as well as the structural softening of the extracellular half of  $\alpha$ -helix H1 favor oligomerization of the receptor.

Although the affinity of alprenolol ( $K_d \approx 1$  nM) is comparable to that of the agonist THRX and greater than that of adrenalin, binding of the neutral antagonist did not show any effects on the structural core segment [H3-C2-H4-E2-H5.1]. Thus, alprenolol established very different

interactions compared to THRX and to other agonists (**Table 3.4**). A possible explanation for this quite unique interaction pattern established in  $\beta_2$ AR could be that alprenolol has a single aromatic ring that cannot establish strong interactions with F193 of loop E2, as shown by molecular dynamics docking simulations (257). Moreover, in contrast to both agonists and carazolol, alprenolol does not form polar interactions with serine residues of  $\alpha$ -helix H5. This may explain that alprenolol cannot establish interactions at the core segment that are supposed to change the activity of  $\beta_2$ AR. In summary, the DFS measurements unravel how a neutral antagonists works by simply constricting the access of other ligands to the receptor (258) and avoiding interactions at functionally important regions.

#### **3.4.2.6 An overall scheme: most ligands modulate the structural core segment of $\beta_2$ AR**

To investigate to which extent ligands change the energetic, kinetic and mechanical properties of  $\beta_2$ AR, DFS was applied in the presence of the synthetic agonists BI and THRX, the natural agonist adrenalin, the inverse agonist carazolol or the neutral antagonist alprenolol. **Figure 3.12** highlights which ligands modulate the properties of different structural segments of  $\beta_2$ AR. Binding of both agonists and the inverse agonist carazolol significantly modified the energetic, kinetic and mechanical parameters of the structural core segment [H3-C2-H4-E2-H5.1]. The magnitude of the effect correlates relatively well with ligand affinity, with the lowest values being observed for the highest affinity ligands. This is may be explained by extensive interactions between ligands and transmembrane  $\alpha$ -helices H3 and H5. As noted above, the small effect observed for the neutral antagonist alprenolol may be explained by the absence of polar interactions between alprenolol and transmembrane  $\alpha$ -helix H5. In the presence of agonists and carazolol, the energy valley stabilizing the structural core segment increased its distance to the transition state  $x_u$  from 0.55 nm (unliganded  $\beta_2$ AR) to 0.73 nm (THRX), 0.71 nm (BI), 0.65 nm (adrenalin) and 0.79 nm (carazolol).

This shift towards wider energy valleys in these ligand bound states implies that the core segment [H3-C2-H4-E2-H5.1] increases conformational variability in response to ligand binding. Furthermore, the reduction of the transition rate  $k_0$  of the core segment by several orders of magnitude suggests that this structural region of  $\beta_2AR$  increases lifetime by orders of magnitude in the presence of BI, THR<sub>X</sub>, adrenalin or carazolol. The spring constant  $\kappa$  of the core segment [H3-C2-H4-E2-H5.1] is slightly reduced from 0.59 N/m (unliganded state) to 0.48 N/m (BI), 0.44 N/m (THR<sub>X</sub>), 0.49 N/m (adrenalin) and 0.39 N/m (carazolol). This reduction in  $\kappa$  indicates that the core segment increases mechanical elasticity by  $\approx 10-20\%$ . Finally, ligand binding stabilized the  $\beta_2AR$  core segment [H3-C2-H4-E2-H5.1] by increasing free energy  $\Delta G_0^\ddagger$  by  $7.7 k_B T$  (BI),  $6.9 k_B T$  (THR<sub>X</sub>),  $3.2 k_B T$  (adrenalin) and  $7.6 k_B T$  (carazolol), compared to unliganded  $\beta_2AR$ . Thus, the high-affinity ligands BI, THR<sub>X</sub> and carazolol increased the free energy stabilizing the core segment twice as much compared to the natural agonist adrenalin.

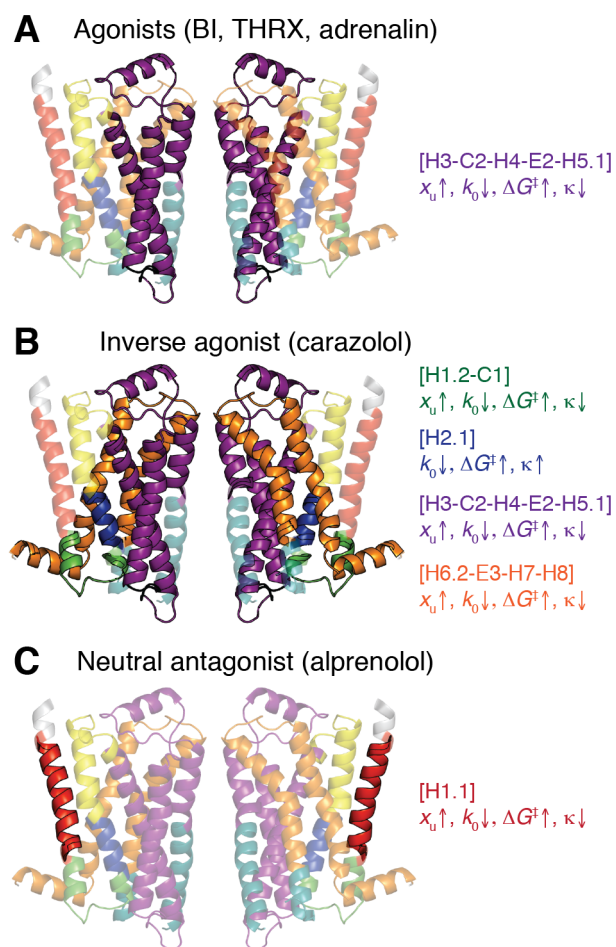


**Figure 3.12: Structural segments of  $\beta_2$ AR changing properties upon ligand binding.** Structural segments that significantly change their energetic, kinetic and mechanical properties upon binding of BI, THRX or adrenalin (A), carazolol (B) and alprenolol (C) are highlighted ( $\beta_2$ AR structure PDB ID code 2RH1). Arrows denote increasing (arrow up) and decreasing (arrow down) parameters characterizing the width of the energy valley ( $x_u$ ), transition rate ( $k_0$ ), energy barrier ( $\Delta G_0^\ddagger$ ), and spring constant ( $\kappa$ ) of stable structural segments. Trends were taken from **Table 3.4**.

Structural and functional data suggest that the core segment [H3-C2-H4-E2-H5.1] is important for ligand binding and  $\beta_2$ AR activation: (i) several amino acid residues of transmembrane  $\alpha$ -helices H3 and H5 are part of the ligand-binding pocket (259). For instance, H3 and H5.1 establish polar interactions and hydrophobic contacts with BI (189). Two residues of H3, D113 and V114, contribute to agonist binding (189). Furthermore, S203 of H5.1 is crucial for agonist binding, as shown by mutagenesis studies (260, 261). (ii) Receptor activation by agonists involves disruption of the ionic lock, which links the cytoplasmic parts of  $\alpha$ -helices H3 and H6 in the inactive state (262, 263). (iii) The second intracellular loop C2 is important for the efficiency of G protein activation and contains a switch that enables G protein coupling (264, 265).

In summary, DFS detected that binding of agonists and the inverse agonist carazolol increases structural flexibility, energetic stability and lifetime (kinetic stability) of the functionally important core segment [H3-C2-H4-E2-H5.1]. These altered properties of the core segment enable

$\beta_2$ AR to adopt certain conformations, which are supposed to represent an active state.

The affinities of the agonists investigated range from  $K_d=0.84$  pM (BI) to  $K_d=3.68$   $\mu$ M (adrenalin).  $K_d$  of THRX is  $\approx 1$  nM. Each agonist changed the conformational variability, kinetic stability, energetic stability, and mechanical elasticity of the structural core segment [H3-C2-H4-E2-H5.1] differently. A systematic change may be found between the kinetic stability of [H3-C2-H4-E2-H5.1], which increased with increasing affinity of the agonists that bound to  $\beta_2$ AR. However, it should be noted that binding of agonists alone is insufficient to stabilize  $\beta_2$ AR in the active state (266, 267). Even binding of full agonists cannot stabilize every  $\beta_2$ AR in the active state (219, 268). The reason for this apparent discrepancy is that although bound to a ligand the probability of  $\beta_2$ ARs to adopt other functional states lowers but does not approach zero (224). Interestingly, the active state can be further stabilized through interactions with G proteins or camelid antibodies (nanobodies) that exhibit G protein-like behavior (189, 267). Characterizing such stable  $\beta_2$ AR/G protein complexes using DFS may be useful to quantify the conformational variability, kinetic stability, energetic stability, and mechanical elasticity of the structural core segment [H3-C2-H4-E2-H5.1] in the fully active state.

#### **3.4.2.7 The inverse agonist carazolol introduces major modifications to $\beta_2$ AR**

Among all ligands tested, carazolol modulated the properties of most structural segments of  $\beta_2$ AR. Besides changing the energetic, kinetic and mechanical properties of the core segment [H3-C2-H4-E2-H5.1] such as observed for the agonists, carazolol significantly affected three other structural segments [H1.2-C1], [H2.1], and [H6.2-E3-H7-H8] (**Table 3.4**). Carazolol widened the energy valley stabilizing [H1.2-C1], [H3-C2-H4-E2-H5.1], and [H6.2-E3-H7-H8] by 0.10-0.27 nm. This indicates that these segments enhanced their conformational variability. Furthermore, carazolol reduced the transition rate  $k_0$  and, thus, increased the lifetime

of each of the four structural segments by up to 6 orders of magnitude. The free energy  $\Delta G_0^\ddagger$  of structural segments [H1.2-C1] and [H3-C2-H4-E2-H5.1] increased by  $\approx 10 k_B T$ . Carazolol slightly lowered the spring constants  $\kappa$  of structural segments [H2.1], [H3-C2-H4-E2-H5.1] and [H6.2-E3-H7-H8], thereby increasing their structural elasticity. The strongest effect was observed for the structural segment [H1.2-C1], where  $\kappa$  reduced from 2.02 N/m in the unliganded state to 0.83 N/m in the carazolol-bound state.

Several amino acid residues of  $\alpha$ -helices H3, H5, H6 and H7 are important for carazolol binding (188). For instance, W109, V114 and V117 of  $\alpha$ -helix H3 establish hydrophobic contacts with carazolol. Additionally, polar interactions between carazolol and D113 of  $\alpha$ -helix H3 as well as S203 of H5.1 are crucial for carazolol binding. Furthermore, hydrophobic contacts between W286, F289 and F290 of  $\alpha$ -helix H6 and carazolol contribute to binding of the inverse agonist (65, 66). Moreover, loop E2 of the structural segment [H3-C2-H4-E2-H5.1] establishes a salt bridge with extracellular loop E3 in the inactive state (257). Carazolol stabilizes packing interactions involving I121 (H3), P211 (H5.1), F282 (H6.2) and N318 (H7) that contribute to a network of interactions that stabilize an inactive conformation of the receptor (267). Thus, from this point it may not be surprising that the experiments detect that the structural segments [H3-C2-H4-E2-H5.1] and [H6.2-E3-H7-H8] change their properties upon carazolol-binding. However, DFS quantifies to which extent the properties of these and other structural regions change.

#### **3.4.2.8 Carazolol modifies structural regions proposed to be involved in oligomerization**

Inverse agonists promote higher-order  $\beta_2$ AR oligomerization that alters access to other signaling proteins (225). The significant changes of the energy barriers ( $x_u$ ,  $k_0$  and  $\Delta G_0^\ddagger$ ) and spring constants ( $\kappa$ ) characterizing the structural segments [H1.2-C1], [H3-C2-H4-E2-H5.1] and [H6.2-E3-H7-H8] in the presence of carazolol are of particular interest because they significantly increase conformational variability,

mechanical flexibility, kinetic stability and energetic stability upon carazolol-binding. It has been proposed for several other class A GPCRs that oligomerization involves primarily the interface between  $\alpha$ -helices H1 and H8 (243, 244). Thus, all structural segments changing their properties may contribute to the oligomerization of  $\beta_2$ AR. Particularly  $\alpha$ -helices H4 and H5 are involved in the native packing arrangement of rhodopsin and define the rhodopsin dimer (243). It is therefore likely that the increased conformational variability of the core segment [H3-C2-H4-E2-H5.1] contributes to the formation of dimers and higher-ordered oligomers in the presence of carazolol. Conversely, interactions between protomers that change their oligomeric state can influence the parameters quantified by DFS (136). Thus, it cannot be distinguished whether changes of the structural segments are induced by carazolol binding or carazolol-induced oligomerization.

#### **3.4.2.9 Carazolol employs direct and indirect interactions to modify structural regions**

Although carazolol binds to  $\beta_2$ AR with picomolar affinity (comparable to BI), it significantly changed the energy landscape of four structural segments. The effect of carazolol on the energy landscape of the receptor is more pronounced compared to the effects caused by any of the other agonists or the neutral antagonist investigated. Not all of the structural segments are supposed to interact directly with carazolol (188). Thus, it can be concluded that carazolol binding changes the properties of the structural regions of  $\beta_2$ AR by direct interactions and by indirect interactions, which do not result from directly contacting the ligand.

### **3.5 Conclusions**

Energy landscapes describe conformational variability, kinetic stability, energetic stability and mechanical elasticity of proteins (231). GPCRs adopt many different conformations that are closely related to functional states (224). The work presented here contributes to a more detailed understanding of the energetic, kinetic and mechanical properties of native-like  $\beta_2$ AR reconstituted into membranes of

phospholipids and cholesterol. It was observed that the interactions of unliganded  $\beta_2$ AR stabilize well-defined structural segments of the receptor.

Cholesterol considerably increased the strength of interactions stabilizing structural segments of  $\beta_2$ AR. These interactions introduced by cholesterol were sufficient to increase the kinetic, energetic, and mechanical stability of all structural segments stabilizing  $\beta_2$ AR except for the structural core segment [H3-C2-H4-E2-H5.1], whose properties were not significantly influenced by cholesterol. Because the core segment of  $\beta_2$ AR is involved in ligand binding, this finding indicates that cholesterol may not necessarily influence the binding of a ligand to the structural core segment. It could not be distinguished to which extent the change introduced to all other stable structural segments were caused by the binding of cholesterol to the receptor or indirectly through the ability of cholesterol to modulate the properties of the lipid bilayer. At least the structural segments of  $\beta_2$ AR that do not expose cholesterol binding sites must have changed properties through indirect interactions mediated by cholesterol. In summary the changing properties detected in the presence of cholesterol are of sufficient magnitude to alter the structure and function relationship of  $\beta_2$ AR (245). The fact that cholesterol increases stability of the receptor supports the hypothesis that cholesterol is an essential component in the crystallization of  $\beta_2$ AR (65). Taken together, the unchanged structural core segment containing multiple ligand binding sites and the changed properties of all other structural segments may represent a mechanism of how cholesterol modulates  $\beta_2$ AR. As cholesterol may not necessarily influence the binding of a ligand to  $\beta_2$ AR, the data suggests that in the presence of cholesterol the GPCR will react differently once a ligand has bound.

In the presence of a ligand, SMFS could not detect drastic changes of interactions and the stabilizing structural segments did not change positions. Thus, it can be concluded that ligand binding to  $\beta_2$ AR induces rather weak interactions instead of strong localized interactions.

However, DFS showed that the interactions established upon ligand binding were sufficient to change the conformational, energetic, kinetic and mechanical properties of structural segments of  $\beta_2$ AR. Agonist or inverse agonist binding increased the conformational variability, kinetic stability, energetic stability and mechanical elasticity of the functionally important structural core segment [H3-C2-H4-E2-H5.1] of  $\beta_2$ AR. To which extent individual ligands could change the properties of the core segment was intrinsic to the ligand. In contrast to the agonists (BI, THRX, and adrenalin), the inverse agonist carazolol affected, in addition to the core segment, three structural segments: [H1.2-C1], [H2.1], and [H6.2-E3-H7-H8]. Finally, the neutral antagonist alprenolol changed only the properties of structural segment [H1.1]. The functionally important structural core segment of the receptor remained unaffected by alprenolol. Taken together, these single-molecule experiments reveal that ligands establish interactions that modulate the properties of distinct structural segments within  $\beta_2$ AR. Quantifying the energetic, kinetic and mechanical parameters of the structural segments provides insight into how these structural segments stabilize ligand-specific conformations of the receptor. Depending on which structural segments change their energetic, kinetic or mechanical properties, the receptor samples more active states in the presence of agonists or more inactive states in the presence of the inverse agonist.



## **4 Single-molecule force spectroscopy from lipid nanodiscs**

Reprinted (adapted) with permission from Zocher M., C. Roos, S. Wegmann, P. D. Bosshart, V. Dotsch, F. Bernhard, and D. J. Müller. 2012. Single-molecule force spectroscopy from nanodiscs: an assay to quantify folding, stability, and interactions of native membrane proteins. *ACS Nano* 6:961-971. Copyright 2012 American Chemical Society.

### *Publication*

M. Zocher *et al.* (2012), *ACS Nano*

### *Author contributions*

**Michael Zocher**: Experimental planning and setup, SMFS experiments, SFMS data analysis, figure preparation & manuscript writing

Christian Roos: Preparation of Bacteriorhodopsin embedded in nanodiscs, UV/vis and CD spectroscopy

Susanne Wegmann: AFM imaging

Patrick D. Bosshart: SMFS of native Bacteriorhodopsin

V. Dötsch, F. Bernhard & Daniel J. Müller: Project initiation and supervision



## **4.1 Introduction**

To reveal insights into membrane proteins by SMFS requires the membrane protein to be embedded in a lipid membrane. These membranes can be extracted from the native cell or synthetic lipid membranes into which the membrane protein has been reconstituted. In contrast to the thousands of different membrane proteins known, only a few could be reconstituted into the functionally important lipid membrane (13, 57, 269). These difficulties are based on the amphiphilic character of membrane proteins that once isolated from the cell membrane must be reconstituted into a lipid bilayer that mimics the native cellular membrane.

Recently, phospholipid nanodiscs have been introduced to reconstitute membrane proteins into a native-like lipid environment (269-271). Nanodiscs are composed of small patches ( $\approx 10$ -20 nm in diameter) of lipid bilayer framed by an amphiphilic membrane scaffold protein (MSP) to shield the hydrophobic fatty acid chains of the lipids from the aqueous buffer solution. MSP itself is based upon the sequence of human serum apolipoprotein A1, which are the primary component of high-density lipoproteins (rHDL). The shielding of hydrophobic interactions by the MSP makes lipid nanodiscs water-soluble. The phospholipids associate as a bilayer domain while two MSP molecules wrap around the edges of the discoidal structure (272). One MSP covers the hydrophobic alkyl chain of each leaflet. Therefore, after integration into nanodiscs, membrane proteins can be handled similar to water-soluble proteins. Because the length of the scaffold protein determines the diameter of the nanodisc and the lipid composition of the nanodisc can be adjusted, the properties of the nanodisc can be tailored to favor the insertion of a particular membrane protein (271). Accordingly, several membrane proteins have already been embedded into lipid nanodiscs including the bacterial chemoreceptor Tar (273), cytochrome P450 (274), the translocon SecYEG (275), BR (276),  $\beta_2$ AR (266, 277) and bovine rhodopsin (278). Structural and functional characterization of these membrane proteins

demonstrated that nanodiscs are capable of mimicking a physiological environment for *in vitro* studies (273, 279-282).

Another bottleneck limits the applicability of SMFS to membrane proteins. To conduct SMFS the protein containing membrane must be first imaged and located so that the AFM tip can be attached to the membrane protein. Once the AFM tip has been attached the stability, folding and interactions of the membrane protein can be characterized (125, 156, 283). These constraints could be avoided if membrane proteins could be reconstituted into nanoscopic lipid bilayers that provide a native-like environment of membrane proteins and that could be densely adsorbed onto the SMFS support. In a raster-like manner the AFM tip could then pick up and characterize one membrane protein after the other without the need of imaging. Dense adsorption layers on supporting surfaces can be prepared with hydrophilic water-soluble proteins (143). In contrast, reconstituted proteoliposomes showing a heterogeneous distribution of diameters from  $\approx 50$  to  $>500$  nm. If adsorbed at higher concentration onto a support, proteoliposomes start forming aggregates that are not suitable for SMFS. However, in principle dense adsorption layers may be obtained using membrane proteins that are embedded in hydrophilic nanodiscs. Such improved preparation procedures would simplify SMFS of membrane proteins and be a basis to apply high-throughput SMFS assays (284, 285) to study membrane protein (un-)folding, stability and interactions.

For these reasons, it was investigated whether membrane proteins reconstituted into phospholipid nanodiscs can be characterized by SMFS and to which extent the reconstitution into nanodiscs modulates the interactions guiding the stability and (un-)folding of membrane proteins. Among membrane proteins the light-driven proton pump bacteriorhodopsin (BR) from *Halobacterium salinarum* most probably represents the functionally and structurally best characterized example (286-289). Moreover, since many years BR serves as model to characterize the unfolding and folding of  $\alpha$ -helical transmembrane proteins (44, 80,

156, 290, 291) (see section 2.8.1). Thus, BR was chosen as example for the SMFS studies presented here. For that purpose, BR from native purple membrane (BR<sub>PM</sub>) and BR reconstituted into phospholipid nanodiscs (BR<sub>ND</sub>) were characterized by SMFS. The mechanical unfolding pathways and the stability of both BR samples were compared and their interactions mapped onto the BR structure. The results showed whether the reconstitution of BR into lipid nanodiscs alters the properties of BR and whether nanodiscs can in principle be applied to characterize membrane proteins by SMFS.

## 4.2 Experimental procedures

### 4.2.1 Expression and purification of MSP1

MSP1 was expressed and purified in Volker Dötsch's laboratory at the University of Frankfurt. *Escherichia coli* BL21 star (DE3, Invitrogen, Germany) were transformed with the plasmid containing the MSP1 gene (pET28b-MSP1). The MSP1 had an N-terminal 6-His affinity tag and a tobacco etch virus (TEV) protease cleavage site (271). A pre-culture was incubated overnight in lysogeny broth medium (supplemented with 30 µg kanamycin) and diluted 30-fold in expression media (lysogeny broth medium, supplemented with 0.5% (w/v) glucose and 30 µg/ml kanamycin). *Escherichia coli* were grown at 37°C with shaking (180 rpm). Expression of MSP1 was induced by adding isopropyl-b-D-thiogalactopyranosid (IPTG) to a final concentration of 1 mM when the optical density at  $\lambda = 600$  nm (OD<sub>600</sub>) reached 1. Subsequently, the cells were incubated under continuous shaking (180 rpm) for 1 h at 37°C before the temperature was decreased to 28°C for additional 4 h. Bacteria were pelleted and stored at -20°C. Bacteria pellets of 1.2 l expression culture were resuspended in 50 ml breaking buffer (300 mM NaCl, 1 protease inhibitor tablet (cComplete Protease Inhibitor Cocktail Tablet, Roche, Germany), 1 mM phenylmethanesulfonylfluoride (PMSF), 40 mM Tris-HCl, pH 8.0). Triton X-100 was added to a final concentration of 1% (v/v). Cells were disrupted using a Labsonic homogenizer (Braun, Germany) for 3 x 60 s and 3 x 45 s (pulse length 0.7 s) on ice. The suspension was centrifuged at 30.000g for

20 min to separate unbroken bacteria from bacteria debris. The supernatant was filtered (pore size 0.45  $\mu\text{m}$ ) before loading on an immobilized metal ion affinity chromatography column (IMAC Sepharose 6 FF, GE Healthcare, USA). The IMAC column was equilibrated with 5 column volumes of buffer 1 (300 mM NaCl, 40 mM Tris-HCl, 1% Triton-X (v/v), pH 8.0) before loading the supernatant. The column was washed successively with 5 column volumes of buffer 1 to 4 (buffer 2: 300 mM NaCl, 50 mM cholic acid, 40 mM Tris-HCl, pH 8.9; buffer 3: 300 mM NaCl, 40 mM Tris-HCl, pH 8.0; buffer 4: 300 mM NaCl, 50 mM imidazol, 40 mM Tris-HCl, pH 8.0) followed by the elution of MSP1 with elution buffer (300 mM NaCl, 300 mM imidazol, 40 mM Tris-HCl, pH 8.0). Purity of the elution fraction was analysed by SDS-PAGE. MSP1-containing fractions were pooled and glycerol was added to a final concentration of 10% (v/v) to prevent aggregation. MSP1 was dialysed against dialysis buffer (300 mM NaCl, 40 mM Tris-HCl, 10% glycerol (v/v), pH 8.0) for 16 h at 4°C with one buffer exchange. The dialysis was performed using Spectra/Por dialysis membranes with 10 kDa molecular weight cut off (Spectrum Laboratories, USA). MSP1 concentration was determined by absorption spectroscopy using the molar extinction coefficient at  $\lambda = 280$  nm ( $\epsilon = 24750 \text{ M}^{-1}\text{cm}^{-1}$ ). MSP1 was flash frozen in liquid nitrogen and stored at -80°C.

#### **4.2.2 Preparation of BR**

Purple membrane was kindly provided by G. Büldt. Purple membrane from strain *H. salinarum* S9 was purified as described (292). For reconstitution of BR into nanodiscs, purple membrane (concentration 4.5-6 mg/ml) was mixed with an equal volume of solubilization buffer (40 mM  $\text{Na}_2\text{HPO}_4/\text{KH}_2\text{PO}_4$ , 7.5% (w/v) *n*-octyl- $\beta$ -D-glucopyranoside ( $\beta$ -OG, Sigma-Aldrich, Germany), pH 6.9) and incubated at 4°C for  $\geq 2$  days to extract BR from purple membrane. The solution was centrifuged at 90.000g for 1 h to remove insoluble fragments. The supernatant containing solubilized BR (including some tightly bound purple membrane lipids) was used for nanodisc reconstitution with the BR concentration

being determined using the molar absorption coefficient at  $\lambda = 560$  nm ( $\epsilon = 42000 \text{ M}^{-1}\text{cm}^{-1}$ ).

### **4.2.3 Reconstitution of BR into nanodiscs**

BR was reconstituted into nanodiscs in Volker Dötsch's laboratory at the University of Frankfurt. Dimyristoylphosphatidylcholine (DMPC, Avanti Polar Lipids, USA) was added to water at a concentration of 50 mM and solubilized by adding sodium cholate to a final concentration of 100 mM. The detergent-lipid mixture was sonicated for 10 min at 35 kHz and 640 W in a water bath (Sonorex Super RK 510, Bandelin, Germany) and filtered (pore size 0.45  $\mu\text{m}$ ). BR was reconstituted into nanodiscs by mixing detergent-solubilized BR with MSP1 and DMPC at a stoichiometry of 1:1:10 (molar ratio). The BR-MSP1-DMPC mixture was incubated for 1 h at room temperature ( $\approx 23^\circ\text{C}$ ). To remove detergent and to induce nanodisc formation the mixture was dialyzed over night at room temperature against detergent-free buffer (100 mM NaCl, 40 mM Tris, pH 7.4) at a ratio  $\geq 1:500$ . Since no purification step was performed after solubilization of BR, the nanodiscs also contained wild-type lipids from purple membrane. The following dialysis was performed at  $4^\circ\text{C}$  for additional 2 days. The detergent-free buffer was exchanged at least twice. To avoid photo bleaching of BR (293), all reconstitution procedures were carried out in the dark. After dialysis the aggregated material was removed by centrifugation at 22.000g for 20 min. The supernatant was concentrated using Amicon ultra centrifugal filter units (Millipore, Germany, 10 kDa molecular weight cut off) to a final volume of 0.5 ml. BR<sub>ND</sub> complexes were purified using size-exclusion chromatography (Superdex 200, Tricorn 10/300, GE Healthcare, Germany) using dialysis buffer. Elution fractions with absorption maxima at  $\lambda = 530$  nm were pooled and concentrated using ultra centrifugal filter units (Amicon, 10 kDa molecular weight cut off) to a final concentration of  $\approx 100$  mM. Finally, the sample was centrifuged (20 min at 22.000g). The supernatant was stored at  $4^\circ\text{C}$  until analysis.

#### **4.2.4 UV/vis spectra**

UV/vis spectra of BR<sub>ND</sub> and BR<sub>PM</sub> were measured with a V-550 spectrophotometer (Jasco, UK) at room temperature. BR<sub>PM</sub> was diluted with buffer solution (100 mM NaCl, 40 mM Tris-HCl, pH 7.4). The buffer was used for baseline setting.

#### **4.2.5 Circular dichroism**

Circular dichroism (CD) spectra are frequently used to measure assembly and disassembly of the BR lattice (294, 295). Thus, CD was applied to determine the assembly of BR in nanodiscs CD spectra were measured with a J-180 spectrometer (Jasco, UK) in buffer solution (100 mM NaCl, 40 mM Tris-HCl, pH 7.4) at a protein concentration of 25.9  $\mu$ M. Measurements were carried out in a 1 mm cuvette at standard sensitivity with a band width of 3 nm, a response of 1 s and a scanning speed of 1 nm/s at 20°C.

#### **4.2.6 SMFS**

AFM imaging of BR<sub>PM</sub> and BR<sub>ND</sub> was performed using a Nanowizard II (JPK Instruments, Germany) and a Multimode8 AFM (Bruker, Germany). SMFS on BR<sub>PM</sub> was conducted using a NanoWizard II (JPK Instruments), whereas BR<sub>ND</sub> was approached using a ForceRobot 300 (JPK Instruments). The rectangular 200  $\mu$ m long AFM cantilevers (OMCL-RC800PSA, Olympus, Japan) having a nominal spring constant of  $\approx$ 0.05 N/m were calibrated in buffer solution using the equipartition theorem (227). Determined spring constants were within  $\approx$ 10% of each other. Experiments were carried out using AFM cantilevers from the same wafer. To non-specifically attach the AFM tip to BR, the tip was pushed on the purple membrane or BR<sub>ND</sub> applying a force of  $\approx$ 1 nN for 1 s (136, 156). Subsequent retraction of the AFM cantilever induced mechanical load that unfolded BR. While retracting the AFM cantilever at a velocity of 528 nm/s, the cantilever deflection was recorded to measure the force in dependence of the pulling distance. To record F-D curves, a x,y-raster of several hundred spots was defined. One F-D curve was recorded for every spot. In purple membrane the distance between

adjacent BR trimers corresponds to  $\approx 6.2$  nm. To ensure that single BR monomers were unfolded from intact BR trimers, the separation between adjacent spots was set  $\approx 20$  nm for purple membrane. To ensure that only one F-D curve per nanodisc was recorded, the distance between adjacent spots was set  $>50$  nm for BR<sub>ND</sub>. All SMFS experiments were performed using identical buffer solution (150 mM KCl, 20 mM Tris-HCl, pH 8.0) at room temperature.

#### **4.2.7 Selection and analysis of F-D curves**

First F-D curves were selected that exhibited an overall length between 60 nm and 70 nm, since they represented the complete unfolding of a BR into a fully stretched conformation (156). Then F-D curves were selected that corresponded to the C-terminal unfolding of BR (156, 296). All F-D curves were aligned using the characteristic force peak at a contour length of 88 amino acids as reference. Every force peak of a F-D curve was fitted using the worm-like chain (WLC) model (Section 2.8.2). Every force peak of every F-D curve was analyzed to quantify contour length and unfolding force (**Figure 4.5**). To determine the average force shown in histograms (**Figure 4.5C,D**) the average force of a particular force peak was calculated and multiplied by its probability of detection. This procedure gives the average force of an unfolding force peak from all unfolding F-D curves analyzed.

#### **4.2.8 Assignment of stable structural segments**

The contour length determined using the WLC model corresponds to the length of the unfolded and stretched BR polypeptide that tethers the AFM tip and a structural unfolding intermediate. Thus, each force peak was used to assign the end of the previous and the beginning of the following structural segment that stabilized BR against unfolding (125). Some stable structural segments had to be assumed to end or begin at the periplasmic BR surface at the opposite side of the pulling AFM tip. Therefore, the so-called ‘membrane compensation procedure’ was applied to correct the contour lengths (125, 159) (see section 3.2.5).

### 4.3 Results and discussion

#### 4.3.1 Mechanically unfolding single BR molecules from purple membrane and from nanodiscs

After reconstituting BR into dimyristoylphosphatidylcholine (DMPC) lipid nanodiscs absorption spectra of native purple membrane ( $BR_{PM}$ ) and of BR in nanodiscs ( $BR_{ND}$ ) were recorded (**Figure 4.1A**).  $BR_{PM}$  and  $BR_{ND}$  showed similar absorption spectra between 450 and 650 nm that are characteristic for the native light-driven proton pump BR (297). Thus, it can be concluded that reconstitution into lipid nanodiscs did not change the functional properties of BR significantly. To determine the assembly of BR in nanodiscs circular dichroism (CD) was used (294, 295). The CD spectra of  $BR_{ND}$  showed peaks in the visible spectrum from 400 to 700 nm (**Figure 4.1B**), which are typical for trimeric BR (298). The bilobed CD spectrum of  $BR_{ND}$  indicates that BR has been reconstituted into lipid nanodiscs as a trimer (298). In previous studies bilobed CD spectra indicating the BR trimerization could be only observed after heating the sample (298). However, a bilobed CD spectrum of  $BR_{ND}$  was observed without heating. This difference was attributed to the fact that a different detergent ( $\beta$ -OG compared to Triton-X used in (298)) to solubilize BR from purple membrane (see section 4.2). Consequently, BR trimers were reconstituted into lipid nanodiscs.

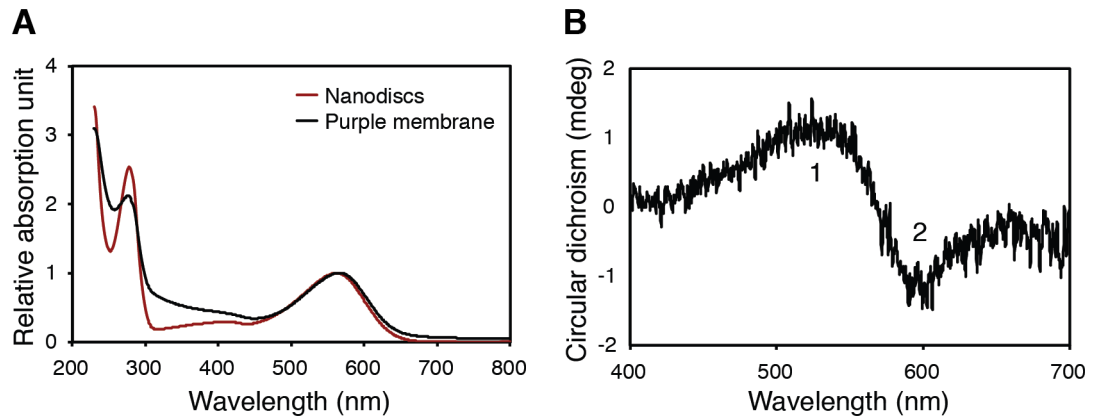


**Figure 4.1: UV/vis and CD spectra.** (A) UV/vis spectra of bacteriorhodopsin in purple membrane and of bacteriorhodopsin in nanodiscs. The co-factor specific absorption of  $BR_{PM}$  and  $BR_{ND}$  at a wavelength of 560 nm is very similar. Differences were detected in the range between 250 and 440 nm. These changes might be caused by lower light scattering of the nanodiscs (272) compared to purple membrane. Spectra were recorded in buffer solution (100 mM NaCl, 40 mM Tris-HCl, pH 7.4) at room temperature. (B) Circular dichroism (CD) spectra of bacteriorhodopsin in nanodiscs. The presence of a positive (1) and a negative peak (2) in the visible CD spectrum indicates the existence of trimeric BR in  $BR_{ND}$  (298). The spectrum represents an average of 3 measurements. Spectra were recorded in buffer solution (100 mM NaCl, 40 mM Tris-HCl, pH 7.4) at 20°C.

For SMFS native purple membrane ( $BR_{PM}$ ) or  $BR_{ND}$  was adsorbed to mica and imaged by AFM in buffer solution (**Figure 4.2**) (143). Whereas purple membranes were heterogeneously distributed over the supporting mica, the  $BR_{ND}$  complexes were homogeneously distributed and densely packed. To attach a single BR *via* unspecific interactions to the AFM tip (156), the tip was brought into contact with the sample ( $BR_{PM}$  or  $BR_{ND}$ ) applying a force of  $\approx 1$  nN for 1 s. In  $\approx 0.5\%$  ( $BR_{PM}$ ,  $n \approx 20.000$ ), or  $\approx 0.05\%$  ( $BR_{ND}$ ,  $n \approx 250.000$ ) of all cases a single BR molecule attached with its terminal end to the AFM tip (**Figure 4.3**). Withdrawal of the AFM tip stretched and stressed the terminal end and induced the unfolding of BR (156). The force-distance (F-D) curve recorded during withdrawal of the AFM tip showed a characteristic sawtooth-like pattern (**Figure 4.4A,B**) that has been assigned to the mechanical unfolding of BR from the C-terminal end (156, 159).

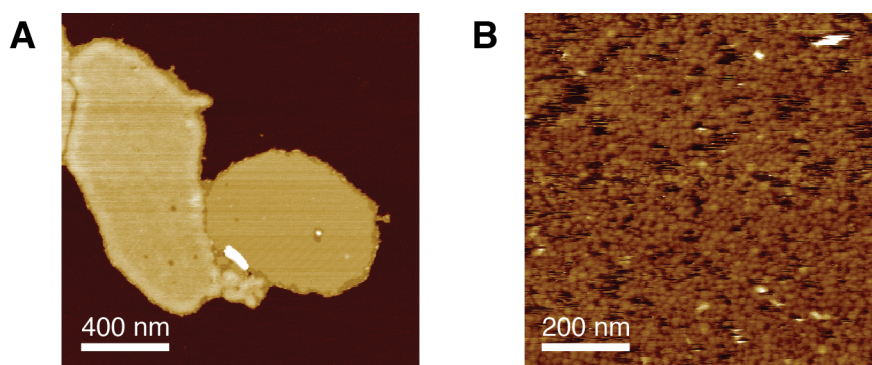


**Figure 4.2: AFM topographs of purple membrane (A) and nanodiscs containing bacteriorhodopsin (BR<sub>ND</sub>) (B).** Purple membrane and BR<sub>ND</sub> were adsorbed for 10 min onto freshly cleaved mica and imaged in buffer solution (300 mM KCl, 20 mM Tris-HCl, pH 8.0) at room temperature. Purple membranes have a diameter of 300-700 nm and BR<sub>ND</sub> have a diameter of  $\approx$ 10-20 nm. Both AFM topographs exhibit a full color scale corresponding to vertical scales of 15 nm. The AFM topograph in (A) was recorded using contact mode AFM applying a contact force of  $\approx$ 100 pN (93) and the topograph in (B) was recorded using force-volume AFM applying a maximal force of  $\approx$ 50 pN (299).

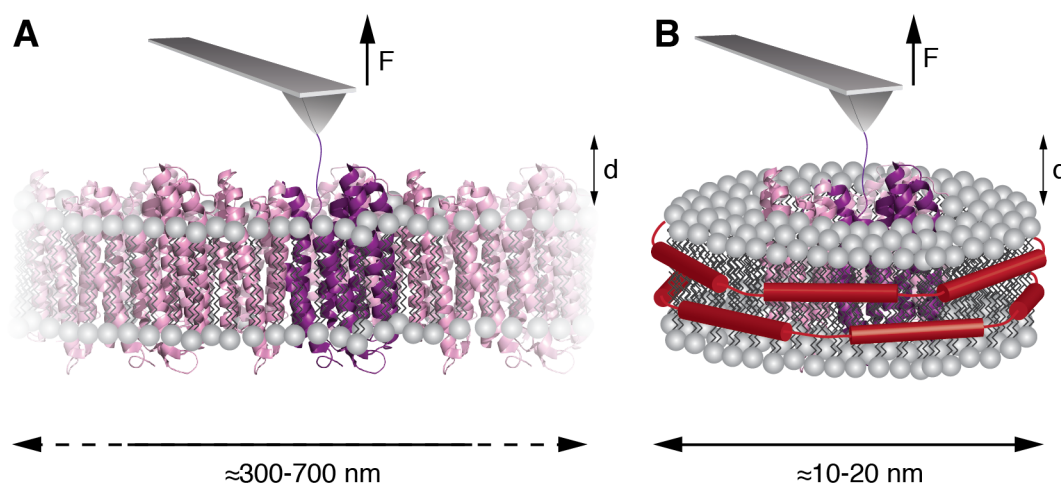


**Figure 4.3: Schematic representation of SMFS of bacteriorhodopsin (BR) embedded in native purple membrane (BR<sub>PM</sub>) and lipid nanodiscs (BR<sub>ND</sub>).** (A) and (B) are cartoons of BR trimers embedded in purple membrane (BR<sub>PM</sub>) and in a lipid nanodisc (BR<sub>ND</sub>), respectively. After attachment of the AFM tip to the C-terminal end of a single BR molecule, the AFM tip is withdrawn to apply mechanical stress to the membrane protein. A force-distance (F-D) curve records the deflection of the AFM cantilever as a function of the distance (d) between AFM tip and membrane (**Figure 4.4A,B**). F-D curves recorded of BR<sub>PM</sub> and BR<sub>ND</sub> show that sufficiently high mechanical stress induces stepwise unfolding of the membrane protein.

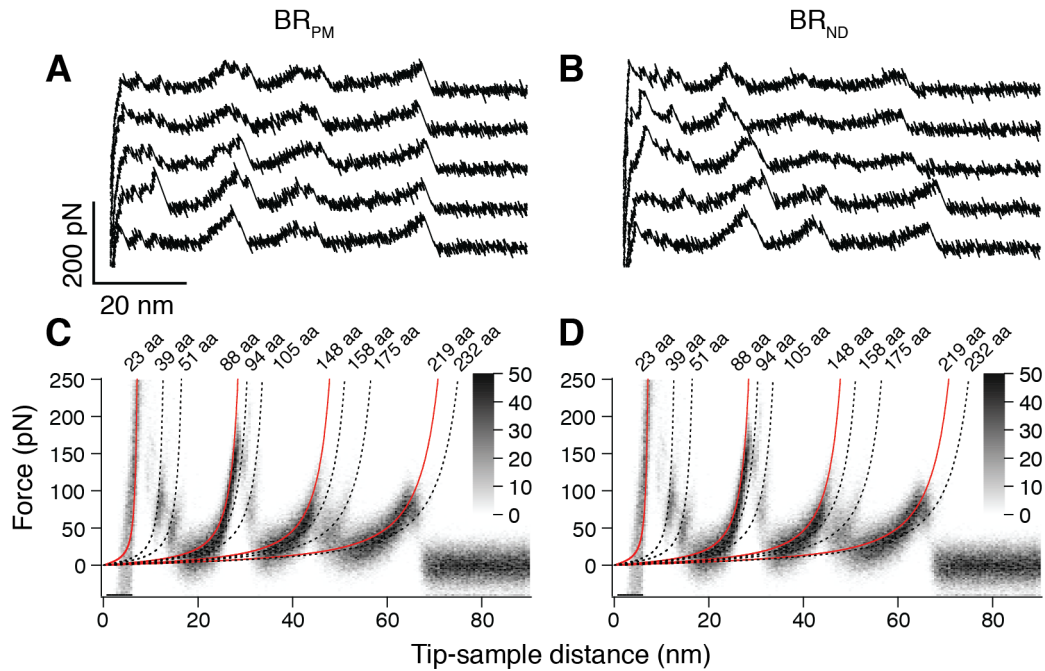


**Figure 4.4: Mechanical unfolding of bacteriorhodopsin in native purple membrane and in lipid nanodiscs.** (A,B) Selection of F-D curves that record the unfolding of single BR<sub>PM</sub> (A) and BR<sub>ND</sub> (B) molecules. Every force peak of every F-D curve detects an unfolding intermediate of BR with all force peaks (unfolding intermediates) describing the unfolding pathway taken by an individual BR molecule. (C,D) Superimpositions of 100 F-D curves recorded for BR<sub>PM</sub> (C) and for BR<sub>ND</sub> (D). Red lines are WLC curves fitting the main force peaks that occur at a probability of 100%, whereas black dashed lines are WLC fits of minor force peaks that occur at probability <80%. The numbers next to each WLC curve assign the contour length (given in amino acids (aa) for every fit) of a force peak. This contour length approximates the length of the unfolded and stretched polypeptide. Gray scale bars allow evaluating how frequently individual force peaks were populated.

In the experiments shown here, BR molecules could either attach unspecifically *via* the N-terminal or the C-terminal end to the AFM tip (Methods). As reported earlier the F-D curves showed a specific pattern depending from which terminal end BR was unfolded (296). However, the probability of the N-terminal end to attach to the AFM-tip was much lower than that of the C-terminal end (156, 296). Thus, for statistical reasons only F-D curves that reflected the unfolding of BR from the C-terminal end were analyzed. The mechanical unfolding of BR from the C-terminal end can be described as follows (156, 159). Upon separating the AFM tip from the support, the C-terminal end of the BR molecule is

stretched and a force builds up. As soon as the stretching force overcomes the stability of BR a structural segment directly connected to the C-terminal end unfolds. This unfolding step extends the polypeptide linking the pulling AFM tip and the portion of the BR molecule that remains folded and anchored in the membrane. Continuously withdrawing the AFM tip stretches the previously unfolded polypeptide until the forthcoming structural segment is loaded, mechanically stressed and unfolded. The unfolding of structural segments forming stably folded entities continues until the entire BR molecule has been unfolded. This scenario explains that every single force peak of a F-D curve detects an unfolding intermediate of BR. The combination of all unfolding intermediates describes the unfolding pathway taken by the BR molecule.

#### **4.3.2 BR in purple membrane and in nanodiscs choose identical unfolding intermediates**

Using SMFS single BR molecules that were embedded either in native purple membrane or in lipid nanodiscs were repeatedly unfolded under identical experimental conditions (**Figure 4.4A,B**; Methods). Every force peak of every F-D curve records an unfolding intermediate of BR that had certain probabilities to be detected (136, 159, 232). An unfolding step describes the transition of one unfolding intermediate into the forthcoming one. Within such an unfolding step a structural segment of the BR molecule unfolds. The amplitude of a force peak quantifies the strength of the interaction that stabilizes a structural segment against unfolding. To visualize the common unfolding intermediates and steps of BR 100 F-D curves recorded of BR<sub>PM</sub> (**Figure 4.4C**) and 100 F-D curves recorded of BR<sub>ND</sub> were superimposed (**Figure 4.4D**). Both superimpositions enhanced the force peaks that were common among all F-D curves (159). The superimpositions of F-D curves recorded of BR<sub>PM</sub> and of BR<sub>ND</sub> did not show any considerable differences.

To fit every force peak and to approximate the contour length of the stretched and unfolded BR polypeptide, the WLC model was used (**Figure 4.4C,D**). After having repeated this procedure for every force

peak of every F-D curve the positions of all force peaks detected were statistically analyzed (**Figure 4.5A,B**). Histograms of the force peak positions detected for the unfolding of BR<sub>PM</sub> and BR<sub>ND</sub> showed minor differences. Student's *t*-tests revealed that none of these differences was statistically significant (**Table 4.1**). This suggests that the unfolding intermediates that were assigned by the force peaks did not differ from both preparations. Thus, it can be concluded that the stable structural segments forming the unfolding intermediates of BR did not depend on whether the membrane protein was embedded in the native purple membrane or in lipid nanodiscs.

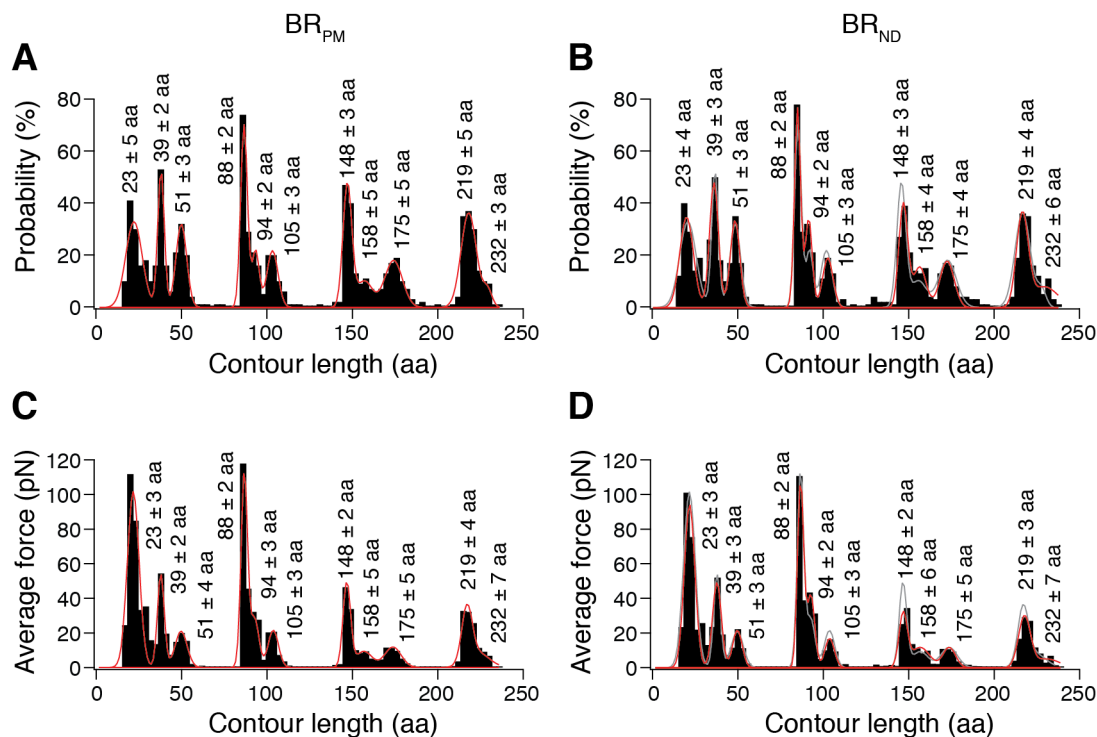


**Figure 4.5: Probability and average force of unfolding intermediates of bacteriorhodopsin in native purple membrane (BR<sub>PM</sub>) and of bacteriorhodopsin reconstituted in lipid nanodiscs (BR<sub>ND</sub>).** (A,B) Probability of force peaks detected at certain contour lengths of BR<sub>PM</sub> (A) and BR<sub>ND</sub> (B). (C,D) Average force of force peaks detected at certain contour lengths of BR<sub>PM</sub> (A) and BR<sub>ND</sub> (B). The contour length of every force peak of every F-D curve ( $n=100$  for each BR<sub>PM</sub> and BR<sub>ND</sub>) was determined by WLC fits (Figure 4.4). Gaussian functions (red lines) were fitted to histograms to determine the average contour length of every peak including the standard deviation (fitted contour lengths in aa are given for every peak). Gray lines in (B) and (D) are Gaussian fits of the BR<sub>PM</sub> reference data (A) and (C), respectively. Bin sizes of histograms were 3 aa. Student's  $t$ -tests did not reveal significant changes between BR<sub>PM</sub> and BR<sub>ND</sub> (Table 4.1).

**Table 4.1: Unfolding intermediates and force peak probability of BR<sub>PM</sub> and BR<sub>ND</sub>.** Values given are averages and standard deviations (Figure 4.5). *p*-values give the statistical difference in the force peak positions and average forces of BR<sub>PM</sub> and BR<sub>ND</sub> as determined by Student's *t*-tests. *p*-values <0.01 are considered significant.

Unfolding intermediate	Localization of intermediate from N-terminal end (aa)	Position of force peak (aa)		<i>p</i> -value		Average force (pN)		<i>p</i> -value		Probability (%)	
		BR <sub>PM</sub>	BR <sub>ND</sub>	BR <sub>PM</sub>	BR <sub>ND</sub>	BR <sub>PM</sub>	BR <sub>ND</sub>	BR <sub>PM</sub>	BR <sub>ND</sub>	BR <sub>PM</sub>	BR <sub>ND</sub>
1	225	23 ± 5	23 ± 4	0.920		102 ± 28	94 ± 22	0.052		100	100
2	198	39 ± 2	39 ± 3	0.706		54 ± 15	49 ± 13	0.505		75	79
3	189	51 ± 3	51 ± 3	0.850		21 ± 7	22 ± 6	0.310		76	70
4	159	88 ± 2	88 ± 2	0.413		112 ± 18	105 ± 16	0.310		100	100
5	144	94 ± 2	94 ± 2	0.613		31 ± 5	42 ± 4	0.208		57	67
6	129	105 ± 3	105 ± 3	0.131		21 ± 3	16 ± 3	0.185		50	44
7	101	148 ± 3	148 ± 3	0.726		49 ± 4	33 ± 4	0.865		100	100
8	79	158 ± 5	158 ± 4	0.071		9 ± 3	12 ± 3	0.062		34	40
9	63	175 ± 5	175 ± 4	0.221		12 ± 3	12 ± 2	0.602		73	67
10	30	219 ± 5	219 ± 4	0.941		37 ± 5	30 ± 5	0.116		100	100
11	17	232 ± 3	232 ± 6	0.063		7 ± 3	5 ± 3	0.058		100	52

To assign the stable structural segments that established unfolding intermediates of the BR structure (**Figure 4.6**, **Figure 4.7**) the average contour lengths were used. The contour length of every unfolding force peak (**Figure 4.5**) was used to assign the beginning of a stable structural segment and the end of the previously unfolded structural segment (159). The stable structural segments detected for both BR<sub>PM</sub> and BR<sub>ND</sub> were similar to the segments repeatedly detected before, using native purple membrane (126, 136, 253). This demonstrates that the unfolding intermediates shaping the unfolding pathway of BR in native purple membrane did not change upon reconstitution of BR into nanodiscs (**Figure 4.7**).

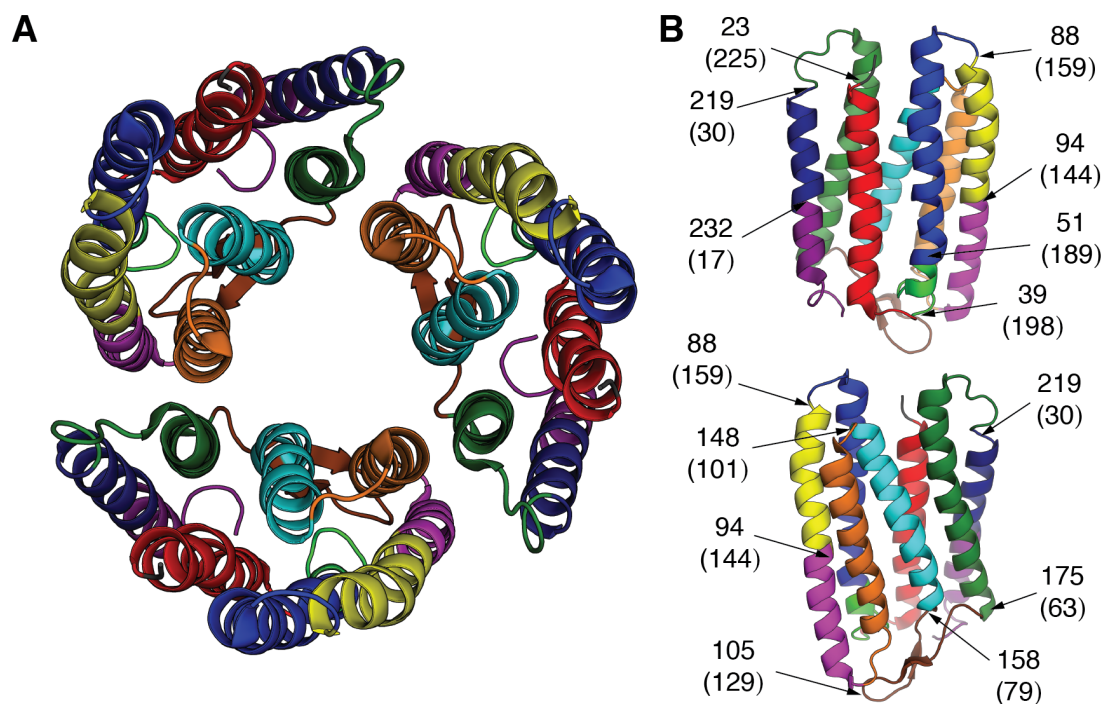


**Figure 4.6: Stable structural segments that establish unfolding intermediates of bacteriorhodopsin.** (A) Top view of the BR trimer from the cytoplasmic surface. (B) Side view of the BR monomer. Numbers without brackets indicate the structural position (in aa) at which a force peak assigned the end of one stable structural segment and the beginning of the forthcoming structural segment. Numbers in brackets denote the corresponding residue (in aa) in the BR sequence (PDB ID 1FFB). Individual structural segments are equally colored.

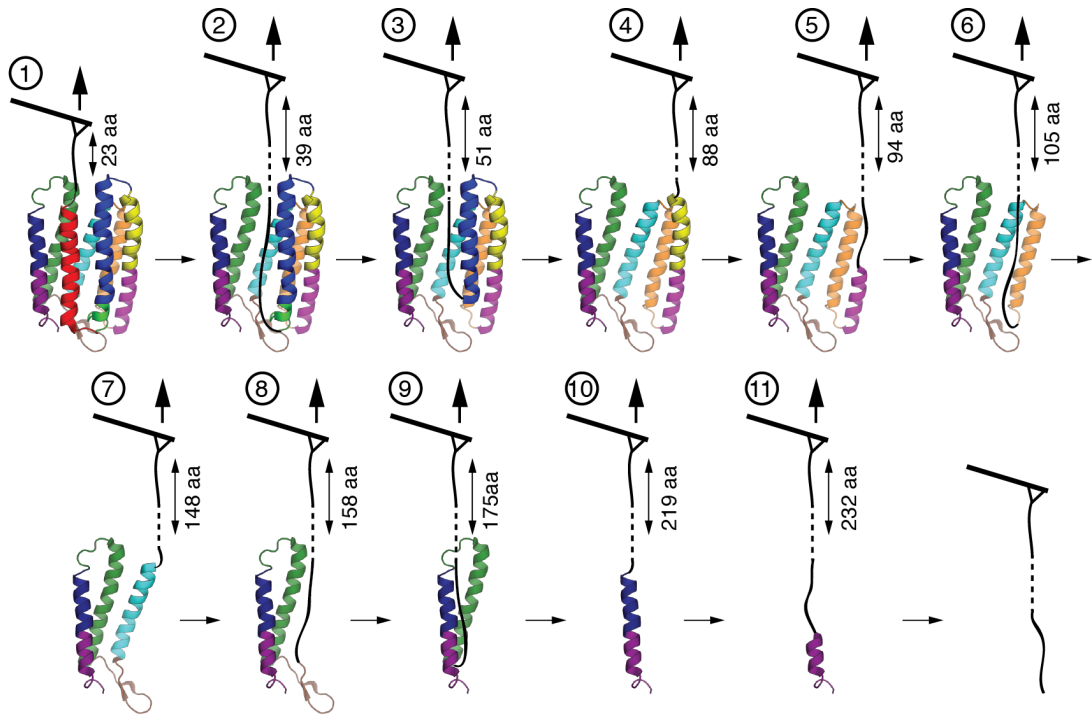


**Figure 4.7: Unfolding intermediates of BR.** After attaching the AFM tip to the C-terminal end the retracting AFM cantilever induces the mechanical unfolding of the BR molecule. In a first step the C-terminal end is stretched (unfolding intermediate 1). At sufficiently high force the first unfolding step occurs and transfers unfolding intermediate 1 into the unfolding intermediate 2. Within this unfolding step the structural segment highlighted in red unfolds. Subsequent retraction of the cantilever stepwise unfolds the BR molecule and stretches the unfolded polypeptide (unfolding intermediates 2-10). In the last unfolding step the remainder of the BR molecule is extracted from the membrane. The sequence of unfolding steps describes transition of one unfolding intermediate into the next one. The sequence of all unfolding intermediates describes the unfolding pathway taken by the BR molecule. As shown in **Table 4.1** every unfolding intermediate of BR had a certain probability to occur. In some cases, one or more unfolding intermediates unfolded collectively in one unfolding step.

Next the average force of every unfolding force peak detected was determined (**Figure 4.5C,D**). Histograms of the average unfolding forces showed minor differences between  $BR_{PM}$  and  $BR_{ND}$ , which were statistically not significant (**Table 4.1**). Because the average unfolding forces quantify the strength of interactions stabilizing the unfolding intermediates of BR, this comparison shows that the interactions established in BR did not depend on whether BR was embedded in the native purple membrane or in lipid nanodiscs. However, it cannot be

excluded that more sensitive SMFS measurements in the future may allow detecting subtle differences.

### **4.3.3 BR<sub>PM</sub> and BR<sub>ND</sub> populate unfolding intermediates similarly**

In the previous chapter it was analyzed whether BR in native purple membrane and BR reconstituted in lipid nanodiscs show different unfolding intermediates and whether there is a difference in the interaction strengths stabilizing the individual unfolding intermediates. None of these analyses revealed significant differences. However, every unfolding intermediate occurred at a certain probability and the sequence of unfolding intermediates describes a particular unfolding pathway taken by the BR molecule. To characterize whether BR in purple membrane and BR in lipid nanodiscs populate unfolding intermediates and pathways differently, the probability for every unfolding intermediate that has been reproducibly taken by BR was analyzed (**Figure 4.7, Table 4.1**). The probability of every unfolding intermediate was obtained from the histogram providing the probability of single unfolding force peaks to be detected (**Figure 4.4A,B**). To determine the probability of a force peak described by a Gaussian distribution the number of F-D curves contributing a force peak to this distribution was counted and divided through the total number of F-D curves (**Table 4.1**).

The unfolding intermediates described by the unfolding force peaks at contour lengths of 23, 88, 148 and 219 aa were detected at a probability of 100%. Therefore, they were named main unfolding intermediates. Other unfolding intermediates of BR were detected at lower probability, and were named minor unfolding intermediates. Thus, stressed at sufficiently high mechanical force the BR molecule always took the same main unfolding intermediates, whereas the minor unfolding intermediates were taken less frequently along the unfolding pathway. The probability of the less frequently occurring unfolding intermediates of BR<sub>ND</sub> showed differences compared to those of BR<sub>PM</sub> (**Table 4.1**). However, these differences and the number of F-D curves analyzed were too small to verify significance (300).

From these results, it can be concluded that, compared to BR of native purple membrane, the reconstitution into lipid nanodiscs did not cause BR to populate unfolding intermediates differently. To further investigate whether there is a difference in the minor unfolding intermediates of BR more sensitive SMFS methods need to be established.

#### **4.3.4 Limited binding probability of the C-terminal end**

The probability to attach the C-terminal end of a BR molecule from purple membrane to the AFM tip was about 10 times higher (0.5%) compared to the probability of attaching the C-terminal end of a BR molecule in lipid nanodiscs (0.05%). Therefore, 10 times more experiments had to be conducted to obtain the 100 F-D curves from BR<sub>ND</sub> in order to superimpose and analyze them in this work (**Figure 4.4**, **Figure 4.5**). Revealing statistical relevant number of F-D curves is mandatory to establish SMFS and dynamic force spectroscopy (DFS) assays to characterize membrane proteins (126, 135, 136, 229, 231, 253). Thus, the low attachment rate of BR from nanodiscs to the AFM tip makes it challenging to obtain sufficient amounts of F-D curves. Several scenarios appear feasible to increase the number of F-D curves recorded from nanodiscs. Most probably the nanodisc preparation characterized for the measurements also contained empty lipid nanodiscs without inserted BR. To overcome this problem, recombinant BR with an affinity tag could be used to separate in a further purification step empty nanodiscs from BR<sub>ND</sub>. Furthermore, it is conceivable that in the preparation used in this work the nanodiscs adsorb onto the support with random orientation (**Figure 4.2**). Therefore, the functionalization of the support to favor a certain orientation of nanodiscs may increase the probability of the AFM tip to attach the terminal end of the membrane protein. Preferentially orienting nanodiscs may also help to reveal AFM topographs that show a sufficient high resolution to identify single BR molecules in the nanodisc. In addition, elongating one of the terminal ends of the membrane protein may be helpful to improve the attachment rate to the AFM tip.

#### 4.4 Summary

In previous SMFS experiments it was investigated whether temperature, mutations, ions, oligomeric assembly, activation, or molecular compounds modify or establish interactions that initiate the formation of new (un-)folding intermediates of membrane proteins embedded in their native lipid membrane (126, 129-133, 136). So far none of these experiments detected that a membrane protein establishes a new unfolding intermediate or stable structural segment. These results suggest that the unfolding intermediates and thus the stable structural segments established within functional membrane proteins are conserved (135, 233). However, when changing external and internal factors modulating the functional state and stability of a membrane protein it was observed that they could significantly change the probability of detecting certain unfolding intermediates by SMFS (127, 130-133). In most of these examples the probability to detect an unfolding intermediate increased with the strength of the interaction stabilizing a particular structural segment. Thus, the interactions stabilizing structural segments within membrane proteins depend sensitively on the environment.

In the SMFS experiments presented here no significant changes of the interaction strengths stabilizing structural segments (unfolding intermediates) of BR embedded in purple membrane and of BR embedded in lipid nanodiscs (**Figure 4.5, Table 4.1**) were detected. To some extent this finding may be considered surprising because the assembly of BR in purple membrane is quite different from BR in lipid nanodiscs (**Figure 4.3**). Additionally, although the phospholipid nanodiscs may contain residual lipids that have been co-extracted with BR from purple membrane, the overall lipid composition of nanodiscs certainly differs from the lipid composition surrounding BR in the native purple membrane. However, as the UV/vis absorption spectra of BR is sensitive to functional alterations (297) the largely unchanged absorption spectra suggests that the native structure and function relationship of BR was

maintained upon reconstitution into phospholipid nanodiscs (**Figure 4.1A**). Because the functional characterization of BR<sub>PM</sub> and BR<sub>ND</sub> reveals no significant differences one may infer that the inter- and intramolecular interactions within BR change very little. From this perspective it is not surprising that the SMFS experiments did not detect significant changes of interactions established of BR<sub>PM</sub> and BR<sub>ND</sub>. Biochemical and biophysical studies showed that BR molecules natively assembled into the BR trimer are structurally and thermally more stable compared to monomeric BR molecules (136, 301, 302). Thus it can be assumed, that the individual BR molecule is significantly stabilized by intermolecular interactions formed within the native BR trimer. In the experiments the BR trimer was reconstituted into lipid nanodiscs (**Figure 4.1B**) without observing significant changes of the folding, stability and the interactions established in BR molecules. To which extend this effect may be attributed to the interactions stabilizing BR molecules within the BR trimer has to be shown. Although in the experiments the modified lipid environment of the nanodisc showed negligible influence on the function and stability of BR this may not be generalized for other membrane proteins. Particularly it has been shown that the lipid composition of membranes can functionally modulate membrane proteins (13, 14, 62, 303). Therefore, it may be too farfetched to conclude from the results that lipid nanodiscs do not change interactions of membrane proteins in general. It may be more realistic to conclude that SMFS of native membrane proteins can be conducted from lipid membranes and from lipid nanodiscs, and that the composition of lipid nanodiscs must be chosen carefully to maintain the native stability, structure and function of a particular membrane protein.

In the experiments presented here no significant changes of the interactions determining the BR stability, unfolding intermediates, and unfolding pathways could be detected. Therefore it can be concluded that membrane proteins can be reconstituted into lipid nanodiscs to study their stability and folding using single molecule techniques such as SMFS. One advantage of using nanodiscs to study membrane proteins by

SMFS is that the reconstitution can be adjusted to the specific conditions required to maintain the native structure and function relationship of the membrane protein. The main advantage of this approach is that membrane proteins reconstituted into nanodiscs can be handled at similar ease as water-soluble proteins. Most importantly, membrane proteins in nanodiscs can be prepared for SMFS and investigated by SMFS similar to water-soluble proteins. Consequently, high-resolution AFM imaging to localize protein membranes is not required anymore for SMFS. This will enable performing high-throughput SMFS of membrane proteins in nanodiscs that homogeneously cover the SMFS support. Such high-throughput SMFS may allow screening for ligands or drugs that bind to the membrane protein of interest, for example to molecular transporters or G protein-coupled receptors (see section 3.1.1) (127, 130, 132, 133). Furthermore, membrane proteins might be sandwiched into polyprotein constructs (304) and characterized with advanced SMFS approaches that have been developed and established using water-soluble proteins. Such approaches include using instrumentations that have been developed to significantly improve force sensitivity (305, 306), time resolution (307), throughput (285, 308, 309) and thermal stability (drift) (310) of the SMFS experiment and that are less well suitable for high-resolution AFM imaging of biological samples. Taken together lipid nanodiscs will open new doors for the characterization of membrane proteins by SMFS.

## 5 Outlook

After its invention in 1986 (90), AFM has emerged into an important tool for the investigation of both biological and non-biological specimen. AFM is constantly improved in terms of instrumentation, but also as a result of novel assays developed to address scientific questions.

Although it has been invented to image surfaces, during the last 20 years the AFM has been increasingly used to measure forces, for instance adhesion forces between individual ligand-receptor pairs (151, 311), cell adhesion (312), stretching of DNA (313) and polymers (314) and of course unfolding of (membrane) proteins (152, 156). All of these experiments had in common that they measured interactions in relation to the function of the investigated sample. Furthermore, these SMFS experiments measured the unfolding behavior of single molecules, in contrast to conventional chemical or biophysical denaturation and unfolding studies, which mainly address bulk properties of a large ensemble of molecules.

It has been shown that SMFS is a valuable tool for investigating unfolding behavior and interactions stabilizing membrane proteins. Furthermore, SMFS-based DFS facilitates the characterization of the underlying energy landscape of the membrane protein. The application of SMFS and DFS made it possible to reveal functionally related changes within membrane proteins (125).

Recently, attempts have been made to study the refolding of membrane proteins into lipid bilayers (138, 139, 315). However, these refolding experiments were based on unfolding experiments where at least one structural element remained anchored in the membrane. Thus, the mechanical refolding of the membrane protein did not reflect a native scenario. Covalently linking the membrane protein of interest to the AFM tip and studying its refolding into an unsupported lipid bilayer might open a new door for the investigation of membrane protein folding on a single-molecule level (92). The target membrane could be supplemented with protein refolding machineries that are known to assist proper

membrane protein folding *in vivo*, like the Sec- (316) or the BAM-complex (317). Additionally, the influence of chaperones on the refolding of membrane proteins could be investigated.

In contrast to soluble proteins, which mainly unfold in a single step, membrane proteins are stabilized by a multitude of molecular interactions. However, unfolding spectra detect only a small subset of these interactions, which can be considered to be the prominent ones. In the future, high-resolution SMFS using ultrastable AFM setups will enable measurements that are sensitive enough to detect even minor interactions of membrane proteins (305, 306, 310). Combined with other techniques, as for example nanodiscs (318) (see chapter 4), SMFS might become an even more powerful tool to investigate the unfolding of membrane proteins *in vitro*.

In order to understand how membrane proteins are controlled *in vivo* and to gain insight into cellular processes, SMFS needs to be transferred into living cells. This paradigm change of combining *in vitro* and *in vivo* SMFS is challenging (300). Nevertheless, such *in vivo* SMFS measurements will provide key insight into biomolecular interactions that drive the machinery in the highly complex and dynamic environment of the cell interior.

---

## 6 Appendix

### 6.1 Abbreviations

°C	Degree Celsius
2D	Two-dimensional
3D	Three-dimensional
Å	Ångström ( $10^{-10}$ m)
aa	Amino acids
AFM	Atomic force microscope/microscopy
BR	Bacteriorhodopsin
BR <sub>ND</sub>	Bacteriorhodopsin in nanodiscs
BR <sub>PM</sub>	Bacteriorhodopsin in purple membrane
CD	Circular dichroism
CHS	Cholesteryl hemisuccinate
DFS	Dynamic force spectroscopy
DMPC	Dimyristoylphosphatidylcholine
DOPC	1,2-dioleoyl-sn-glycero-3-phosphocholine
EM	Electron microscopy
F-D curve	Force-distance curve
G protein	Guanine nucleotide binding protein
G <sub>i</sub>	Inhibiting G protein
GPCR	G protein-coupled receptor
G <sub>s</sub>	Stimulating G protein
h	Hour
HOPG	Highly ordered pyrolytic graphite
IG	Immunoglobulin
IMAC	Immobilized metal ion affinity chromatography
IPTG	Isopropyl- $\beta$ -D-thiogalactopyranosid
J	Joule
min	Minute
mM	Millimolar ( $10^{-3}$ mol/l)
MSP	Membrane scaffold protein

nm	Nanometer ( $10^{-6}$ m)
NMR	Nuclear magnetic resonance
nN	Nanonewton ( $10^{-9}$ N)
OD	Optical density
PC	Phosphatidylcholine
PDB	Protein Data Bank
PE	Phosphatidylethanolamine
PMSF	Phenylmethanesulfonylfluoride
pN	Piconewton ( $10^{-12}$ N)
PS	Phosphatidylserine
PSPD	Position sensitive photodiode
rHDL	Reconstituted high density lipoprotein
s	Second
SD	Standard deviation
Sf9	<i>Spodoptera frugiperda</i>
SM	Sphingomyelin
SMFS	Single-molecule force spectroscopy
SPM	Scanning probe microscope/microscopy
STM	Scanning tunneling microscope
TEV	Tobacco etch virus
TRIS	2-Amino-2-(hydroxymethyl)-1,3-propanediol
WLC	Worm-like chain
$\beta$ -OG	<i>n</i> -octyl- $\beta$ -D-glucopyranoside
$\beta_2$ AR	Human $\beta_2$ adrenergic receptor
$\mu$ m	Micrometer ( $10^{-6}$ m)

## 6.2 Symbols

$F^*$	Most probable rupture/unfolding force [N]
$k_0$	Unfolding rate in absence of force [ $s^{-1}$ ]
$k_B$	Boltzmann constant ( $1.38 \cdot 10^{-23}$ J/K)
$K_d$	Dissociation constant
$L_c$	Contour length [m]
$l_p$	Persistence length [m]

---

$r_f^*$	Most probable loading rage [N/s]
$r_f$	Loading rate [N/s]
$x_u$	Distance between native and transition state [m]
$\kappa_{spacer}$	Spring constant of the polymeric handle connecting cantilever tip and molecule ( <i>e.g.</i> already unfolded polypeptide chain) [N/m]
$\tau_D$	Diffuse relaxation time [s]
$\Delta G_0^\ddagger$	Free energy of activation [J]
$E$	Young's modulus [N/m <sup>2</sup> ]
$F$	Force [N]
$k$	Spring constant [N/m]
$Q$	Quality factor
$T$	Temperature [K]
$\kappa$	Mechanical rigidity of a structural segment [N/m]

### 6.3 Acknowledgements

My PhD thesis involved the work and support of several people. I would like to express my gratitude to those, who made it possible: my PhD advisors Prof. Andreas Engel and Prof. Daniel Müller. I have learnt the most important thing in science: working hard through a project, finishing the project and publishing its results. Thus, I have learnt how to prepare professional illustrations and to write a concise and clear scientific story. I really enjoyed the opportunity, to move to Switzerland and become a fellow member of the Marie Curie Initial Training Network.

I would like to thank all past and present members of Prof. Daniel Müller's research group for their continuous support. In particular, I am very thankful to Christian Bippes, who introduced me to the atomic force microscope. Christian was an extremely helpful colleague throughout my PhD project. Whenever I ran into trouble with the AFM or data analysis, he was the one who knew the solution. I also had nice discussions with Susanne Wegmann, Patrick Bosshart and Jonne Helenius, from which I learnt a lot.

Furthermore, I would like to thank Brian Kobilka and his co-workers. Without this collaboration, the extensive  $\beta_2$ AR project would not have been possible. I would also like to thank Volker Dötsch and his co-workers, especially Frank Bernhard and Christian Roos, who were involved in the nanodisc-project.

Above all, I am very grateful to my parents, Monika and Matthias Zocher, for their support and encouragement to successfully finish my PhD thesis.

Finally, I would like to thank Frederic Bertels for carefully reading my thesis manuscript.

---

## 7 Bibliography

1. Alberts, B., A. Johnson, J. Lewis, M. Raff, K. Roberts, and P. Walter (2007). *Molecular Biology of the Cell*. Edition 5. Garland Science.
2. Voet, D., and G. V. Voet (2010). *Biochemistry*. Edition 4. Wiley.
3. van Meer, G., D. R. Voelker, and G. W. Feigenson (2008). Membrane lipids: where they are and how they behave. *Nat. Rev. Mol. Cell Biol.* **9**:112-124.
4. Rothman, J. E., and J. Lenard (1977). Membrane asymmetry. *Science* **195**:743-753.
5. Zachowski, A. (1993). Phospholipids in animal eukaryotic membranes: transverse asymmetry and movement. *Biochem. J.* **294 (Pt. 1)**:1-14.
6. Heijne, G. (1986). The distribution of positively charged residues in bacterial inner membrane proteins correlates with the trans-membrane topology. *EMBO J.* **5**:3021-3027.
7. von Heijne, G., and Y. Gavel (1988). Topogenic signals in integral membrane proteins. *Eur. J. Biochem.* **174**:671-678.
8. Gavel, Y., J. Steppuhn, R. Herrmann, and G. von Heijne (1991). The 'positive-inside rule' applies to thylakoid membrane proteins. *FEBS Lett.* **282**:41-46.
9. Gavel, Y., and G. von Heijne (1992). The distribution of charged amino acids in mitochondrial inner-membrane proteins suggests different modes of membrane integration for nuclearly and mitochondrially encoded proteins. *Eur. J. Biochem.* **205**:1207-1215.
10. Leever, S. J., B. Vanhaesebroeck, and M. D. Waterfield (1999). Signalling through phosphoinositide 3-kinases: the lipids take centre stage. *Curr. Opin. Cell Biol.* **11**:219-225.
11. Steinberg, S. F. (2008). Structural basis of protein kinase C isoform function. *Physiol. Rev.* **88**:1341-1378.
12. Bogdanov, M., E. Mileykovskaya, and W. Dowhan (2008). Lipids in the assembly of membrane proteins and organization of protein supercomplexes: implications for lipid-linked disorders. *Subcell. Biochem.* **49**:197-239.
13. Opekarova, M., and W. Tanner (2003). Specific lipid requirements of membrane proteins--a putative bottleneck in heterologous expression. *Biochim. Biophys. Acta* **1610**:11-22.
14. Lee, A. G. (2004). How lipids affect the activities of integral membrane proteins. *Biochim. Biophys. Acta* **1666**:62-87.
15. Singer, S. J., and G. L. Nicolson (1972). The fluid mosaic model of the structure of cell membranes. *Science* **175**:720-731.
16. Engelman, D. M. (2005). Membranes are more mosaic than fluid. *Nature* **438**:578-580.
17. Kusumi, A., C. Nakada, K. Ritchie, K. Murase, K. Suzuki, H. Murakoshi, R. S. Kasai, J. Kondo, and T. Fujiwara (2005). Paradigm shift of the plasma

- membrane concept from the two-dimensional continuum fluid to the partitioned fluid: high-speed single-molecule tracking of membrane molecules. *Annu. Rev. Biophys. Biomol. Struct.* **34**:351-378.
18. Schagger, H., and K. Pfeiffer (2000). Supercomplexes in the respiratory chains of yeast and mammalian mitochondria. *EMBO J.* **19**:1777-1783.
  19. Dekker, J. P., and E. J. Boekema (2005). Supramolecular organization of thylakoid membrane proteins in green plants. *Biochim. Biophys. Acta* **1706**:12-39.
  20. Wallin, E., and G. von Heijne (1998). Genome-wide analysis of integral membrane proteins from eubacterial, archaean, and eukaryotic organisms. *Protein Sci.* **7**:1029-1038.
  21. Pestourie, C., L. Cerchia, K. Gombert, Y. Aissouni, J. Boulay, V. De Franciscis, D. Libri, B. Tavitian, and F. Duconge (2006). Comparison of different strategies to select aptamers against a transmembrane protein target. *Oligonucleotides* **16**:323-335.
  22. Yildirim, M. A., K. I. Goh, M. E. Cusick, A. L. Barabasi, and M. Vidal (2007). Drug-target network. *Nat. Biotechnol.* **25**:1119-1126.
  23. Sanders, C. R., and J. K. Nagy (2000). Misfolding of membrane proteins in health and disease: the lady or the tiger? *Curr. Opin. Struct. Biol.* **10**:438-442.
  24. Sanders, C. R., and J. K. Myers (2004). Disease-related misassembly of membrane proteins. *Annu. Rev. Biophys. Biomol. Struct.* **33**:25-51.
  25. Berman, H. M., J. Westbrook, Z. Feng, G. Gilliland, T. N. Bhat, H. Weissig, I. N. Shindyalov, and P. E. Bourne (2000). The Protein Data Bank. *Nucleic Acids Res.* **28**:235-242.
  26. White, S. H. (2004). The progress of membrane protein structure determination. *Protein Sci.* **13**:1948-1949.
  27. Buchanan, S. K. (1999). Beta-barrel proteins from bacterial outer membranes: structure, function and refolding. *Curr. Opin. Struct. Biol.* **9**:455-461.
  28. Koebnik, R., K. P. Locher, and P. Van Gelder (2000). Structure and function of bacterial outer membrane proteins: barrels in a nutshell. *Mol. Microbiol.* **37**:239-253.
  29. Wimley, W. C. (2003). The versatile beta-barrel membrane protein. *Curr. Opin. Struct. Biol.* **13**:404-411.
  30. Tamm, L. K., H. Hong, and B. Liang (2004). Folding and assembly of beta-barrel membrane proteins. *Biochim. Biophys. Acta* **1666**:250-263.
  31. Galdiero, S., M. Galdiero, and C. Pedone (2007). beta-Barrel membrane bacterial proteins: structure, function, assembly and interaction with lipids. *Curr. Prot. Peptide Sci.* **8**:63-82.
  32. Palczewski, K., T. Kumasaka, T. Hori, C. A. Behnke, H. Motoshima, B. A. Fox, I. Le Trong, D. C. Teller, T. Okada, R. E. Stenkamp, M. Yamamoto, and M. Miyano (2000). Crystal structure of rhodopsin: A G protein-coupled receptor. *Science* **289**:739-745.

33. Subbarao, G. V., and B. van den Berg (2006). Crystal structure of the monomeric porin OmpG. *J. Mol. Biol.* **360**:750-759.
34. Van den Berg, B., W. M. Clemons, Jr., I. Collinson, Y. Modis, E. Hartmann, S. C. Harrison, and T. A. Rapoport (2004). X-ray structure of a protein-conducting channel. *Nature* **427**:36-44.
35. White, S. H., and G. von Heijne (2004). The machinery of membrane protein assembly. *Curr. Opin. Struct. Biol.* **14**:397-404.
36. Rapoport, T. A. (2007). Protein translocation across the eukaryotic endoplasmic reticulum and bacterial plasma membranes. *Nature* **450**:663-669.
37. White, S. H. (2007). Membrane protein insertion: the biology-physics nexus. *J. Gen. Physiol.* **129**:363-369.
38. White, S. H., and G. von Heijne (2008). How translocons select transmembrane helices. *Annu. Rev. Biophys.* **37**:23-42.
39. Heinrich, S. U., W. Mothes, J. Brunner, and T. A. Rapoport (2000). The Sec61p complex mediates the integration of a membrane protein by allowing lipid partitioning of the transmembrane domain. *Cell* **102**:233-244.
40. Hessa, T., H. Kim, K. Bihlmaier, C. Lundin, J. Boekel, H. Andersson, I. Nilsson, S. H. White, and G. von Heijne (2005). Recognition of transmembrane helices by the endoplasmic reticulum translocon. *Nature* **433**:377-381.
41. Heinrich, S. U., and T. A. Rapoport (2003). Cooperation of transmembrane segments during the integration of a double-spanning protein into the ER membrane. *EMBO J.* **22**:3654-3663.
42. Sadlish, H., D. Pitonzo, A. E. Johnson, and W. R. Skach (2005). Sequential triage of transmembrane segments by Sec61alpha during biogenesis of a native multispanning membrane protein. *Nat. Struct. Mol. Biol.* **12**:870-878.
43. Popot, J. L., and D. M. Engelman (1990). Membrane protein folding and oligomerization: the two-stage model. *Biochemistry* **29**:4031-4037.
44. Engelman, D. M., Y. Chen, C. N. Chin, A. R. Curran, A. M. Dixon, A. D. Dupuy, A. S. Lee, U. Lehnert, E. E. Matthews, Y. K. Reshetnyak, A. Senes, and J. L. Popot (2003). Membrane protein folding: beyond the two stage model. *FEBS Lett.* **555**:122-125.
45. Anfinsen, C. B. (1973). Principles that govern the folding of protein chains. *Science* **181**:223-230.
46. MacKenzie, K. R., J. H. Prestegard, and D. M. Engelman (1997). A transmembrane helix dimer: structure and implications. *Science* **276**:131-133.
47. Russ, W. P., and D. M. Engelman (2000). The GxxxG motif: a framework for transmembrane helix-helix association. *J. Mol. Biol.* **296**:911-919.
48. Senes, A., M. Gerstein, and D. M. Engelman (2000). Statistical analysis of amino acid patterns in transmembrane helices: the GxxxG motif occurs frequently and in association with beta-branched residues at neighboring positions. *J. Mol. Biol.* **296**:921-936.

49. Hermansson, M., and G. von Heijne (2003). Inter-helical hydrogen bond formation during membrane protein integration into the ER membrane. *J. Mol. Biol.* **334**:803-809.
50. Popot, J. L., and D. M. Engelman (2000). Helical membrane protein folding, stability, and evolution. *Annu. Rev. Biochem.* **69**:881-922.
51. White, S. H., and W. C. Wimley (1999). Membrane protein folding and stability: physical principles. *Annu. Rev. Biophys. Biomol. Struct.* **28**:319-365.
52. Engelman, D. M., and T. A. Steitz (1981). The spontaneous insertion of proteins into and across membranes: the helical hairpin hypothesis. *Cell* **23**:411-422.
53. Jacobs, R. E., and S. H. White (1989). The nature of the hydrophobic binding of small peptides at the bilayer interface: implications for the insertion of transbilayer helices. *Biochemistry* **28**:3421-3437.
54. Milik, M., and J. Skolnick (1993). Insertion of peptide chains into lipid membranes: an off-lattice Monte Carlo dynamics model. *Proteins* **15**:10-25.
55. Becher, B. M., and J. Y. Cassim (1975). Improved isolation procedures for the purple membrane of *Halobacterium halobium*. *Prep. Biochem.* **5**:161-178.
56. Tate, C. G. (2001). Overexpression of mammalian integral membrane proteins for structural studies. *FEBS Lett.* **504**:94-98.
57. Seddon, A. M., P. Curnow, and P. J. Booth (2004). Membrane proteins, lipids and detergents: not just a soap opera. *Biochim. Biophys. Acta* **1666**:105-117.
58. Wagner, S., M. L. Bader, D. Drew, and J. W. de Gier (2006). Rationalizing membrane protein overexpression. *Trends Biotechnol.* **24**:364-371.
59. Otto, J. C., D. L. DeWitt, and W. L. Smith (1993). N-glycosylation of prostaglandin endoperoxide synthases-1 and -2 and their orientations in the endoplasmic reticulum. *J. Biol. Chem.* **268**:18234-18242.
60. Loll, P. J. (2003). Membrane protein structural biology: the high throughput challenge. *J. Struct. Biol.* **142**:144-153.
61. Booth, P. J. (2003). The trials and tribulations of membrane protein folding in vitro. *Biochim. Biophys. Acta* **1610**:51-56.
62. Hunte, C., and S. Richers (2008). Lipids and membrane protein structures. *Curr. Opin. Struct. Biol.* **18**:406-411.
63. Tribet, C., R. Audebert, and J. L. Popot (1996). Amphipols: polymers that keep membrane proteins soluble in aqueous solutions. *Proc. Natl. Acad. Sci. USA* **93**:15047-15050.
64. Luecke, H., B. Schobert, H. T. Richter, J. P. Cartailler, and J. K. Lanyi (1999). Structural changes in bacteriorhodopsin during ion transport at 2 angstrom resolution. *Science* **286**:255-261.
65. Cherezov, V., D. M. Rosenbaum, M. A. Hanson, S. G. Rasmussen, F. S. Thian, T. S. Kobilka, H. J. Choi, P. Kuhn, W. I. Weis, B. K. Kobilka, and R. C. Stevens (2007). High-resolution crystal structure of an engineered human beta2-adrenergic G protein-coupled receptor. *Science* **318**:1258-1265.

- 
66. Rasmussen, S. G., H. J. Choi, D. M. Rosenbaum, T. S. Kobilka, F. S. Thian, P. C. Edwards, M. Burghammer, V. R. Ratnala, R. Sanishvili, R. F. Fischetti, G. F. Schertler, W. I. Weis, and B. K. Kobilka (2007). Crystal structure of the human beta2 adrenergic G-protein-coupled receptor. *Nature* **450**:383-387.
  67. Ruska, E. (1987). Nobel lecture. The development of the electron microscope and of electron microscopy. *Biosci. Rep.* **7**:607-629.
  68. Unwin, P. N., and R. Henderson (1975). Molecular structure determination by electron microscopy of unstained crystalline specimens. *J. Mol. Biol.* **94**:425-440.
  69. Murata, K., K. Mitsuoka, T. Hirai, T. Walz, P. Agre, J. B. Heymann, A. Engel, and Y. Fujiyoshi (2000). Structural determinants of water permeation through aquaporin-1. *Nature* **407**:599-605.
  70. Saibil, H. R. (2000). Macromolecular structure determination by cryo-electron microscopy. *Acta Crystallogr. D Biol. Crystallogr.* **56**:1215-1222.
  71. Frank, J. (2002). Single-particle imaging of macromolecules by cryo-electron microscopy. *Annu. Rev. Biophys. Biomol. Struct.* **31**:303-319.
  72. Klein-Seetharaman, J., P. J. Reeves, M. C. Loewen, E. V. Getmanova, J. Chung, H. Schwalbe, P. E. Wright, and H. G. Khorana (2002). Solution NMR spectroscopy of [ $\alpha$ - $^{15}\text{N}$ ]lysine-labeled rhodopsin: The single peak observed in both conventional and TROSY-type HSQC spectra is ascribed to Lys-339 in the carboxyl-terminal peptide sequence. *Proc. Natl. Acad. Sci. USA* **99**:3452-3457.
  73. Baldus, M. (2007). ICMRBS founder's medal 2006: biological solid-state NMR, methods and applications. *J. Biomol. NMR* **39**:73-86.
  74. Eilers, M., W. Ying, P. J. Reeves, H. G. Khorana, and S. O. Smith (2002). Magic angle spinning nuclear magnetic resonance of isotopically labeled rhodopsin. *Methods Enzymol.* **343**:212-222.
  75. Vogel, H., L. Nilsson, R. Rigler, S. Meder, G. Boheim, W. Beck, H. H. Kurth, and G. Jung (1993). Structural fluctuations between two conformational states of a transmembrane helical peptide are related to its channel-forming properties in planar lipid membranes. *Eur. J. Biochem.* **212**:305-313.
  76. Wallace, B. A., J. G. Lees, A. J. Orry, A. Loble, and R. W. Janes (2003). Analyses of circular dichroism spectra of membrane proteins. *Protein Sci.* **12**:875-884.
  77. Gerwert, K. (1999). Molecular reaction mechanisms of proteins monitored by time-resolved FTIR-spectroscopy. *Biol. Chem.* **380**:931-935.
  78. Wang, J., and M. A. El-Sayed (1999). Temperature jump-induced secondary structural change of the membrane protein bacteriorhodopsin in the premelting temperature region: a nanosecond time-resolved Fourier transform infrared study. *Biophys. J.* **76**:2777-2783.
  79. Sharom, F. J., R. Liu, and Y. Romsicki (1998). Spectroscopic and biophysical approaches for studying the structure and function of the P-glycoprotein multidrug transporter. *Biochem. Cell Biol.* **76**:695-708.
  80. Brouillette, C. G., D. D. Muccio, and T. K. Finney (1987). pH dependence of bacteriorhodopsin thermal unfolding. *Biochemistry* **26**:7431-7438.

81. Edrington, T. C. t., M. Bennett, and A. D. Albert (2008). Calorimetric studies of bovine rod outer segment disk membranes support a monomeric unit for both rhodopsin and opsin. *Biophys. J.* **95**:2859-2866.
82. Bukauskas, F. F., R. Vogel, and R. Weingart (1997). Biophysical properties of heterotypic gap junctions newly formed between two types of insect cells. *J. Physiol.* **499 (Pt. 3)**:701-713.
83. Karpen, J. W., and M. Ruiz (2002). Ion channels: does each subunit do something on its own? *Trends Biochem. Sci.* **27**:402-409.
84. Dunlop, J., M. Bowlby, R. Peri, D. Vasilyev, and R. Arias (2008). High-throughput electrophysiology: an emerging paradigm for ion-channel screening and physiology. *Nat. Rev. Drug Discov.* **7**:358-368.
85. Oliveira, L., T. Hulsén, D. Lutje Hulsik, A. C. Paiva, and G. Vriend (2004). Heavier-than-air flying machines are impossible. *FEBS Lett.* **564**:269-273.
86. Fanelli, F., and P. G. De Benedetti (2005). Computational modeling approaches to structure-function analysis of G protein-coupled receptors. *Chem. Rev.* **105**:3297-3351.
87. Cieplak, M., S. Filipek, H. Janovjak, and K. A. Krzysko (2006). Pulling single bacteriorhodopsin out of a membrane: Comparison of simulation and experiment. *Biochim. Biophys. Acta* **1758**:537-544.
88. Seeber, M., F. Fanelli, E. Paci, and A. Caflisch (2006). Sequential unfolding of individual helices of bacterioopsin observed in molecular dynamics simulations of extraction from the purple membrane. *Biophys. J.* **91**:3276-3284.
89. Binnig, G., H. Rohrer, C. Gerber, and E. Weibel (1982). Tunneling through a Controllable Vacuum Gap. *Appl. Phys. Lett.* **40**:178-180.
90. Binnig, G., C. F. Quate, and C. Gerber (1986). Atomic force microscope. *Phys. Rev. Lett.* **56**:930-933.
91. Giessibl, F. J. (1995). Atomic resolution of the silicon (111)-(7x7) surface by atomic force microscopy. *Science* **267**:68-71.
92. Bippes, C. A., and D. J. Muller (2011). High-resolution atomic force microscopy and spectroscopy of native membrane proteins. *Rep. Prog. Phys.* **74**.
93. Muller, D. J., and A. Engel (2007). Atomic force microscopy and spectroscopy of native membrane proteins. *Nat. Protoc.* **2**:2191-2197.
94. Hoh, J. H., R. Lal, S. A. John, J. P. Revel, and M. F. Arnsdorf (1991). Atomic Force Microscopy and Dissection of Gap-Junctions. *Science* **253**:1405-1408.
95. Schabert, F. A., C. Henn, and A. Engel (1995). Native Escherichia-Coli Ompf Porin Surfaces Probed by Atomic-Force Microscopy. *Science* **268**:92-94.
96. Fotiadis, D., D. J. Muller, G. Tsiotis, L. Hasler, P. Tittmann, T. Mini, P. Jenö, H. Gross, and A. Engel (1998). Surface analysis of the photosystem I complex by electron and atomic force microscopy. *J. Mol. Biol.* **283**:83-94.
97. Muller, D. J., H. J. Sass, S. A. Muller, G. Buldt, and A. Engel (1999). Surface structures of native bacteriorhodopsin depend on the molecular packing arrangement in the membrane. *J. Mol. Biol.* **285**:1903-1909.

98. Scheuring, S., P. Ringler, M. Borgnia, H. Stahlberg, D. J. Muller, P. Agre, and A. Engel (1999). High resolution AFM topographs of the Escherichia coli water channel aquaporin Z. *EMBO J.* **18**:4981-4987.
99. Fotiadis, D., L. Hasler, D. J. Muller, H. Stahlberg, J. Kistler, and A. Engel (2000). Surface tongue-and-groove contours on lens MIP facilitate cell-to-cell adherence. *J. Mol. Biol.* **300**:779-789.
100. Fotiadis, D., K. Suda, P. Tittmann, P. Jenö, A. Philippsen, D. J. Muller, H. Gross, and A. Engel (2002). Identification and structure of a putative Ca<sup>2+</sup>-binding domain at the C terminus of AQP1. *J. Mol. Biol.* **318**:1381-1394.
101. Muller, D. J., G. M. Hand, A. Engel, and G. E. Sosinsky (2002). Conformational changes in surface structures of isolated connexin 26 gap junctions. *EMBO J.* **21**:3598-3607.
102. Scheuring, S., J. Seguin, S. Marco, D. Levy, B. Robert, and J. L. Rigaud (2003). Nanodissection and high-resolution imaging of the Rhodospseudomonas viridis photosynthetic core complex in native membranes by AFM. *Proc. Natl. Acad. Sci. USA* **100**:1690-1693.
103. Yu, J. S., C. A. Bippes, G. M. Hand, D. J. Muller, and G. E. Sosinsky (2007). Aminosulfonate modulated pH-induced conformational changes in connexin26 hemichannels. *J. Biol. Chem.* **282**:8895-8904.
104. Muller, D. J., G. Buldt, and A. Engel (1995). Force-Induced Conformational Change of Bacteriorhodopsin. *J. Mol. Biol.* **249**:239-243.
105. Muller, D. J., W. Baumeister, and A. Engel (1996). Conformational change of the hexagonally packed intermediate layer of Deinococcus radiodurans monitored by atomic force microscopy. *J. Bacteriol.* **178**:3025-3030.
106. Muller, D. J., and A. Engel (1999). Voltage and pH-induced channel closure of porin OmpF visualized by atomic force microscopy. *J. Mol. Biol.* **285**:1347-1351.
107. Mari, S. A., S. Koster, C. A. Bippes, O. Yildiz, W. Kuhlbrandt, and D. J. Muller (2010). pH-Induced Conformational Change of the beta-Barrel-Forming Protein OmpG Reconstituted into Native E. coli Lipids. *J. Mol. Biol.* **396**:610-616.
108. Mari, S. A., J. Pessoa, S. Altieri, U. Hensen, L. Thomas, J. H. Morais-Cabral, and D. J. Muller (2011). Gating of the MlotiK1 potassium channel involves large rearrangements of the cyclic nucleotide-binding domains. *Proc. Natl. Acad. Sci. USA* **108**:20802-20807.
109. Mou, J. X., J. Yang, and Z. F. Shao (1995). Atomic-Force Microscopy of Cholera-Toxin B-Oligomers Bound to Bilayers of Biologically Relevant Lipids. *J. Mol. Biol.* **248**:507-512.
110. Czajkowsky, D. M., S. Sheng, and Z. Shao (1998). Staphylococcal alpha-hemolysin can form hexamers in phospholipid bilayers. *J. Mol. Biol.* **276**:325-330.
111. Seelert, H., A. Poetsch, N. A. Dencher, A. Engel, H. Stahlberg, and D. J. Muller (2000). Structural biology. Proton-powered turbine of a plant motor. *Nature* **405**:418-419.
112. Stahlberg, H., D. J. Muller, K. Suda, D. Fotiadis, A. Engel, T. Meier, U. Matthey, and P. Dimroth (2001). Bacterial Na<sup>(+)</sup>-ATP synthase has an undecameric rotor. *EMBO Rep.* **2**:229-233.

113. Fotiadis, D., Y. Liang, S. Filipek, D. A. Saperstein, A. Engel, and K. Palczewski (2003). Atomic-force microscopy: Rhodopsin dimers in native disc membranes. *Nature* **421**:127-128.
114. Cisneros, D. A., D. Oesterhelt, and D. J. Muller (2005). Probing origins of molecular interactions stabilizing the membrane proteins halorhodopsin and bacteriorhodopsin. *Structure* **13**:235-242.
115. Meier, T., J. Yu, T. Raschle, F. Henzen, P. Dimroth, and D. J. Muller (2005). Structural evidence for a constant c11 ring stoichiometry in the sodium F-ATP synthase. *FEBS J.* **272**:5474-5483.
116. Pogoryelov, D., J. Yu, T. Meier, J. Vonck, P. Dimroth, and D. J. Muller (2005). The c15 ring of the *Spirulina platensis* F-ATP synthase: F1/F0 symmetry mismatch is not obligatory. *EMBO Rep.* **6**:1040-1044.
117. Fotiadis, D., B. Jastrzebska, A. Philippsen, D. J. Muller, K. Palczewski, and A. Engel (2006). Structure of the rhodopsin dimer: a working model for G-protein-coupled receptors. *Curr. Opin. Struct. Biol.* **16**:252-259.
118. Hoogenboom, B. W., K. Suda, A. Engel, and D. Fotiadis (2007). The supramolecular assemblies of voltage-dependent anion channels in the native membrane. *J. Mol. Biol.* **370**:246-255.
119. Pogoryelov, D., C. Reichen, A. L. Klyszejko, R. Brunisholz, D. J. Muller, P. Dimroth, and T. Meier (2007). The oligomeric state of c rings from cyanobacterial F-ATP synthases varies from 13 to 15. *J. Bacteriol.* **189**:5895-5902.
120. Fritz, M., A. L. Klyszejko, N. Morgner, J. Vonck, B. Brutschy, D. J. Muller, T. Meier, and V. Muller (2008). An intermediate step in the evolution of ATPases: a hybrid F(0)-V(0) rotor in a bacterial Na(+) F(1)F(0) ATP synthase. *FEBS J.* **275**:1999-2007.
121. Klyszejko, A. L., S. Shastri, S. A. Mari, H. Grubmuller, D. J. Muller, and C. Glaubitz (2008). Folding and assembly of proteorhodopsin. *J. Mol. Biol.* **376**:35-41.
122. Matthies, D., L. Preiss, A. L. Klyszejko, D. J. Muller, G. M. Cook, J. Vonck, and T. Meier (2009). The c13 ring from a thermoalkaliphilic ATP synthase reveals an extended diameter due to a special structural region. *J. Mol. Biol.* **388**:611-618.
123. Muller, D. J., A. Engel, U. Matthey, T. Meier, P. Dimroth, and K. Suda (2003). Observing membrane protein diffusion at subnanometer resolution. *J. Mol. Biol.* **327**:925-930.
124. Yamashita, H., K. Voitchovsky, T. Uchihashi, S. A. Contera, J. F. Ryan, and T. Ando (2009). Dynamics of bacteriorhodopsin 2D crystal observed by high-speed atomic force microscopy. *J. Struct. Biol.* **167**:153-158.
125. Kedrov, A., H. Janovjak, K. T. Sapro, and D. J. Muller (2007). Deciphering molecular interactions of native membrane proteins by single-molecule force spectroscopy. *Annu. Rev. Biophys. Biomol. Struct.* **36**:233-260.
126. Janovjak, H., M. Kessler, D. Oesterhelt, H. Gaub, and D. J. Muller (2003). Unfolding pathways of native bacteriorhodopsin depend on temperature. *EMBO J.* **22**:5220-5229.

- 
127. Kedrov, A., M. Krieg, C. Ziegler, W. Kuhlbrandt, and D. J. Muller (2005). Locating ligand binding and activation of a single antiporter. *EMBO Rep.* **6**:668-674.
128. Kedrov, A., S. Wegmann, S. H. Smits, P. Goswami, H. Baumann, and D. J. Muller (2007). Detecting molecular interactions that stabilize, activate and guide ligand-binding of the sodium/proton antiporter MjNhaP1 from *Methanococcus jannaschii*. *J. Struct. Biol.* **159**:290-301.
129. Kedrov, A., M. Appel, H. Baumann, C. Ziegler, and D. J. Muller (2008). Examining the dynamic energy landscape of an antiporter upon inhibitor binding. *J. Mol. Biol.* **375**:1258-1266.
130. Bippes, C. A., A. Zeltina, F. Casagrande, M. Ratera, M. Palacin, D. J. Muller, and D. Fotiadis (2009). Substrate binding tunes conformational flexibility and kinetic stability of an amino acid antiporter. *J. Biol. Chem.* **284**:18651-18663.
131. Kedrov, A., A. M. Hellawell, A. Klosin, R. B. Broadhurst, E. R. Kunji, and D. J. Muller (2010). Probing the interactions of carboxy-atractyloside and atractyloside with the yeast mitochondrial ADP/ATP carrier. *Structure* **18**:39-46.
132. Park, P. S., K. T. Sapra, M. Kolinski, S. Filipek, K. Palczewski, and D. J. Muller (2007). Stabilizing effect of Zn<sup>2+</sup> in native bovine rhodopsin. *J. Biol. Chem.* **282**:11377-11385.
133. Ge, L., C. Perez, I. Waclawska, C. Ziegler, and D. J. Muller (2011). Locating an extracellular K<sup>+</sup>-dependent interaction site that modulates betaine-binding of the Na<sup>+</sup>-coupled betaine symporter BetP. *Proc. Natl. Acad. Sci. USA* **108**:E890-898.
134. Kedrov, A., C. Ziegler, and D. J. Muller (2006). Differentiating ligand and inhibitor interactions of a single antiporter. *J. Mol. Biol.* **362**:925-932.
135. Sapra, K. T., G. P. Balasubramanian, D. Labudde, J. U. Bowie, and D. J. Muller (2008). Point mutations in membrane proteins reshape energy landscape and populate different unfolding pathways. *J. Mol. Biol.* **376**:1076-1090.
136. Sapra, K. T., H. Besir, D. Oesterhelt, and D. J. Muller (2006). Characterizing molecular interactions in different bacteriorhodopsin assemblies by single-molecule force spectroscopy. *J. Mol. Biol.* **355**:640-650.
137. Damaghi, M., K. T. Sapra, S. Koster, O. Yildiz, W. Kuhlbrandt, and D. J. Muller (2010). Dual energy landscape: the functional state of the beta-barrel outer membrane protein G molds its unfolding energy landscape. *Proteomics* **10**:4151-4162.
138. Kedrov, A., C. Ziegler, H. Janovjak, W. Kuhlbrandt, and D. J. Muller (2004). Controlled unfolding and refolding of a single sodium-proton antiporter using atomic force microscopy. *J. Mol. Biol.* **340**:1143-1152.
139. Damaghi, M., S. Koster, C. A. Bippes, O. Yildiz, and D. J. Muller (2011). One beta hairpin follows the other: exploring refolding pathways and kinetics of the transmembrane beta-barrel protein OmpG. *Angew. Chem. Int. Ed. Engl.* **50**:7422-7424.
140. Yeh, M. K., B. Y. Chen, N. H. Tai, and C. C. Chiu (2006). Force measurement by AFM cantilever with different coating layers. *Key. Eng. Mat.* **326-328**:377-380.

141. Burnham, N. A., X. Chen, C. S. Hodges, G. A. Matei, E. J. Thoreson, C. J. Roberts, M. C. Davies, and S. J. B. Tendler (2003). Comparison of calibration methods for atomic-force microscopy cantilevers. *Nanotechnology* **14**:1-6.
142. Hutter, J. L., and J. Bechhoefer (1993). Calibration of Atomic-Force Microscope Tips. *Rev. Sci. Instrum.* **64**:3342-3342.
143. Muller, D. J., M. Amrein, and A. Engel (1997). Adsorption of biological molecules to a solid support for scanning probe microscopy. *J. Struct. Biol.* **119**:172-188.
144. Cisneros, D. A., D. J. Muller, S. M. Daud, and J. H. Lakey (2006). An approach to prepare membrane proteins for single-molecule imaging. *Angew. Chem. Int. Ed. Engl.* **45**:3252-3256.
145. Frederix, P. L., P. D. Bosshart, T. Akiyama, M. Chami, M. R. Gullo, J. J. Blackstock, K. Dooleweerd, N. F. de Rooij, U. Staufer, and A. Engel (2008). Conductive supports for combined AFM-SECM on biological membranes. *Nanotechnology* **19**:384004.
146. Karrasch, S., M. Dolder, F. Schabert, J. Ramsden, and A. Engel (1993). Covalent binding of biological samples to solid supports for scanning probe microscopy in buffer solution. *Biophys. J.* **65**:2437-2446.
147. Karrasch, S., R. Hegerl, J. H. Hoh, W. Baumeister, and A. Engel (1994). Atomic force microscopy produces faithful high-resolution images of protein surfaces in an aqueous environment. *Proc. Natl. Acad. Sci. USA* **91**:836-838.
148. Muller, D. J., F. A. Schabert, G. Buldt, and A. Engel (1995). Imaging purple membranes in aqueous solutions at sub-nanometer resolution by atomic force microscopy. *Biophys. J.* **68**:1681-1686.
149. Muller, D. J., and Y. F. Dufrene (2008). Atomic force microscopy as a multifunctional molecular toolbox in nanobiotechnology. *Nat. Nanotechnol.* **3**:261-269.
150. Moy, V. T., E. L. Florin, and H. E. Gaub (1994). Intermolecular forces and energies between ligands and receptors. *Science* **266**:257-259.
151. Lee, G. U., D. A. Kidwell, and R. J. Colton (1994). Sensing Discrete Streptavidin Biotin Interactions with Atomic-Force Microscopy. *Langmuir* **10**:354-357.
152. Rief, M., M. Gautel, F. Oesterhelt, J. M. Fernandez, and H. E. Gaub (1997). Reversible unfolding of individual titin immunoglobulin domains by AFM. *Science* **276**:1109-1112.
153. Smith, M. L., D. Gourdon, W. C. Little, K. E. Kubow, R. A. Eguiluz, S. Luna-Morris, and V. Vogel (2007). Force-induced unfolding of fibronectin in the extracellular matrix of living cells. *PLoS Biol.* **5**:e268.
154. Falb, M., K. Muller, L. Konigsmair, T. Oberwinkler, P. Horn, S. von Gronau, O. Gonzalez, F. Pfeiffer, E. Bornberg-Bauer, and D. Oesterhelt (2008). Metabolism of halophilic archaea. *Extremophiles* **12**:177-196.
155. Ng, W. V., S. P. Kennedy, G. G. Mahairas, B. Berquist, M. Pan, H. D. Shukla, S. R. Lasky, N. S. Baliga, V. Thorsson, J. Sbrogna, S. Swartzell, D. Weir, J. Hall, T. A. Dahl, R. Welti, Y. A. Goo, B. Leithauser, K. Keller, R. Cruz, M. J. Danson, D. W. Hough, D. G. Maddocks, P. E. Jablonski, M. P. Krebs, C. M. Angevine, H. Dale, T. A. Isenbarger, R. F. Peck, M. Pohlschroder, J. L. Spudich, K. W. Jung, M. Alam, T. Freitas, S. Hou, C. J. Daniels, P. P. Dennis, A. D. Omer, H. Eberhardt,

- T. M. Lowe, P. Liang, M. Riley, L. Hood, and S. DasSarma (2000). Genome sequence of Halobacterium species NRC-1. *Proc. Natl. Acad. Sci. USA* **97**:12176-12181.
156. Oesterhelt, F., D. Oesterhelt, M. Pfeiffer, A. Engel, H. E. Gaub, and D. J. Muller (2000). Unfolding pathways of individual bacteriorhodopsins. *Science* **288**:143-146.
157. Luecke, H., B. Schobert, H. T. Richter, J. P. Cartailler, and J. K. Lanyi (1999). Structure of bacteriorhodopsin at 1.55 Å resolution. *J. Mol. Biol.* **291**:899-911.
158. Lanyi, J. K. (2004). Bacteriorhodopsin. *Annu. Rev. Physiol.* **66**:665-688.
159. Muller, D. J., M. Kessler, F. Oesterhelt, C. Moller, D. Oesterhelt, and H. Gaub (2002). Stability of bacteriorhodopsin alpha-helices and loops analyzed by single-molecule force spectroscopy. *Biophys. J.* **83**:3578-3588.
160. Flory, P. J. (1969). *Statistical mechanics of chain molecules* Interscience Publishers, New York.
161. Bustamante, C., J. F. Marko, E. D. Siggia, and S. Smith (1994). Entropic Elasticity of Lambda-Phage DNA. *Science* **265**:1599-1600.
162. Marko, J. F., and E. D. Siggia (1995). Stretching DNA. *Macromolecules* **28**:8759-8770.
163. Bouchiat, C., M. D. Wang, J. Allemand, T. Strick, S. M. Block, and V. Croquette (1999). Estimating the persistence length of a worm-like chain molecule from force-extension measurements. *Biophys. J.* **76**:409-413.
164. Puchner, E. M., and H. E. Gaub (2009). Force and function: probing proteins with AFM-based force spectroscopy. *Curr. Opin. Struct. Biol.* **19**:605-614.
165. Evans, E. (2001). Probing the relation between force--lifetime--and chemistry in single molecular bonds. *Annu. Rev. Biophys. Biomol. Struct.* **30**:105-128.
166. Baldwin, R. L., and G. D. Rose (1999). Is protein folding hierarchic? I. Local structure and peptide folding. *Trends Biochem. Sci.* **24**:26-33.
167. Baldwin, R. L., and G. D. Rose (1999). Is protein folding hierarchic? II. Folding intermediates and transition states. *Trends Biochem. Sci.* **24**:77-83.
168. Bieri, O., J. Wirz, B. Hellrung, M. Schutkowski, M. Drewello, and T. Kiefhaber (1999). The speed limit for protein folding measured by triplet-triplet energy transfer. *Proc. Natl. Acad. Sci. USA* **96**:9597-9601.
169. Krieger, F., B. Fierz, O. Bieri, M. Drewello, and T. Kiefhaber (2003). Dynamics of unfolded polypeptide chains as model for the earliest steps in protein folding. *J. Mol. Biol.* **332**:265-274.
170. Bell, G. I. (1978). Models for the specific adhesion of cells to cells. *Science* **200**:618-627.
171. Evans, E., and K. Ritchie (1997). Dynamic strength of molecular adhesion bonds. *Biophys. J.* **72**:1541-1555.
172. Dill, K. A., S. Bromberg, K. Yue, K. M. Fiebig, D. P. Yee, P. D. Thomas, and H. S. Chan (1995). Principles of protein folding--a perspective from simple exact models. *Protein Sci.* **4**:561-602.

173. Onuchic, J. N., P. G. Wolynes, Z. Luthey-Schulten, and N. D. Socci (1995). Toward an outline of the topography of a realistic protein-folding funnel. *Proc. Natl. Acad. Sci. USA* **92**:3626-3630.
174. Dill, K. A., and H. S. Chan (1997). From Levinthal to pathways to funnels. *Nat. Struct. Biol.* **4**:10-19.
175. Onuchic, J. N., Z. Luthey-Schulten, and P. G. Wolynes (1997). Theory of protein folding: the energy landscape perspective. *Annu. Rev. Phys. Chem.* **48**:545-600.
176. Dill, K. A. (1999). Polymer principles and protein folding. *Protein Sci.* **8**:1166-1180.
177. Evans, E. (1998). Energy landscapes of biomolecular adhesion and receptor anchoring at interfaces explored with dynamic force spectroscopy. *Faraday Discuss.* **111**:1-16.
178. Janovjak, H., H. Knaus, and D. J. Muller (2007). Transmembrane helices have rough energy surfaces. *J. Am. Chem. Soc.* **129**:246-247.
179. Fredriksson, R., M. C. Lagerstrom, L. G. Lundin, and H. B. Schioth (2003). The G-protein-coupled receptors in the human genome form five main families. Phylogenetic analysis, paralogon groups, and fingerprints. *Mol. Pharmacol.* **63**:1256-1272.
180. Rosenbaum, D. M., S. G. Rasmussen, and B. K. Kobilka (2009). The structure and function of G-protein-coupled receptors. *Nature* **459**:356-363.
181. Milligan, G., P. Svoboda, and C. M. Brown (1994). Why are there so many adrenoceptor subtypes? *Biochem. Pharmacol.* **48**:1059-1071.
182. Takeda, S., S. Kadowaki, T. Haga, H. Takaesu, and S. Mitaku (2002). Identification of G protein-coupled receptor genes from the human genome sequence. *FEBS Lett.* **520**:97-101.
183. Bai, T. R. (1992). Beta 2 adrenergic receptors in asthma: a current perspective. *Lung* **170**:125-141.
184. Barnes, P. J. (1993). Beta-adrenoceptors on smooth muscle, nerves and inflammatory cells. *Life Sci.* **52**:2101-2109.
185. Smiley, R. M., and M. Finster (1996). Do receptors get pregnant too? Adrenergic receptor alterations in human pregnancy. *J. Matern. Fetal Med.* **5**:106-114.
186. Overington, J. P., B. Al-Lazikani, and A. L. Hopkins (2006). How many drug targets are there? *Nat. Rev. Drug Discov.* **5**:993-996.
187. Wishart, D. S., C. Knox, A. C. Guo, S. Shrivastava, M. Hassanali, P. Stothard, Z. Chang, and J. Woolsey (2006). DrugBank: a comprehensive resource for in silico drug discovery and exploration. *Nucleic Acids Res.* **34**:D668-672.
188. Rosenbaum, D. M., V. Cherezov, M. A. Hanson, S. G. Rasmussen, F. S. Thian, T. S. Kobilka, H. J. Choi, X. J. Yao, W. I. Weis, R. C. Stevens, and B. K. Kobilka (2007). GPCR engineering yields high-resolution structural insights into beta2-adrenergic receptor function. *Science* **318**:1266-1273.
189. Rasmussen, S. G., H. J. Choi, J. J. Fung, E. Pardon, P. Casarosa, P. S. Chae, B. T. Devree, D. M. Rosenbaum, F. S. Thian, T. S. Kobilka, A. Schnapp, I. Konetzki, R. K. Sunahara, S. H. Gellman, A. Pautsch, J. Steyaert, W. I. Weis, and B. K.

- Kobilka (2011). Structure of a nanobody-stabilized active state of the beta(2) adrenoceptor. *Nature* **469**:175-180.
190. Rasmussen, S. G., B. T. DeVree, Y. Zou, A. C. Kruse, K. Y. Chung, T. S. Kobilka, F. S. Thian, P. S. Chae, E. Pardon, D. Calinski, J. M. Mathiesen, S. T. Shah, J. A. Lyons, M. Caffrey, S. H. Gellman, J. Steyaert, G. Skiniotis, W. I. Weis, R. K. Sunahara, and B. K. Kobilka (2011). Crystal structure of the beta2 adrenergic receptor-Gs protein complex. *Nature* **477**:549-555.
191. Rosenbaum, D. M., C. Zhang, J. A. Lyons, R. Holl, D. Aragao, D. H. Arlow, S. G. Rasmussen, H. J. Choi, B. T. Devree, R. K. Sunahara, P. S. Chae, S. H. Gellman, R. O. Dror, D. E. Shaw, W. I. Weis, M. Caffrey, P. Gmeiner, and B. K. Kobilka (2011). Structure and function of an irreversible agonist-beta(2) adrenoceptor complex. *Nature* **469**:236-240.
192. Hoffman, B. B., and R. J. Lefkowitz (1982). Adrenergic receptors in the heart. *Annu. Rev. Physiol.* **44**:475-484.
193. Chidiac, P., T. E. Hebert, M. Valiquette, M. Dennis, and M. Bouvier (1994). Inverse agonist activity of beta-adrenergic antagonists. *Mol. Pharmacol.* **45**:490-499.
194. Samama, P., G. Pei, T. Costa, S. Cotecchia, and R. J. Lefkowitz (1994). Negative antagonists promote an inactive conformation of the beta 2-adrenergic receptor. *Mol. Pharmacol.* **45**:390-394.
195. Xiao, R. P., H. Cheng, Y. Y. Zhou, M. Kuschel, and E. G. Lakatta (1999). Recent advances in cardiac beta(2)-adrenergic signal transduction. *Circul. Res.* **85**:1092-1100.
196. Azzi, M., P. G. Charest, S. Angers, G. Rousseau, T. Kohout, M. Bouvier, and G. Pineyro (2003). Beta-arrestin-mediated activation of MAPK by inverse agonists reveals distinct active conformations for G protein-coupled receptors. *Proc. Natl. Acad. Sci. USA* **100**:11406-11411.
197. Shenoy, S. K., M. T. Drake, C. D. Nelson, D. A. Houtz, K. Xiao, S. Madabushi, E. Reiter, R. T. Premont, O. Lichtarge, and R. J. Lefkowitz (2006). beta-arrestin-dependent, G protein-independent ERK1/2 activation by the beta2 adrenergic receptor. *J. Biol. Chem.* **281**:1261-1273.
198. Freedman, N. J., and R. J. Lefkowitz (1996). Desensitization of G protein-coupled receptors. *Recent Prog. Horm. Res.* **51**:319-351; discussion 352-313.
199. Hanyaloglu, A. C., and M. von Zastrow (2008). Regulation of GPCRs by endocytic membrane trafficking and its potential implications. *Annu. Rev. Pharmacol. Toxicol.* **48**:537-568.
200. Terrillon, S., and M. Bouvier (2004). Roles of G-protein-coupled receptor dimerization. *EMBO Rep.* **5**:30-34.
201. Insel, P. A., B. P. Head, R. S. Ostrom, H. H. Patel, J. S. Swaney, C. M. Tang, and D. M. Roth (2005). Caveolae and lipid rafts: G protein-coupled receptor signaling microdomains in cardiac myocytes. *Ann. N. Y. Acad. Sci.* **1047**:166-172.
202. Watts, A., I. D. Volotovski, and D. Marsh (1979). Rhodopsin-lipid associations in bovine rod outer segment membranes. Identification of immobilized lipid by spin-labels. *Biochemistry* **18**:5006-5013.

203. Fretten, P., S. J. Morris, A. Watts, and D. Marsh (1980). Lipid-lipid and lipid-protein interactions in chromaffin granule membranes. A spin label ESR study. *Biochim. Biophys. Acta* **598**:247-259.
204. Marsh, D., A. Watts, R. D. Pates, R. Uhl, P. F. Knowles, and M. Esmann (1982). ESR spin-label studies of lipid-protein interactions in membranes. *Biophys. J.* **37**:265-274.
205. Phillips, R., T. Ursell, P. Wiggins, and P. Sens (2009). Emerging roles for lipids in shaping membrane-protein function. *Nature* **459**:379-385.
206. Simons, K., and M. J. Gerl (2010). Revitalizing membrane rafts: new tools and insights. *Nat. Rev. Mol. Cell Biol.* **11**:688-699.
207. Lingwood, D., and K. Simons (2010). Lipid rafts as a membrane-organizing principle. *Science* **327**:46-50.
208. Oates, J., and A. Watts (2011). Uncovering the intimate relationship between lipids, cholesterol and GPCR activation. *Curr. Opin. Struct. Biol.* **21**:82102-807.
209. Gimpl, G., K. Burger, and F. Fahrenholz (1997). Cholesterol as modulator of receptor function. *Biochemistry* **36**:10959-10974.
210. Pang, L., M. Graziano, and S. Wang (1999). Membrane cholesterol modulates galanin-GalR2 interaction. *Biochemistry* **38**:12003-12011.
211. Burger, K., G. Gimpl, and F. Fahrenholz (2000). Regulation of receptor function by cholesterol. *Cell. Mol. Life Sci.* **57**:1577-1592.
212. Pucadyil, T. J., and A. Chattopadhyay (2004). Cholesterol modulates ligand binding and G-protein coupling to serotonin(1A) receptors from bovine hippocampus. *Biochim. Biophys. Acta* **1663**:188-200.
213. Pucadyil, T. J., and A. Chattopadhyay (2006). Role of cholesterol in the function and organization of G-protein coupled receptors. *Prog. Lipid. Res.* **45**:295-333.
214. Rajendran, L., H. J. Knolker, and K. Simons (2010). Subcellular targeting strategies for drug design and delivery. *Nat. Rev. Drug Discov.* **9**:29-42.
215. Xiang, Y., V. O. Rybin, S. F. Steinberg, and B. Kobilka (2002). Caveolar localization dictates physiologic signaling of beta 2-adrenoceptors in neonatal cardiac myocytes. *J. Biol. Chem.* **277**:34280-34286.
216. Yao, Z., and B. Kobilka (2005). Using synthetic lipids to stabilize purified beta2 adrenoceptor in detergent micelles. *Anal. Biochem.* **343**:344-346.
217. Hanson, M. A., V. Cherezov, M. T. Griffith, C. B. Roth, V. P. Jaakola, E. Y. Chien, J. Velasquez, P. Kuhn, and R. C. Stevens (2008). A specific cholesterol binding site is established by the 2.8 Å structure of the human beta2-adrenergic receptor. *Structure* **16**:897-905.
218. Kenakin, T. (2003). Ligand-selective receptor conformations revisited: the promise and the problem. *Trends Pharmacol. Sci.* **24**:346-354.
219. Ghanouni, P., J. J. Steenhuis, D. L. Farrens, and B. K. Kobilka (2001). Agonist-induced conformational changes in the G-protein-coupling domain of the beta 2 adrenergic receptor. *Proc. Natl. Acad. Sci. USA* **98**:5997-6002.

- 
220. Swaminath, G., Y. Xiang, T. W. Lee, J. Steenhuis, C. Parnot, and B. K. Kobilka (2004). Sequential binding of agonists to the beta2 adrenoceptor. Kinetic evidence for intermediate conformational states. *J. Biol. Chem.* **279**:686-691.
221. Swaminath, G., X. Deupi, T. W. Lee, W. Zhu, F. S. Thian, T. S. Kobilka, and B. Kobilka (2005). Probing the beta2 adrenoceptor binding site with catechol reveals differences in binding and activation by agonists and partial agonists. *J. Biol. Chem.* **280**:22165-22171.
222. Galandrin, S., G. Oligny-Longpre, and M. Bouvier (2007). The evasive nature of drug efficacy: implications for drug discovery. *Trends Pharmacol. Sci.* **28**:423-430.
223. Wisler, J. W., S. M. DeWire, E. J. Whalen, J. D. Violin, M. T. Drake, S. Ahn, S. K. Shenoy, and R. J. Lefkowitz (2007). A unique mechanism of beta-blocker action: carvedilol stimulates beta-arrestin signaling. *Proc. Natl. Acad. Sci. USA* **104**:16657-16662.
224. Kobilka, B. K., and X. Deupi (2007). Conformational complexity of G-protein-coupled receptors. *Trends Pharmacol. Sci.* **28**:397-406.
225. Fung, J. J., X. Deupi, L. Pardo, X. J. Yao, G. A. Velez-Ruiz, B. T. Devree, R. K. Sunahara, and B. K. Kobilka (2009). Ligand-regulated oligomerization of beta(2)-adrenoceptors in a model lipid bilayer. *EMBO J.* **28**:3315-3328.
226. Butt, H. J., and M. Jaschke (1995). Calculation of Thermal Noise in Atomic-Force Microscopy. *Nanotechnology* **6**:1-7.
227. Florin, E. L., M. Rief, H. Lehmann, M. Ludwig, C. Dornmair, V. T. Moy, and H. E. Gaub (1995). Sensing Specific Molecular-Interactions with the Atomic-Force Microscope. *Biosens. Bioelectron.* **10**:895-901.
228. Muller, D. J. (2008). AFM: a nanotool in membrane biology. *Biochemistry* **47**:7986-7998.
229. Sapra, K. T., P. S. H. Park, S. Filipek, A. Engel, D. J. Muller, and K. Palczewski (2006). Detecting molecular interactions that stabilize native bovine rhodopsin. *J. Mol. Biol.* **358**:255-269.
230. Dietz, H., F. Berkemeier, M. Bertz, and M. Rief (2006). Anisotropic deformation response of single protein molecules. *Proc. Natl. Acad. Sci. USA* **103**:12724-12728.
231. Janovjak, H., K. T. Sapra, A. Kedrov, and D. J. Muller (2008). From valleys to ridges: exploring the dynamic energy landscape of single membrane proteins. *Chemphyschem* **9**:954-966.
232. Janovjak, H., J. Struckmeier, M. Hubain, A. Kedrov, M. Kessler, and D. J. Muller (2004). Probing the energy landscape of the membrane protein bacteriorhodopsin. *Structure* **12**:871-879.
233. Sapra, K. T., J. Doehner, V. Renugopalakrishnan, E. Padros, and D. J. Muller (2008). Role of extracellular glutamic acids in the stability and energy landscape of bacteriorhodopsin. *Biophys. J.* **95**:3407-3418.
234. Kawamura, S., A. T. Colozo, D. J. Muller, and P. S. Park (2010). Conservation of molecular interactions stabilizing bovine and mouse rhodopsin. *Biochemistry* **49**:10412-10420.

235. Wells, J. W. (1992). Analysis and interpretation of binding at equilibrium, in *Receptor-Ligand Interactions: A Practical Approach*. In Oxford University Press. E. C. Hulme, editor, Oxford. 7.
236. Motulsky, H. a. C., A. (2004). Fitting models to biological data using linear and nonlinear regression: a practical guide to curve fitting. In Oxford University Press, New York.
237. Kumar, S., B. Ma, C. J. Tsai, N. Sinha, and R. Nussinov (2000). Folding and binding cascades: dynamic landscapes and population shifts. *Protein Sci.* **9**:10-19.
238. Oliveberg, M., and P. G. Wolynes (2005). The experimental survey of protein-folding energy landscapes. *Q. Rev. Biophys.* **38**:245-288.
239. Evans, E., and D. Needham (1986). Giant vesicle bilayers composed of mixtures of lipids, cholesterol and polypeptides. Thermomechanical and (mutual) adherence properties. *Faraday discussions of the Chemical Society*:267-280.
240. Needham, D., and R. S. Nunn (1990). Elastic deformation and failure of lipid bilayer membranes containing cholesterol. *Biophys. J.* **58**:997-1009.
241. Hebert, T. E., S. Moffett, J. P. Morello, T. P. Loisel, D. G. Bichet, C. Barret, and M. Bouvier (1996). A peptide derived from a beta2-adrenergic receptor transmembrane domain inhibits both receptor dimerization and activation. *J. Biol. Chem.* **271**:16384-16392.
242. Milligan, G. (2004). G protein-coupled receptor dimerization: function and ligand pharmacology. *Mol. Pharmacol.* **66**:1-7.
243. Liang, Y., D. Fotiadis, S. Filipek, D. A. Saperstein, K. Palczewski, and A. Engel (2003). Organization of the G protein-coupled receptors rhodopsin and opsin in native membranes. *J. Biol. Chem.* **278**:21655-21662.
244. Guo, W., E. Urizar, M. Kralikova, J. C. Mobarec, L. Shi, M. Filizola, and J. A. Javitch (2008). Dopamine D2 receptors form higher order oligomers at physiological expression levels. *EMBO J.* **27**:2293-2304.
245. Zocher, M., J. J. Fung, B. K. Kobilka, and D. J. Muller (2012). Ligand-Specific Interactions Modulate Kinetic, Energetic, and Mechanical Properties of the Human beta(2) Adrenergic Receptor. *Structure*. DOI 10.1016/j.str.2012.05.010
246. Kirilovsky, J., and M. Schramm (1983). Delipidation of a beta-adrenergic receptor preparation and reconstitution by specific lipids. *J. Biol. Chem.* **258**:6841-6849.
247. Kobilka, B. K., T. S. Kobilka, K. Daniel, J. W. Regan, M. G. Caron, and R. J. Lefkowitz (1988). Chimeric alpha 2-,beta 2-adrenergic receptors: delineation of domains involved in effector coupling and ligand binding specificity. *Science* **240**:1310-1316.
248. Gether, U., and B. K. Kobilka (1998). G protein-coupled receptors. II. Mechanism of agonist activation. *J. Biol. Chem.* **273**:17979-17982.
249. Ben-Arie, N., C. Gileadi, and M. Schramm (1988). Interaction of the beta-adrenergic receptor with Gs following delipidation. Specific lipid requirements for Gs activation and GTPase function. *Eur. J. Biochem.* **176**:649-654.

- 
250. Reiter, E., and R. J. Lefkowitz (2006). GRKs and beta-arrestins: roles in receptor silencing, trafficking and signaling. *Trends Endocrinol. Metab.* **17**:159-165.
251. Xiang, Y., and B. Kobilka (2003). The PDZ-binding motif of the beta2-adrenoceptor is essential for physiologic signaling and trafficking in cardiac myocytes. *Proc. Natl. Acad. Sci. USA* **100**:10776-10781.
252. Parnot, C., S. Miserey-Lenkei, S. Bardin, P. Corvol, and E. Clauser (2002). Lessons from constitutively active mutants of G protein-coupled receptors. *Trends Endocrinol. Metab.* **13**:336-343.
253. Sapra, K. T., P. S. Park, K. Palczewski, and D. J. Muller (2008). Mechanical properties of bovine rhodopsin and bacteriorhodopsin: possible roles in folding and function. *Langmuir* **24**:1330-1337.
254. Deupi, X., and B. K. Kobilka (2010). Energy Landscapes as a Tool to Integrate GPCR Structure, Dynamics, and Function. *Physiology* **25**:293-303.
255. Sakmar, T. P., R. R. Franke, and H. G. Khorana (1989). Glutamic acid-113 serves as the retinylidene Schiff base counterion in bovine rhodopsin. *Proc. Natl. Acad. Sci. USA* **86**:8309-8313.
256. Zhukovsky, E. A., and D. D. Oprian (1989). Effect of carboxylic acid side chains on the absorption maximum of visual pigments. *Science* **246**:928-930.
257. Bokoch, M. P., Y. Zou, S. G. Rasmussen, C. W. Liu, R. Nygaard, D. M. Rosenbaum, J. J. Fung, H. J. Choi, F. S. Thian, T. S. Kobilka, J. D. Puglisi, W. I. Weis, L. Pardo, R. S. Prosser, L. Mueller, and B. K. Kobilka (2010). Ligand-specific regulation of the extracellular surface of a G-protein-coupled receptor. *Nature* **463**:108-112.
258. Kenakin, T. P. (2008). Pharmacological onomastics: What's in a name? *Br. J. Pharmacol.* **153**:432-438.
259. Gether, U., F. Asmar, A. K. Meinild, and S. G. Rasmussen (2002). Structural basis for activation of G-protein-coupled receptors. *Pharmacol. Toxicol.* **91**:304-312.
260. Strader, C. D., I. S. Sigal, R. B. Register, M. R. Candelore, E. Rands, and R. A. Dixon (1987). Identification of residues required for ligand binding to the beta-adrenergic receptor. *Proc. Natl. Acad. Sci. USA* **84**:4384-4388.
261. Liapakis, G., J. A. Ballesteros, S. Papachristou, W. C. Chan, X. Chen, and J. A. Javitch (2000). The forgotten serine. A critical role for Ser-2035.42 in ligand binding to and activation of the beta 2-adrenergic receptor. *J. Biol. Chem.* **275**:37779-37788.
262. Ballesteros, J. A., A. D. Jensen, G. Liapakis, S. G. Rasmussen, L. Shi, U. Gether, and J. A. Javitch (2001). Activation of the beta 2-adrenergic receptor involves disruption of an ionic lock between the cytoplasmic ends of transmembrane segments 3 and 6. *J. Biol. Chem.* **276**:29171-29177.
263. Greasley, P. J., F. Fanelli, O. Rossier, L. Abuin, and S. Cotecchia (2002). Mutagenesis and modelling of the alpha(1b)-adrenergic receptor highlight the role of the helix 3/helix 6 interface in receptor activation. *Mol. Pharmacol.* **61**:1025-1032.

264. Savarese, T. M., and C. M. Fraser (1992). In vitro mutagenesis and the search for structure-function relationships among G protein-coupled receptors. *Biochem. J.* **283** ( Pt 1):1-19.
265. Wess, J. (1997). G-protein-coupled receptors: molecular mechanisms involved in receptor activation and selectivity of G-protein recognition. *FASEB J.* **11**:346-354.
266. Whorton, M. R., M. P. Bokoch, S. G. Rasmussen, B. Huang, R. N. Zare, B. Kobilka, and R. K. Sunahara (2007). A monomeric G protein-coupled receptor isolated in a high-density lipoprotein particle efficiently activates its G protein. *Proc. Natl. Acad. Sci. USA* **104**:7682-7687.
267. Kobilka, B. K. (2011). Structural insights into adrenergic receptor function and pharmacology. *Trends Pharmacol. Sci.* **32**:213-218.
268. Yao, X. J., G. Velez Ruiz, M. R. Whorton, S. G. Rasmussen, B. T. DeVree, X. Deupi, R. K. Sunahara, and B. Kobilka (2009). The effect of ligand efficacy on the formation and stability of a GPCR-G protein complex. *Proc. Natl. Acad. Sci. USA* **106**:9501-9506.
269. Sligar, S. G. (2003). Finding a single-molecule solution for membrane proteins. *Biochem. Biophys. Res. Commun.* **312**:115-119.
270. Bayburt, T. H., Y. V. Grinkova, and S. G. Sligar (2002). Self-assembly of discoidal phospholipid bilayer nanoparticles with membrane scaffold proteins. *Nano Lett.* **2**:853-856.
271. Denisov, I. G., Y. V. Grinkova, A. A. Lazarides, and S. G. Sligar (2004). Directed self-assembly of monodisperse phospholipid bilayer Nanodiscs with controlled size. *J. Am. Chem. Soc.* **126**:3477-3487.
272. Bayburt, T. H., and S. G. Sligar (2010). Membrane protein assembly into Nanodiscs. *FEBS Lett.* **584**:1721-1727.
273. Boldog, T., S. Grimme, M. Li, S. G. Sligar, and G. L. Hazelbauer (2006). Nanodiscs separate chemoreceptor oligomeric states and reveal their signaling properties. *Proc. Natl. Acad. Sci. USA* **103**:11509-11514.
274. Bayburt, T. H., and S. G. Sligar (2002). Single-molecule height measurements on microsomal cytochrome P450 in nanometer-scale phospholipid bilayer disks. *Proc. Natl. Acad. Sci. USA* **99**:6725-6730.
275. Alami, M., K. Dalal, B. Lelj-Garolla, S. G. Sligar, and F. Duong (2007). Nanodiscs unravel the interaction between the SecYEG channel and its cytosolic partner SecA. *EMBO J.* **26**:1995-2004.
276. Bayburt, T. H., and S. G. Sligar (2003). Self-assembly of single integral membrane proteins into soluble nanoscale phospholipid bilayers. *Protein Sci.* **12**:2476-2481.
277. Leitz, A. J., T. H. Bayburt, A. N. Barnakov, B. A. Springer, and S. G. Sligar (2006). Functional reconstitution of Beta2-adrenergic receptors utilizing self-assembling Nanodisc technology. *BioTechniques* **40**:601-602, 604, 606, passim.
278. Bayburt, T. H., S. A. Vishnivetskiy, M. A. McLean, T. Morizumi, C. C. Huang, J. J. Tesmer, O. P. Ernst, S. G. Sligar, and V. V. Gurevich (2011). Monomeric rhodopsin is sufficient for normal rhodopsin kinase (GRK1) phosphorylation and arrestin-1 binding. *J. Biol. Chem.* **286**:1420-1428.

- 
279. Kijac, A. Z., Y. Li, S. G. Sligar, and C. M. Rienstra (2007). Magic-angle spinning solid-state NMR spectroscopy of nanodisc-embedded human CYP3A4. *Biochemistry* **46**:13696-13703.
280. Raschle, T., S. Hiller, T. Y. Yu, A. J. Rice, T. Walz, and G. Wagner (2009). Structural and functional characterization of the integral membrane protein VDAC-1 in lipid bilayer nanodiscs. *J. Am. Chem. Soc.* **131**:17777-17779.
281. Kijac, A., A. Y. Shih, A. J. Nieuwkoop, K. Schulten, S. G. Sligar, and C. M. Rienstra (2010). Lipid-protein correlations in nanoscale phospholipid bilayers determined by solid-state nuclear magnetic resonance. *Biochemistry* **49**:9190-9198.
282. Borch, J., P. Roepstorff, and J. Moller-Jensen (2011). Nanodisc-based co-immunoprecipitation for mass spectrometric identification of membrane-interacting proteins. *Mol. Cell. Proteomics* **10**:O110 006775.
283. Engel, A., and H. E. Gaub (2008). Structure and mechanics of membrane proteins. *Annu. Rev. Biochem.* **77**:127-148.
284. Bosshart, P. D., F. Casagrande, P. L. Frederix, M. Ratera, C. A. Bippes, D. J. Muller, M. Palacin, A. Engel, and D. Fotiadis (2008). High-throughput single-molecule force spectroscopy for membrane proteins. *Nanotechnology* **19**:384014.
285. Struckmeier, J., R. Wahl, M. Leuschner, J. Nunes, H. Janovjak, U. Geisler, G. Hofmann, T. Jahnke, and D. J. Muller (2008). Fully automated single-molecule force spectroscopy for screening applications. *Nanotechnology* **19**:384020.
286. Haupts, U., J. Tittor, and D. Oesterhelt (1999). Closing in on bacteriorhodopsin: progress in understanding the molecule. *Annu. Rev. Biophys. Biomol. Struct.* **28**:367-399.
287. Dencher, N. A., H. J. Sass, and G. Buldt (2000). Water and bacteriorhodopsin: structure, dynamics, and function. *Biochim. Biophys. Acta* **1460**:192-203.
288. Cartailier, J. P., and H. Luecke (2003). X-ray crystallographic analysis of lipid-protein interactions in the bacteriorhodopsin purple membrane. *Annu. Rev. Biophys. Biomol. Struct.* **32**:285-310.
289. Hirai, T., S. Subramaniam, and J. K. Lanyi (2009). Structural snapshots of conformational changes in a seven-helix membrane protein: lessons from bacteriorhodopsin. *Curr. Opin. Struct. Biol.* **19**:433-439.
290. Huang, K. S., H. Bayley, M. J. Liao, E. London, and H. G. Khorana (1981). Refolding of an integral membrane protein. Denaturation, renaturation, and reconstitution of intact bacteriorhodopsin and two proteolytic fragments. *J. Biol. Chem.* **256**:3802-3809.
291. Popot, J. L., S. E. Gerchman, and D. M. Engelman (1987). Refolding of bacteriorhodopsin in lipid bilayers. A thermodynamically controlled two-stage process. *J. Mol. Biol.* **198**:655-676.
292. Oesterhelt, D., and W. Stoeckenius (1974). Isolation of the cell membrane of *Halobacterium halobium* and its fractionation into red and purple membrane. *Methods Enzymol.* **31**:667-678.
293. Mukai, Y., N. Kamo, and S. Mitaku (1999). Light-induced denaturation of bacteriorhodopsin solubilized by octyl-beta-glucoside. *Protein Engin.* **12**:755-759.

294. Heyn, M. P., R. J. Cherry, and N. A. Dencher (1981). Lipid-protein interactions in bacteriorhodopsin-dimyristoylphosphatidylcholine vesicles. *Biochemistry* **20**:840-849.
295. Isenbarger, T. A., and M. P. Krebs (2001). Thermodynamic stability of the bacteriorhodopsin lattice as measured by lipid dilution. *Biochemistry* **40**:11923-11931.
296. Kessler, M., and H. E. Gaub (2006). Unfolding barriers in bacteriorhodopsin probed from the cytoplasmic and the extracellular side by AFM. *Structure* **14**:521-527.
297. Rehorek, M., and M. P. Heyn (1979). Binding of all-trans-retinal to the purple membrane. Evidence for cooperativity and determination of the extinction coefficient. *Biochemistry* **18**:4977-4983.
298. Bayburt, T. H., Y. V. Grinkova, and S. G. Sligar (2006). Assembly of single bacteriorhodopsin trimers in bilayer nanodiscs. *Arch. Biochem. Biophys.* **450**:215-222.
299. Medalsy, I., U. Hensen, and D. J. Muller (2011). Imaging and Quantifying Chemical and Physical Properties of Native Proteins at Molecular Resolution by Force-Volume AFM. *Angew. Chem. Int. Ed.* **50**:12103-12108.
300. Dufrene, Y. F., E. Evans, A. Engel, J. Helenius, H. E. Gaub, and D. J. Muller (2011). Five challenges to bringing single-molecule force spectroscopy into living cells. *Nat. Methods* **8**:123-127.
301. Brouillette, C. G., R. B. McMichens, L. J. Stern, and H. G. Khorana (1989). Structure and thermal stability of monomeric bacteriorhodopsin in mixed phospholipid/detergent micelles. *Proteins* **5**:38-46.
302. Heyes, C. D., and M. A. El-Sayed (2002). The role of the native lipids and lattice structure in bacteriorhodopsin protein conformation and stability as studied by temperature-dependent Fourier transform-infrared spectroscopy. *J. Biol. Chem.* **277**:29437-29443.
303. Hunte, C. (2005). Specific protein-lipid interactions in membrane proteins. *Biochem. Soc. Trans.* **33**:938-942.
304. Rief, M., J. Pascual, M. Saraste, and H. E. Gaub (1999). Single molecule force spectroscopy of spectrin repeats: low unfolding forces in helix bundles. *J. Mol. Biol.* **286**:553-561.
305. Stahl, S. W., E. M. Puchner, and H. E. Gaub (2009). Photothermal cantilever actuation for fast single-molecule force spectroscopy. *Rev. Sci. Instrum.* **80**:073702.
306. Kobayashi, K., H. Yamada, and K. Matsushige (2011). Reduction of frequency noise and frequency shift by phase shifting elements in frequency modulation atomic force microscopy. *Rev. Sci. Instrum.* **82**:033702.
307. Sahin, O., S. Magonov, C. Su, C. F. Quate, and O. Solgaard (2007). An atomic force microscope tip designed to measure time-varying nanomechanical forces. *Nat. Nanotechnol.* **2**:507-514.
308. Lang, H. P., M. Hegner, and C. Gerber (2005). Cantilever array sensors. *Mater. Today* **8**:30-36.

- 
309. Favre, M., J. Polesel-Maris, T. Overstolz, P. Niedermann, S. Dasen, G. Gruener, R. Ischer, P. Vettiger, M. Liley, H. Heinzelmann, and A. Meister (2011). Parallel AFM imaging and force spectroscopy using two-dimensional probe arrays for applications in cell biology. *J. Mol. Recognit.* **24**:446-452.
310. King, G. M., A. R. Carter, A. B. Churnside, L. S. Eberle, and T. T. Perkins (2009). Ultrastable atomic force microscopy: atomic-scale stability and registration in ambient conditions. *Nano Lett.* **9**:1451-1456.
311. Florin, E. L., V. T. Moy, and H. E. Gaub (1994). Adhesion Forces between Individual Ligand-Receptor Pairs. *Science* **264**:415-417.
312. Benoit, M., D. Gabriel, G. Gerisch, and H. E. Gaub (2000). Discrete interactions in cell adhesion measured by single-molecule force spectroscopy. *Nat. Cell Biol.* **2**:313-317.
313. Lee, G. U., L. A. Chrisey, and R. J. Colton (1994). Direct Measurement of the Forces between Complementary Strands of DNA. *Science* **266**:771-773.
314. Rief, M., F. Oesterhelt, B. Heymann, and H. E. Gaub (1997). Single molecule force spectroscopy on polysaccharides by atomic force microscopy. *Science* **275**:1295-1297.
315. Kessler, M., K. E. Gottschalk, H. Janovjak, D. J. Muller, and H. E. Gaub (2006). Bacteriorhodopsin folds into the membrane against an external force. *J. Mol. Biol.* **357**:644-654.
316. Driessen, A. J. M., and N. Nouwen (2008). Protein translocation across the bacterial cytoplasmic membrane. *Annu. Rev. Biochem.* **77**:643-667.
317. Knowles, T. J., A. Scott-Tucker, M. Overduin, and I. R. Henderson (2009). Membrane protein architects: the role of the BAM complex in outer membrane protein assembly. *Nat. Rev. Microbiol.* **7**:206-214.
318. Zocher, M., C. Roos, S. Wegmann, P. D. Bosshart, V. Dotsch, F. Bernhard, and D. J. Muller (2012). Single-molecule force spectroscopy from nanodiscs: an assay to quantify folding, stability, and interactions of native membrane proteins. *ACS Nano* **6**:961-971.



# Curriculum Vitae

Basel, August 2012

---

## MICHAEL ZOCHER DIPL. BIOCHEM.

### PERSONAL DETAILS

---

Address: Schönaustr. 38  
CH-4058 Basel  
Switzerland

E-Mail [zocher.michael@googlemail.com](mailto:zocher.michael@googlemail.com)

Nationality: German  
Date of Birth: October 14, 1982  
Place of Birth: Ilmenau



### EDUCATION

---

2009 - 2012 Center for Cellular Imaging and Nanoanalytics, M.E.Mueller Institute for Structural Biology (MSB), Biozentrum, University of Basel, Switzerland  
Research for my PhD Thesis *Novel single-molecule force spectroscopy approaches to characterize interactions of membrane proteins*  
Research Group: Andreas Engel (in collaboration with Daniel Müller, ETH Zurich, Switzerland, and Brian Kobilka, Stanford University School of Medicine, USA)

2007 – 2008 Leibniz Institute for Age Research – Fritz Lipmann Institute, Jena, Germany  
Research for my Diploma Thesis *The Endoplasmic Reticulum Sorting Receptor Rer1 – Investigation of Function and Expression in Different Tissues*  
Research Group: Christoph Kaether

2005 – 2006 Erasmus year, Umeå University, Sweden

2002 – 2008 Friedrich Schiller University of Jena  
Biochemistry/Molecular Biology Diploma (elective: Molecular Biotechnology)  
Grade point average 1.2

1993 – 2001 Grammar school ‘Gymnasium Am Lindenberg’, Ilmenau  
Grad point average 1.0

1989 – 1993 Primary school, Ilmenau

### FURTHER QUALIFICATIONS

---

*Computer:*

Microsoft Office Excellent knowledge  
Adobe Photoshop Good knowledge  
Adobe Illustrator Excellent knowledge

### Language skills:

German	Native language
English	Good knowledge, fluently
Swedish	Good knowledge, one year stay in Sweden
French	Basic knowledge
Japanese	Basic knowledge

### EMPLOYMENTS

---

Since August 2012	Department of Biosystems Science and Engineering, ETH Zurich, Basel, Switzerland PostDoc
Nov. 2008 – Jan. 2009	Max Planck Institute of Molecular Cell Biology and Genetics (MPI-CBG), Biotechnology Center TU Dresden, Germany Scientific assistant Research Group: Daniel Müller
Sept. 2008 – Oct. 2008	Leibniz Institute for Age Research – Fritz Lipmann Institute, Jena, Germany Scientific assistant Research Group: Christoph Kaether
March 2006 – June 2006	Umeå University, Department of Radiation Sciences, Oncology Scientific assistant Research Group: Håkan Hedman
July 2001 – May 2002	Civilian service at the ‘Behindertenverband Ilmenau e.V.’

### SCHOLARSHIPS

---

PhD thesis	Marie Curie Fellows Association
online-Stipendium	e-fellows.net (since 2007)
Erasmus	Year abroad in Umeå, Sweden

### PUBLICATIONS

---

- M. Zocher**, C. Zhang, B.K. Kobilka and D.J. Müller. Cholesterol increases kinetic, energetic, and mechanical stability of the human  $\beta_2$  adrenergic receptor. *submitted*.
- C. Roos, **M. Zocher**, D.J. Müller, D. Münch, T. Schneider, H.G. Sahl, F. Scholz, J. Wachtveitl, Y. Ma, E. Henrich, V. Dötsch and F. Bernhard. Characterization of co-translationally formed nanodisc complexes with small multidrug transporters, proteorhodopsin and with the E. coli MraY translocase. *submitted*.
- M. Zocher**, J.J. Fung, B.K. Kobilka and D.J. Müller. Ligand-specific interactions modulate kinetic, energetic, and mechanical properties of the human  $\beta_2$  adrenergic receptor. *Structure* (2012). [Epub ahead of print]
- M. Zocher**, C. Roos, S. Wegmann, P.D. Bosshart, V. Dötsch, F. Bernhard and D.J. Müller. Single-molecule force spectroscopy from nanodiscs: an assay to quantify folding, stability, and interactions of native membrane proteins. *ACS Nano* (2012) **6**, 961-971.
- M. Fassler, **M. Zocher**, A. Guzman de la Fuente, J. Scheuermann, A. Capell, C. Haass, C. Valkova and C. Kaether. Masking of transmembrane-based retention signals controls ER-export of  $\gamma$ -secretase. *Traffic* (2010) **11**, 250-258.